



HAL
open science

Phase diagram of iron under extreme conditions measured with time resolved methods

Simone Anzellini

► **To cite this version:**

Simone Anzellini. Phase diagram of iron under extreme conditions measured with time resolved methods. General Physics [physics.gen-ph]. Université Pierre et Marie Curie - Paris VI, 2014. English. NNT : 2014PA066155 . tel-01164980

HAL Id: tel-01164980

<https://theses.hal.science/tel-01164980>

Submitted on 18 Jun 2015

HAL is a multi-disciplinary open access archive for the deposit and dissemination of scientific research documents, whether they are published or not. The documents may come from teaching and research institutions in France or abroad, or from public or private research centers.

L'archive ouverte pluridisciplinaire **HAL**, est destinée au dépôt et à la diffusion de documents scientifiques de niveau recherche, publiés ou non, émanant des établissements d'enseignement et de recherche français ou étrangers, des laboratoires publics ou privés.

Université Pierre et Marie Curie

ED 107

CEA-DAM Île de France - Laboratoire hautes pressions statiques

Phase diagram of iron under extreme conditions measured with time-resolved methods

Par Simone Anzellini

Thèse de doctorat de Physique

Dirigée par Paul Loubeyre et Carlo Meneghini

Présentée et soutenue publiquement le 20/05/2014

Devant un jury composé de :

M. Decremps Frederic	Maître de conférences	Président
M. Andrault Denis	Professeur	Rapporteur
M. Gorelli Federico	Ingénieur chercheur	Rapporteur
Mlle. Dewaele Agnès	Ingénieur chercheur	Encadrante
M. Loubeyre Paul	Ingénieur chercheur	Directeur de thèse
M. Meneghini Carlo	Ingénieur chercheur	Directeur de thèse





Contents

1	The phase diagram of iron	5
1.1	Introduction	5
1.2	Geophysical interest	6
1.3	State of the art	8
1.4	Conclusions	12
2	High Pressure - High Temperature experimental methods	15
2.1	Static high pressure device: the Diamond Anvil Cell (DAC) .	16
2.1.1	Membrane Diamond Anvil Cell	17
2.1.2	Laser Heated Diamond Anvil Cell (LH-DAC)	25
2.2	X-ray techniques	27
2.2.1	X-ray diffraction in a DAC	28
2.2.2	X-ray absorption fine structure in a DAC	30
3	High pressure - high temperature metrology	39
3.1	Introduction	39
3.2	Measuring P in a DAC	40
3.2.1	The ruby gauge	40
3.2.2	X-ray gauge	41
3.2.3	The case of Rhenium	44
3.3	Measuring T in a LH-DAC	52
4	XRD study of the Fe melting curve	59
4.1	Introduction	59
4.2	Sample loading	59
4.2.1	"Low" pressure	60
4.2.2	"High" pressure	62
4.3	Experimental setup	63
4.4	Experimental results	65
4.4.1	Textural evolution of the solid sample	65
4.4.2	Detection of melting	66
4.4.3	Chemical reactions	69
4.4.4	Volumetric thermal expansion	70

4.4.5	Comparison with previous LH-DAC results	72
4.5	Article	76
5	XAFS study of the Fe phase diagram	81
5.1	Introduction	81
5.2	Sample preparation	82
5.3	Experimental setup	82
5.4	Experimental results	84
5.5	Conclusion	88
6	Conclusion	91

Chapter 1

The phase diagram of iron

The main part of my PhD Thesis concerns the use of a time-resolved method to measure the melting of iron by the means of X-ray diffraction in Diamond Anvil Cells. This chapter is devoted to the description of the scientific motivations that have led to the choice of this PhD project. In the first section, a brief introduction on the iron chemical and physical properties is given. A description of the state of the art, together with the related issues concerning the various parts of the phase diagram of iron are presented in the second section of this chapter.

1.1 Introduction

Iron (Fe, Z=26) is one of the most common elements on the Earth and because of its abundance and peculiarities, for several years it has been inseparably linked to the development of the human society. There are four isotopes of iron ranging from ^{54}Fe , ^{56}Fe , ^{57}Fe and ^{58}Fe . Among all, ^{56}Fe is the most abundant isotope with an abundance of 91.754% on Earth and it is known as the most stable nucleus. Fe belongs to the metals of the first transition series and it can form a wide range of compounds mainly in the +2 and +3 oxidation states. Iron is a ferromagnetic material at ambient conditions. Fe electronic configuration is $1s^2 2s^2 2p^6 3s^2 3p^6 3d^6 4s^2$. Because of its reaction with water and oxygen, metal Fe can't be found in the Earth's crust but it can be obtained by the smelting process of different ore of which the principal one is the hematite. Once extracted, pure iron is a soft metal (softer than aluminium), with a silver white or grayish color. Some of its most important properties are ductility, malleability and high thermal conductivity. Malleability lets iron be beaten into sheets, without cleavage and ductility makes it possible for thin wires to be drawn from it. Thanks to its peculiarities and abundance on our planet, the interest in iron's properties and phase diagram covers different fields, in particular in geophysics, metallurgy and material science.

1.2 Geophysical interest

The advent of seismology during the XXth century allowed, for the first time in history, to probe the Earth's interior. In fact, the seismological observatories spread out all over the globe, allow to measure the travel time of the P- and S-wave and, therefore, their velocities. The P waves are compressional waves (the matter is compressed along the direction of propagation of the wave). The S waves, are shear waves (the matter oscillate perpendicularly to the direction of propagation of the wave). Global seismological models based on travel-time-distance curves for seismic waves and on periods of free oscillations have been developed.

Among all, the Preliminary Reference Earth Model (PREM) [1], set up in 1981 is one of the most widely used global seismological model. According to this model (Fig.1.1), the Earth is divided into radially symmetrical shells separated by seismological discontinuities, of which the principal are situated at depths of 400, 670, 2890 and 5150 km, corresponding to the seismic boundaries between upper mantle and transition zone, transition zone and lower mantle, mantle and core, liquid outer and solid inner core respectively.

The core (inner and outer) is considered to be mainly composed by Fe on the basis of the following evidences (e.g. [3, 4, 5]). First, the meteorites falling on Earth, which keep a record of the building blocks of the early solar system, are mainly composed by iron [6, 7]. Second, the internal geomagnetic field of the Earth must be produced by a dynamo mechanism, which is only possible in a liquid metallic region inside the Earth (e.g. [8, 9]). Third, the seismologically observed density and sound velocities of the core are close to those of iron measured at the appropriate pressures and temperatures [10, 11, 12, 13].

Nevertheless, it is estimated that an outer core of pure iron would have a density about 10% higher than the density deduced from seismological observations [10]. This deficit can be explained if iron is alloyed with some proportion of lighter elements [6]. Which are those light elements is still an object of debate but by analogy with meteorites it is reasonable to consider S, Si, O, C, K and H probable alloying elements (see [14, 3] for reviews).

The solid inner core forms from the solidification of the liquid outer core. This crystallization process releases a latent heat and a gravitational energy. This heat contributes to the convection movement in the liquid outer core and can explain the phenomenon of self-sustained geodynamo generating the Earth's magnetic field [8]. The knowledge of the temperature-depth profile (geotherm) inside the Earth can help to study these and other kindred phenomena such the cooling rate and the heat flux to the mantle Earth [15]. Geotherms are usually anchored in the depths of seismic discontinuities identified with phase transitions whose P, T boundaries are experimentally known or extrapolated [6]. The geotherm can then be deduced from

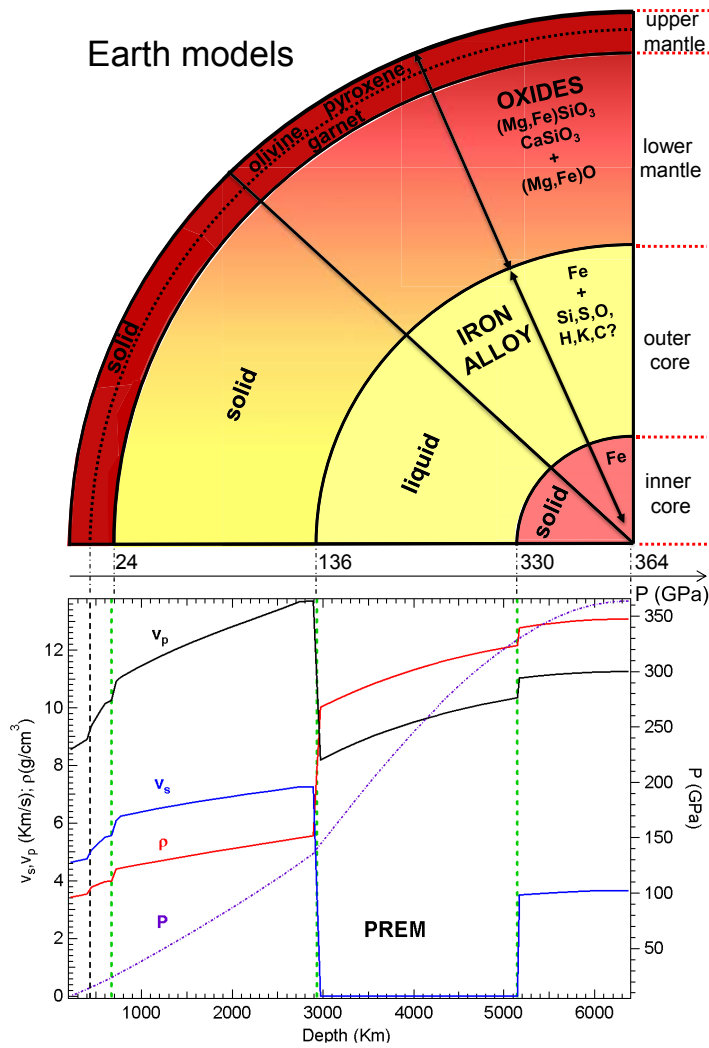


Figure 1.1: Bottom: Preliminary Reference Earth Model (PREM) [2] profiles within the Earth's interior: velocities v_s and v_p , the density ρ and the pressure P . The four seismological discontinuities (dashed lines) separate the Earth in different shells. Top: Corresponding compositional model of the Earth as a function of depth. The pressures at the interfaces between each couple of shells are also indicated.

consideration on the heat transport mechanisms (convective or conductive according to the specific phase [6]) and compositional model of the various shells of the Earth [6].

The geotherm in the core, can be calculated assuming an adiabatic distribution of the temperature due to the convective motion in the liquid core [6]

and using the Inner Core Boundary (ICB) as anchoring point [16]. The ICB is by definition the interface between the liquid and the solid core. Since the pressure of the ICB is accurately known (330 GPa), and since the main constituent of the core is Fe, a first approximation of the temperature of the ICB can be found by measuring the melting temperature of Fe at 330 GPa. Thus, the determination of the melting point of iron at ICB condition, provides important constraint on the geotherm in the core. In addition, the phase diagram of solid iron at very high pressures (330 GPa- 364 GPa) can shed light on the crystalline structure and physical properties of the inner core, including the so far unexplained elastic anisotropy of this region [17]. Therefore, a complete and rigorous characterization of the iron's phase diagram up to very high pressure and temperature poses important benchmarks on our knowledge on the characteristics of the interior of the Earth.

1.3 State of the art

In the last sixty years, many attempts have been made to find the phase diagram of iron up to the core conditions ($P= 135\text{-}364$ GPa, $T= 4000\text{-}7000$ K). However, consensus in the obtained results is limited to a narrow low P - T range ($P \leq 20$ GPa, $T \leq 2400$ K).

The moderate P - T phase diagram of Fe is reviewed in *Swartzendruber* [18] and it is reported in Fig. 1.2. At room temperature and atmospheric pressure, pure iron is stable in the body centered cubic - bcc - (α) phase. This phase is ferromagnetic, below the Curie temperature (1043 K) [19] before the transition to the paramagnetic face centered cubic - fcc - (γ) phase. At higher temperature (1667 K) and ambient pressure, Fe transforms into a second bcc phase (δ) before melting. The α , γ and δ phases are believed to be stabilized by magnetism [20, 21]. Under the application of an external pressure at ambient T , iron undergoes a transition at 13 GPa from the bcc α -phase to the hexagonal close packed - hcp - ϵ -phase structure [22] with the loss of its ferromagnetic long range order [23]. At $P= 10.5$ GPa and $T= 753$ K there is the α - γ - ϵ triple point. In the pure hcp ϵ -phase, superconductivity appears close to the transition between 15 and 30 GPa, below 2 K [24, 25].

Considering the phase diagram of iron at higher pressure and temperature, the so far obtained results show several discordant elements and still unsolved issues. In the following the various parts of the Fe phase diagram will be analyzed and the various studies performed so far will be discussed. Starting with the melting line of Fe, neither dynamics [26, 27, 13] and static [28, 29, 30, 31], nor thermodynamic modeling [32, 33, 34, 35] have resulted in a consensus on the ICB melting temperature, in part because these approaches suffer from intrinsic uncertainties.

Concerning static experiments in diamond anvil cell, the obtained results

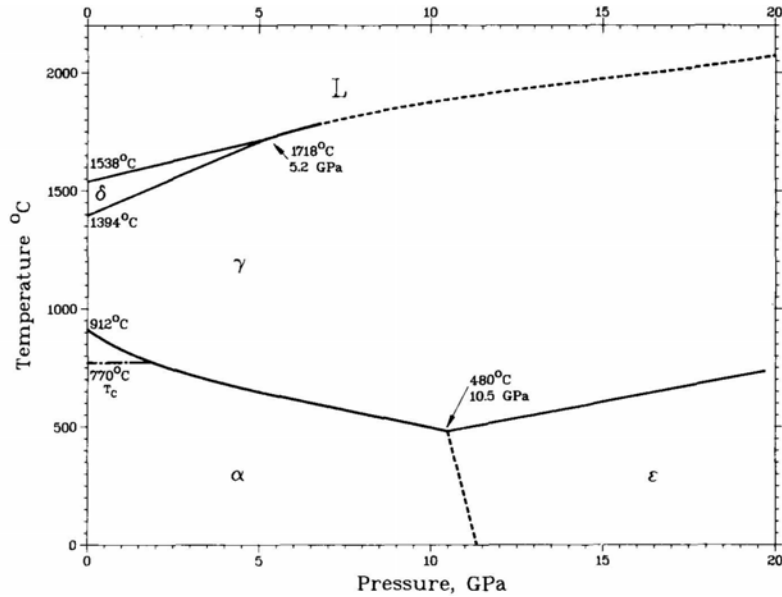


Figure 1.2: Low pressure - low temperature phase diagram of iron. The four solid-phases of Fe are plotted together with its liquid phase. The figure has been taken from [18] and the temperature are reported in Celsius

strongly depend on the adopted melting criterium, uncertainties in the pyrometric measurements and the possible temperature-induced chemical reactions. In 1993 *Boehler* [28] reported a melting temperature of 3800 K at $P=200$ GPa (5200 K at ICB) by texturing observation of melting in laser-heated diamond anvil cells. His data results lower than the ones obtained by a previous study [30] (4800 K at 136 GPa) based on the same melting criterium and on textural consideration on the recovered sample. Errors in pyrometry measurement due to temperature gradients in the laser-heated sample have been proposed as a possible cause of this discrepancy [36, 37, 28, 38].

In 2004, a study based on the observation of a diffuse X-ray diffraction signal from liquid as melting criterium [29] and performed up to 58 GPa, yielded intermediate melting temperatures. Other studies based on the same method [31, 39], observed the presence of solid iron above the melting curve of Ref.[28].

Dynamic measurements have long been considered the most promising way to determine the ICB temperature because of the possibility to reach pressure of the same order of the ICB during the experiments, yet the temperature determination and the possibility of super heating in shock compression [40] are major uncertainties. In 1986 *Brown and McQueen* [13] showed a

melting temperatures of 5500 K at $P=243$ GPa. During the experiment the shock temperature were calculated using a thermodynamic modeling. Using a similar technique, *Nguyen and Holmes* [27], reported a melting temperature of 5100 K at $P=225$ GPa, approximately on the same melting curve as *Brown and McQueen*. Another shock wave study which directly measured

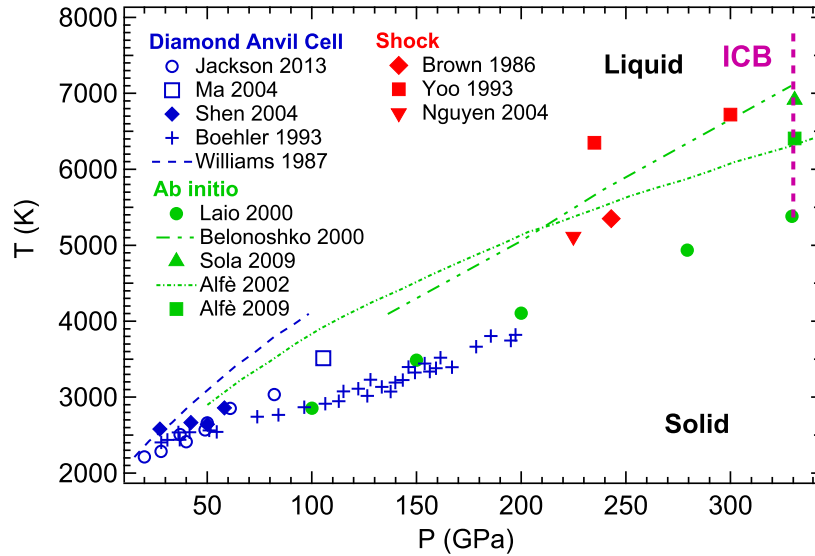


Figure 1.3: Melting curves obtained with static (blue symbols) [41, 31, 29, 28, 30], dynamic (red symbols) [13, 26, 27] high pressure technique and predicted with *ab initio* approaches (green symbols) [42, 32, 35, 34, 33].

the temperature by optical pyrometry [26], indicated melting temperatures (6350 K at 235 GPa and 6720 K at 300 GPa) higher than the previously reported in the other dynamic measurements [13, 27].

Finally, the tremendous advances in computational capacity have enabled quantum mechanics calculations of the melting behavior, but each method has underlying approximations or assumptions. For instance, melting temperatures from 6370 [34] to 7050 K [32] have been obtained with the same melting criterion - the coexistence of a liquid and solid phase in a molecular dynamics run - but a different description of interatomic forces within density functional theory. Going beyond density functional theory (DFT) with a quantum Monte Carlo simulation, melting was obtained at 6900 K [35] at 330 GPa. These calculations are consistent with the shock wave data [26, 13]. *Laio et al.* [42] combining first principle and classical molecular dynamics simulations, reported a melting curve that is consistent with static DAC data [28]. A summary of all the studies performed on the melting curve of iron is reported in Fig.1.3.

Another controversy concerns the high pressure - high temperature solid phase of iron. Available experimental data [43, 36, 28, 44, 45, 46] indicate that the γ - ϵ -melt triple point would be between 2500 - 3250 K and 50 - 94 GPa. In 1986 *Brown and McQueen* [13] investigating the phase diagram of Fe between 77 GPa and 400 GPa by the means of shock wave experiment, found two discontinuities in the sound velocities at 200 GPa and 243 GPa, interpreted respectively as the transition between the ϵ -Fe and γ -Fe and the onset of melting. This would give a γ - ϵ -melt triple point at least 100 GPa higher than the ones found in the other studies. *Boehler* [36] tried to explain the shock wave observations by the presence of another solid phase of Fe, whose structure remains unknown. As a consequence, the discontinuity observed at 200 GPa by *Brown and McQueen* [13] would correspond to a solid-solid phase transition from the ϵ -Fe to this new high-pressure solid phase.

Over the years, several structures were proposed for the fifth solid-phase of iron. In particular, a bcc (α') structure was suggested as the high-temperature high-pressure (above 200 GPa and 4000 K) phase [47] presents in the inner core of the Earth.

Since then, several theoretical studies have investigated the stability of the bcc phase against the hcp phase. In particular, simulation made by molecular dynamics (MD) methods predict the bcc structure to be the most stable for iron at ICB using either a Morse type potential [48] or an embedded atoms models [49]. Instead, different DFT simulations based on a full potential linear muffin-tin orbital method [50] or in a General Gradient Approximation (GGA) [51, 52], predict the hcp phase to be the most stable structure of iron at the ICB conditions.

In a recent shock wave study [27], only one discontinuity was observed in the sound velocities. This discontinuity observed at 225 GPa was associated to a solid-liquid phase transition, therefore no ϵ - α' phase transition was observed.

Discordant results are also obtained in recent static *in situ* X-ray diffraction measurement. In 2007 *Dubrovinsky et al.* [53] observed an high-pressure bcc phase in the $\text{Fe}_{0.9}\text{Ni}_{0.1}$ composition above $P= 225$ GPa and $T= 3400$ K. In 2010, instead, *Tateno et al.* [39] did not observe any solid-solid phase transition in pure iron in the pressure region between 120 and 370 GPa (see Fig.1.4).

Another "low pressure" phase has been proposed for iron: the β -phase. This phase would appear above 40 GPa and between 1500-3000 K [54, 28], its possible structure was a double-hcp (also called ϵ') [55, 56] or an orthorhombic structure [57]. However, the presence of these two new phases of iron have been discarded by the results obtained by recent static studies [27, 31, 46, 58, 39].

In Fig. 1.4 a summary of the predicted and well known phases of iron is

reported together with the recent data of [31, 46, 58, 39].

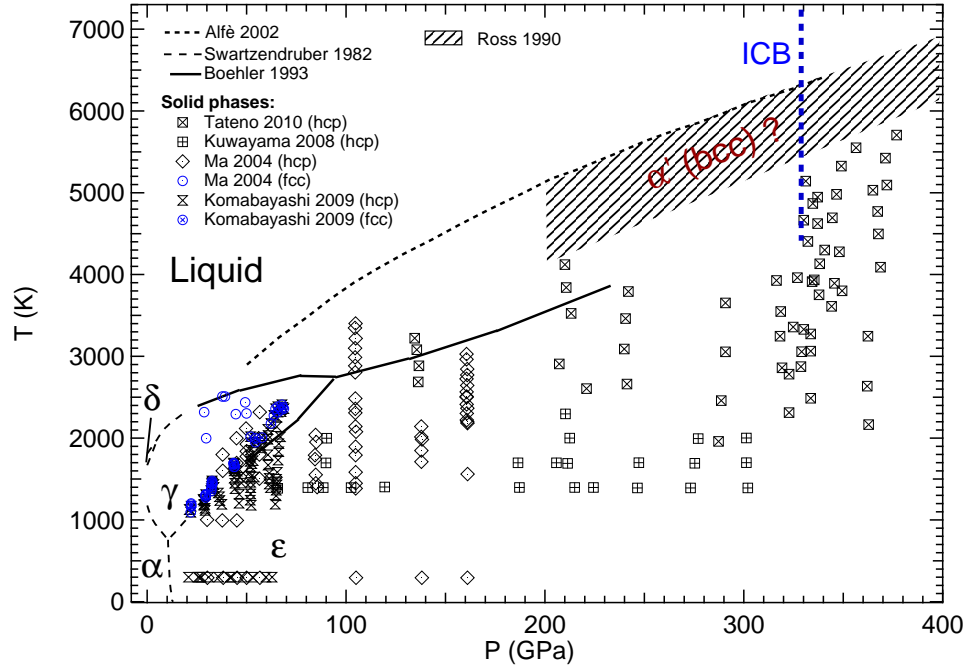


Figure 1.4: High pressure phase diagram of iron. The melting curve proposed by Alfè [33] and Boehler [28] are presented as possible "high" and "low" melting curves. The symbols indicate the P - T conditions at which ϵ -Fe or γ -Fe have been characterized by X-ray diffraction in diamond anvil cell [39, 58, 31, 46]. The dashed region indicates the unexplored P - T domain in which the α' phase has been predicted [47].

To sum up, the ϵ and the α' phases are both possible candidates for being the crystallographic structure of iron at the ICB conditions of the Earth. However, due to the technical issue linked to the extreme conditions to be reached (200-400 GPa and 4000 - 7000 K), further static investigation on the P - T domain proposed for the α' phase haven't been performed yet.

1.4 Conclusions

The knowledge of the phase diagram and melting curve of iron up to the ICB conditions are of fundamental importance in geophysics and planetary science. Nevertheless, even though this problem has been studied for decades through different experimental and theoretical approaches, a consensus on the obtained results is lacking. In particular, concerning the melting curve of Fe, a certain agreement have been observed between the results obtained by

dynamic experiment and *ab initio* calculation, while some results obtained by static measurement in diamond anvil cell give lower melting temperatures. A discrepancy in the melting temperature obtained by dynamic and static measurement was also observed in the melting curve of other metals [59, 60, 61], therefore it should be linked to a technical or a physical issue concerning the experiment performed in diamond anvil cell.

Due to the extreme conditions to be reached, several parameters (wrong experimental setup, chemical reactions, pressure and temperature gradients, erroneous melting criteria...) can influence the measure and the interpretation of the obtained data. An improvement of the techniques associated to the static experiment at extreme conditions of pressures and temperatures is then mandatory.

The main part of my work was performed using the *fast* X-ray diffraction (XRD) [60, 61] technique in laser-heated diamond anvil cells. This technique, based on the (*ad hoc*) experimental setup developed on the beamline ID27 [62] of the European Synchrotron Radiation Facility (ESRF), has already led to a resolution of the controversy on the melting curve of tantalum [61].

During my work, big efforts have been devoted to the preparation of good quality samples (chapter 4). In particular, we have worked out new methods to contain the samples in the insulating pressure transmitting medium. The obtained loading permit to prevent chemical reactions, heat the sample up even at very high pressure (up to 206 GPa) maximizing the probability to observe the apparition of the characteristic X-ray diffracted signal from a liquid (i.e. a diffuse ring).

The *fast* X-ray diffraction allows to follow the chemical, structural and textural evolution of the sample during a heating ramp. The obtained results can then be compared to the measured temperatures to check the coherence of the obtained results. In chapter 2 and chapter 3, an overview of the issues generally encountered in a laser-heated experiment in diamond anvil cell are reported together with the solutions and techniques adopted in this work.

The second part of my work concerns the study of the phase diagram of iron in a laser-heated diamond anvil cell by X-ray Absorption Fine Structure (XAFS) spectroscopy. The interest in this kind of study, lies in the short range order sensitivity of XAFS which makes it particularly suited to detect local order in crystalline, amorphous and liquids materials with the same precision.

Furthermore, XAFS is an element selective technique and, the shape of a XAFS spectrum is characteristic of the particular phase, chemical bonds and oxidation state of the probed sample. Small variation in the local structure, corresponds to intense variation in the shape of a XAFS spectrum.

In addition, the use of XAFS with an energy dispersive setup [63] permits to perform *fast* experiment with a millisecond temporal resolution [64]. Thus, the combination of XAFS and *fast* XRD analysis looks very promising for

a complete characterization of the solid and liquid part of the phase diagram of iron. In Chapter 5, the obtained preliminary results are discussed together with the experimental setup adopted.

Chapter 2

High Pressure - High Temperature experimental methods

This chapter surveys the apparatus and methods for high-pressure and high temperature studies used in this work. In the first part, the principle of the diamond anvil cell is described. The second part is focused on the X-ray technique used to probe the sample.

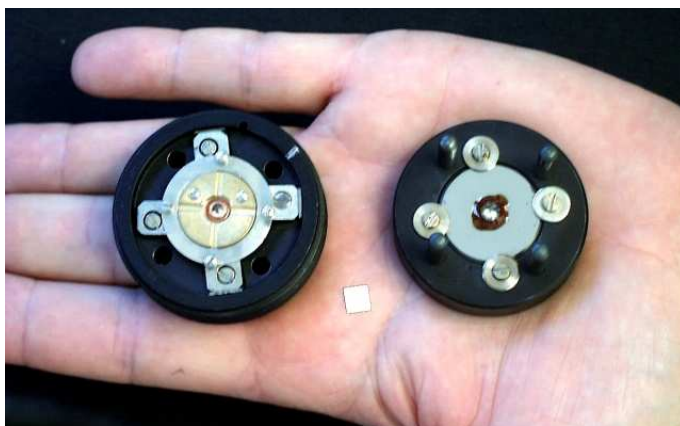


Figure 2.1: Picture of the main component of a DAC.

2.1 Static high pressure device: the Diamond Anvil Cell (DAC)

During this project, all the high pressure experiment have been performed in a static way by the means of the Diamond Anvil Cells (DAC). The DAC was invented in 1959 in the USA [65, 66] and it is currently the device that allows to generate the highest static pressure reachable.

In Fig.2.2, the principle of a DAC is illustrated. The center of the cell is composed by two gem-quality single crystal diamonds.

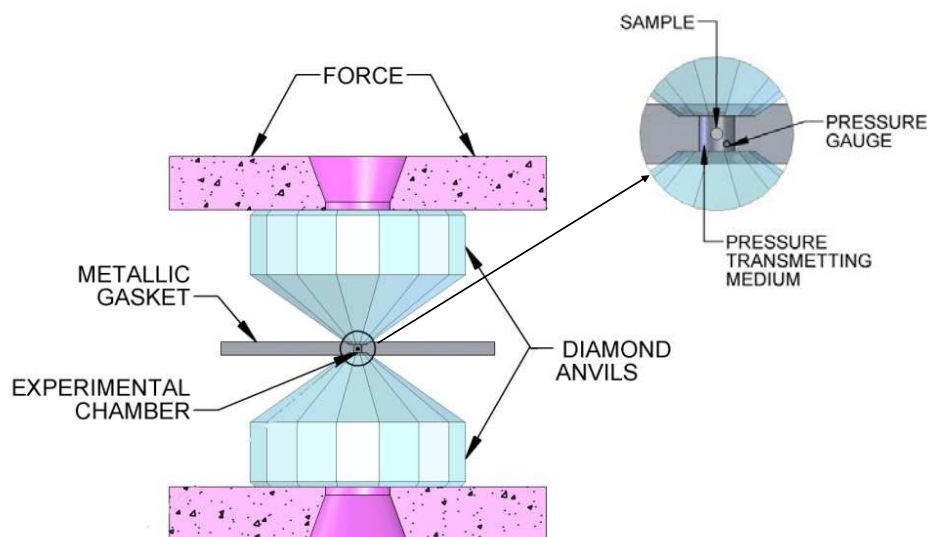


Figure 2.2: Principle of the diamond anvil cell.

The heads of the diamonds are cut to create flat faces. The diamonds are mounted so that a sample can be squeezed between the anvil's faces. The smaller the area A of the anvil faces, the higher the pressure P reached by the sample in the DAC for an equivalent value of applied force F ($P \simeq F/A$). One of the diamond anvils is usually mounted on the end of a sliding piston, while the other is stationary (cylinder). In the DAC used for this project, four dowels guide the piston so that the anvil faces meet very precisely. The piston is pushed by a mechanical device such as a screw or a small hydraulic ram, thus driving the two anvils together. A rocker or a tilting

2.1. STATIC HIGH PRESSURE DEVICE: THE DIAMOND ANVIL CELL (DAC)17

plate directly under the diamond anvils allows to orientate the two diamonds to be adjusted so that the faces are concentric and parallels.

The concept of Diamond Anvil Cell over the years have been applied in various ways so that every team has its own concept of cell. We have worked with membrane Diamond Anvil Cells.

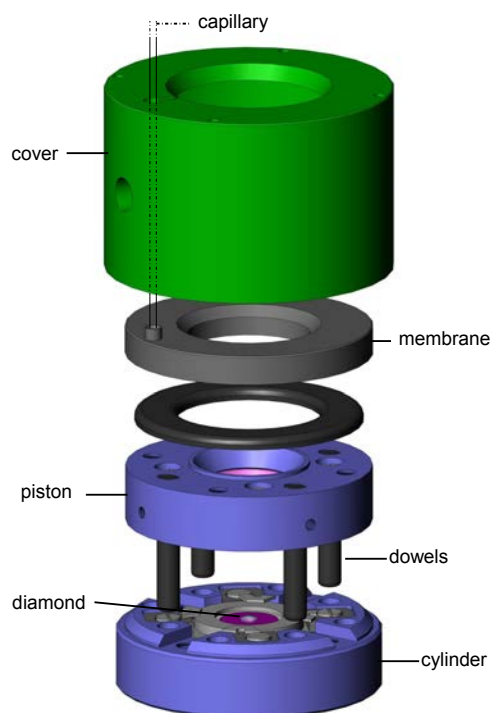


Figure 2.3: Schematic representation of the components of a membrane diamond anvil cell [67]. The membrane is filled with helium through a capillary and transmits the force to the piston.

2.1.1 Membrane Diamond Anvil Cell

In this kind of cell, the force is transmitted to the piston through a pressure exerted by a gas (Fig. 2.3). The idea of transmitting the force by hydraulic way was first suggested by *Besson and Pinceaux* [68] starting from a piston-cylinder system subsequently replaced by a sealed and deformable membrane filled with He [67].

The use of a membrane DAC presents various advantages:

- The applied force is proportional to the pressure in the membrane and a plot of the pressure measured in the cell vs the pres-

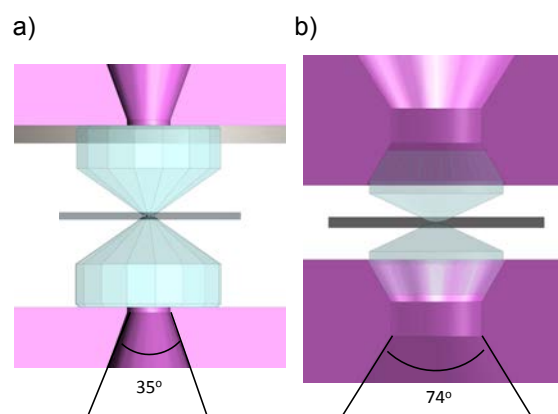


Figure 2.4: Scheme of two membrane DACs equipped with a standard anvil's support (a) and an *Almax – Boehler* design [69] (b).

sure in the membrane, allows to verify that the cell is working correctly.

-The pressure rise (drop) can be easily tuned by increase (decrease) the pressure of the membrane.

-There is the possibility of remotely control the pressure by the means of an automatic pressure driver. In this way, experiments that require the placement of the cell in poorly accessible locations (e.g. experiment in an experimental hutch of a Synchrotron) can be easily performed.

Depending on the experimental geometry required by the particular experiment, different anvils and corresponding supports's designs can be mounted in a membrane DAC. In particular, the *Almax-Boehler* (AB) [69] design have been used in experiments requiring a wider angular aperture and a thinner thickness of the diamond (Fig. 2.4). Let's focus now on the elements that play the principal roles in experiment performed in a DAC, namely: the diamonds, the gasket and the pressure transmitting media.

Diamonds

Diamonds are suitable anvils due to their hardness and transparency to electromagnetic radiation, which make the DAC well adapted for spectroscopic studies - such as Raman, infrared spectroscopy, X-ray absorption - and X-ray diffraction (XRD). The diamond anvils are cut from natural, gem-quality stones to have 16 faces. Great care must be taken in centering and aligning

2.1. STATIC HIGH PRESSURE DEVICE: THE DIAMOND ANVIL CELL (DAC)19

the two anvils to avoid premature failure of the diamonds at high pressure. The adjustment procedure is made under a microscope: the concentricity is achieved moving the support of the piston diamond slightly to superimpose the two polygons corresponding to the face of the anvils; the parallelism is checked by observing the interference fringes that appear when the two anvils are not parallel.

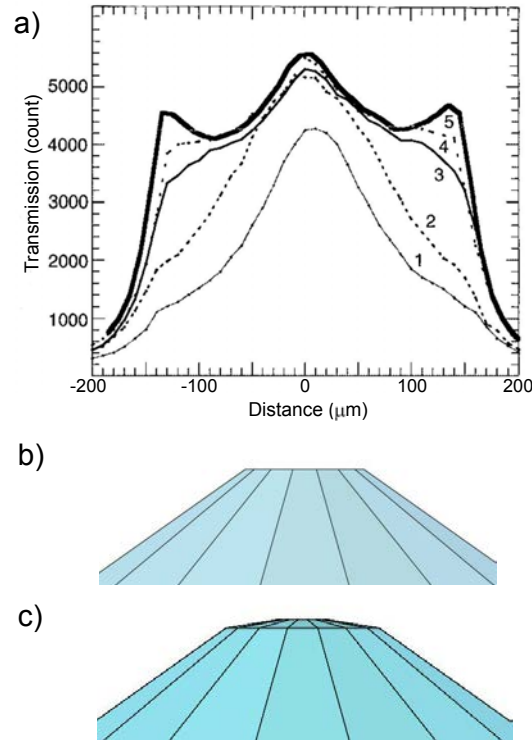


Figure 2.5: a) X-ray transmission profile of a beveled diamond (8°) with a central flat of $10 \mu\text{m}$ and a culet of $300 \mu\text{m}$. The image has been taken from Ref. [70] and shows the cupping phenomenon the diamond undergoes with the increasing pressure. The different curves, numbered from 1 to 5, represent the diamond's profile from ambient to 300 GPa pressure. b) Schematic representation of a diamond with flat tip. c) Schematic representation of a diamond with beveled tip.

The probe radiation passes through a conical hole drilled in the backing plate. Despite the relatively high transparency of diamonds to light and X-rays, the usual thickness of a pair of $1/4 - 1/3$ carat anvil, may create a significant impediment to the radiation transmission. In the case of X-rays, a 5 mm diamond thickness of a pair of 0.3 carat anvils will essentially block the transmission of photons for $E < 10 \text{ KeV}$ (see [71]).

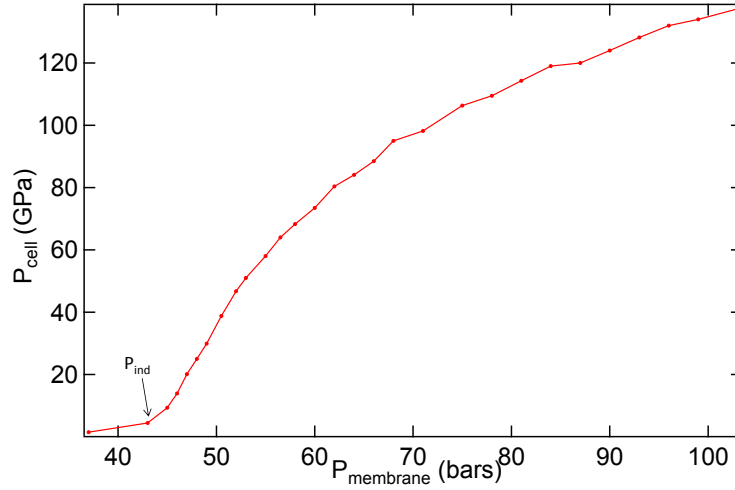


Figure 2.6: Plot of the pressure measured in the cell as a function of the pressure in the membrane. For membrane pressure below the value used to indent the gasket (P_{ind}), the pressure in the cell increases very slowly. Just above the indentation pressure, the slope of the plotted graph undergoes a sharp rise. When the deformation of the diamond start to occur, the slope of the curve becomes smoother up to a saturation point after which the failure of the diamond occurs.

During the pressure increase, the diamond undergoes a very strong elastic deformation (cupping) near the sample region (Fig. 2.5). Due to this deformation, the force transmitted to the sample through the diamond is attenuated. This phenomenon is well illustrated in Fig. 2.6 where the measured pressure in the cell is plotted as a function of the corresponding pressure in the membrane. When the deformation of the diamond occurs, the slope of the represented curve becomes smoother up to a saturation point after which the diamond breaks. For this reason, beveled anvils (Fig. 2.5) [72] (bevel angle of 8°) have been used in this project to reach pressure higher than ~ 80 GPa. In fact, due to their particular shape, the beveled diamonds present a longer deformation path with respect to the diamonds of the same culet's size but with a classical shape. A higher pressure domain can thus be reached with this kind of anvils.

Table 2.1 reports a list of the diamond used, in particular the relationship between the adopted culet size and the pressure achievable is shown.

Gasket

To be encapsulated in the high pressure chamber of a DAC, the sample is placed in a small hole drilled in a metallic gasket placed between the two diamonds. The gasket consists of a metallic foil of typically 200 - 250 μm of initial thickness. The capability of containing extremely high pressure originates from the anvil-gasket friction and the gasket small thickness [73]. To increase the hardness of the metal, avoid large deformation and instability of the hole, the foil is pre-indented to a thickness slightly greater than the final thickness, which depends on the maximum pressure that is planned to be applied. The sample is often embedded in a pressure transmitting medium

culet size (μm)	thickness (μm)	Φ (μm)	P_{max} (GPa)
400	45	300	35
300	35	120	80
200 \times 300	30	80	100
150 \times 300	23	70	120
100 \times 300	17	40	150
70 \times 300	14	30	200

Table 2.1: Values of the Re gasket parameters according to the culet size of the adopted diamonds. Φ : diameter of the laser-drilled hole; P_{max} : maximum pressure reachable with the corresponding values for the gasket and the diamonds.

which fills the pressure chamber of the DAC. The diameter of the gasket's hole depends on the chosen pressure medium. In case of a solid pressure medium (e.g. NaCl, KCl, KBr), the ideal size is a little bit smaller than half of the diamond culet size. In the case of a very compressible pressure medium (e.g. He, Ne, N₂, H₂), the hole's diameter should be 3/4 of the total culet's size because the size of the hole dramatically decreases with the pressure rise.

During this work, we have used gasket made of rhenium (Re) with an initial thickness of 250 μm . Re has been chosen because is the least compressible of all metals [74, 75, 76, 77] and as a high yield-strength material, it reaches higher pressure in the sample chamber. Concerning the indentation procedure, we have seen that for Re, a good thickness of the gasket is generally obtained for each culet's size of the diamonds by applying a pressure of 30 GPa (the corresponding values of thicknesses are reported in Table 2.1).

In this work, the gasket's holes have been drilled by a pulsed (8 ns) Q-switched doubled YAG laser (532 nm). A picture of the laser-drilling set-up adopted by our laboratory is reported in Fig. 2.7 together with a working

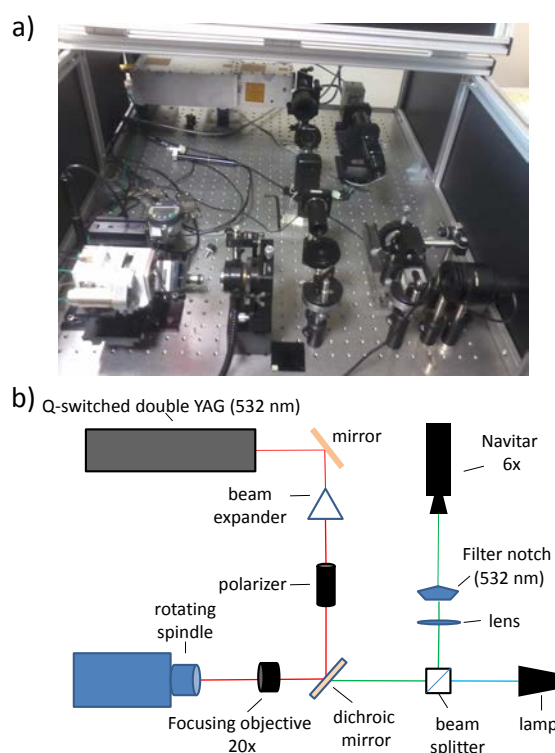


Figure 2.7: Picture (a) and working scheme (b) of the laser-drilling set-up adopted in our laboratory.

scheme. In this set-up, a microscope objective focus the laser beam on the gasket indentation. The pre-indented gasket is fixed to a high precision rotating spindle equipped with a supporting plate. The gasket indentation is first aligned on the spindle rotational axis by a manual xy stage attached to the gasket supporting fixture. A fine alignment is thus obtained using xy piezo actuators mounted on the axis of the spindle. The magnified image of the gasket is visualized through a Navitar 6x. To optimize the ablation process, the intensity and frequency of the laser are tuned to 19 A and 40 khz respectively and the rotation speed is tuned to optimize the roughness quality of the drilled hole. Such laser-drilling set-up has allowed us to quickly (2-3 min) obtain gasket holes ranging between 30 - 300 μm with a precision of $\sim 2 \mu\text{m}$. In Fig. 2.8 top and side view of a laser-drilled Re gasket images taken with a Scanning Electron Microscope (SEM) are reported. The values of the hole's diameter adopted in this work are reported in Table 2.1.

2.1. STATIC HIGH PRESSURE DEVICE: THE DIAMOND ANVIL CELL (DAC)23

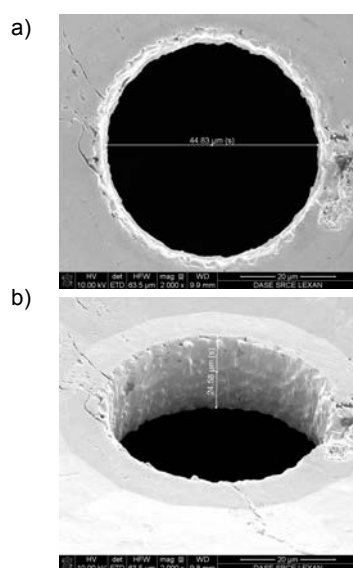


Figure 2.8: a) Top and b) side views of a laser-drilled hole ($44.83 \mu\text{m}$ diameter) of a Re gasket of $24.58 \mu\text{m}$ thickness. The two images have been taken with a Scanning Electron Microscope (SEM).

Hydrostaticity and pressure transmitting media

Pressure transmitting media can be liquids (alcohol, alcohol mixture (Methanol - Ethanol 4:1), silicone oil), soft solids (alkali halides), hard solids (MgO , Al_2O_3 , etc) and condensed gases (He, Ne, N_2 , Ar, etc). The adopted transmitting medium must not chemically react with the sample and must not interfere with the measurement of the sample.

A fluid pressure transmitting medium supports no shear and transmits an hydrostatic pressure to the sample. With the increasing pressure the transmitting medium solidifies. Beyond this point, shear stresses appear and the pressure across the experimental volume becomes inhomogeneous. The variation of stress conditions at different points in the sample depends on the strength of the medium. The hydrostatic limits of several pressure transmitting media were determined [78] by measuring the pressure homogeneity with several ruby chips over the area of the gasket aperture.

Gases, are the best pressure media for room and low temperature experiments. In particular He is considered to be the best pressure-transmitting medium (a comparison between the standard deviations between the pressure measured over the high pressure chamber of a DAC at 40 GPa is reported in Tab. 2.2 for Ar, Ne and He). He is the element with the highest freezing pressure (11.6 GPa at 300 K [68]) and even in its solid phase, it releases stress through recrystallization [79]. In 2001 *Takemura* [80] reported

Name	Freezing pressure (GPa)	Standard deviation (GPa)
Ar	1.4	1.2
Ne	4.8	0.3
He	11.6	0.15

Table 2.2: Freezing pressure at 300 K and standard deviations of the pressure measured in ref. [78] at 40 GPa for Ar, Ne and He.

that good hydrostatic conditions are maintained in solid helium to at least 50 GPa. While in 2007 *Dewaele and Loubeyre* [81] have shown that the effect of non-hydrostatic stress in the high pressure chamber of a DAC filled with He, is negligible for Ag, Mo and Cu up to 150 GPa.

During this project KCl has been used as pressure transmitting medium for laser heating experiment, while He has been adopted for the experiment at ambient temperature.

A particular gas-loading procedure has been developed in our laboratory and will be presented in the next paragraph.

Gas loading

A gas loading system was developed by our lab at the CEA-DIF in collaboration with the company Sanchez Technologies (Viarmes, France) and consists of a fully automated system whose principle of operation is illustrated in Fig. 2.9.

The DAC is placed in a sealed vessel that can contain a gas up to a maximum pressure of 1500 bar (circuit C_1). The membrane of the DAC is then connected to a different circuit (C_2) of pressure. C_1 and C_2 are connected.

1-The pressures in C_1 and C_2 are increased with a controlled speed by a piston compressor.

2-Once the loading pressure is reached (~ 1500 bar), the two circuits are separated by closing a valve. A pressure difference $\Delta P = P_{C_2} - P_{C_1}$ is then built. ΔP must be such as to ensure a force on the piston to seal the pressure chamber of the DAC.

3-The two pressures of the membrane and of the housing chamber are lowered maintaining a constant ΔP until $P_{C_1}=0$.

The pressure ramps are defined by the user. Once the gas loading procedure is ended, the membrane circuit is isolated and the DAC is ready to be used for the experiment.

2.1. STATIC HIGH PRESSURE DEVICE: THE DIAMOND ANVIL CELL (DAC)25

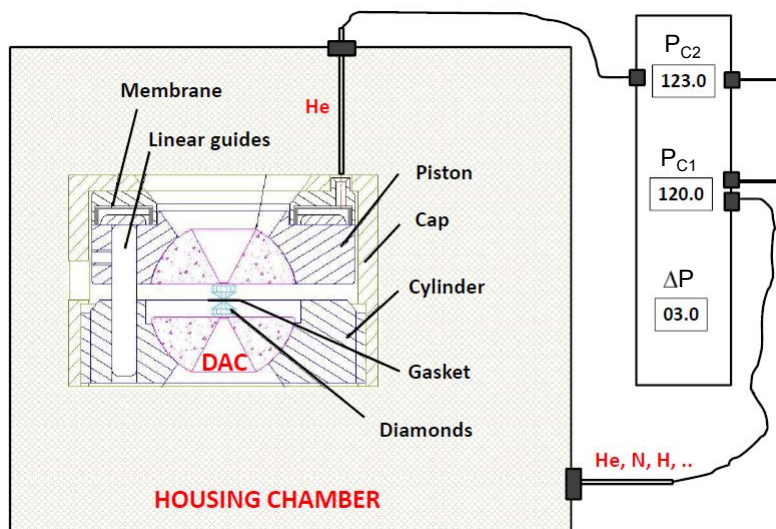


Figure 2.9: Schematic representation of the operation of the gas loading system developed in our laboratory.

2.1.2 Laser Heated Diamond Anvil Cell (LH-DAC)

A sample in the high pressure chamber of a DAC can be heated up using internal or external heating methods. Internal heating methods, involve the resistive heating of the sample. This can be achieved either by passing an electric current through a miniature heating assembly [82] or by directly passing the current through the sample if it is conducting [36]. However, the maximum temperature reported in such kind of device are of the order of 3500 K [53] and the decrease of the gasket's strength due to heating limits the reachable pressure.

The highest P - T domain achievable in a DAC can be obtained by laser heating the sample i.e. by focusing a high-power laser onto the sample surface. Temperature of the order of ~ 5700 K have been reported at ~ 360 GPa by *Tateno et al.* [39]. In Fig 2.10 the P - T domains reachable by resistive and laser heating are reported.

During a laser heating experiment in a DAC visual, spectroscopic and X-ray diffraction measurement can be performed *in situ*. The principal requirements for a laser to perform a laser-heating experiment in a diamond anvil cell are: focusing, high power, stability in power and beam position; suitable wavelength for absorption and a wavelength outside the spectral range in

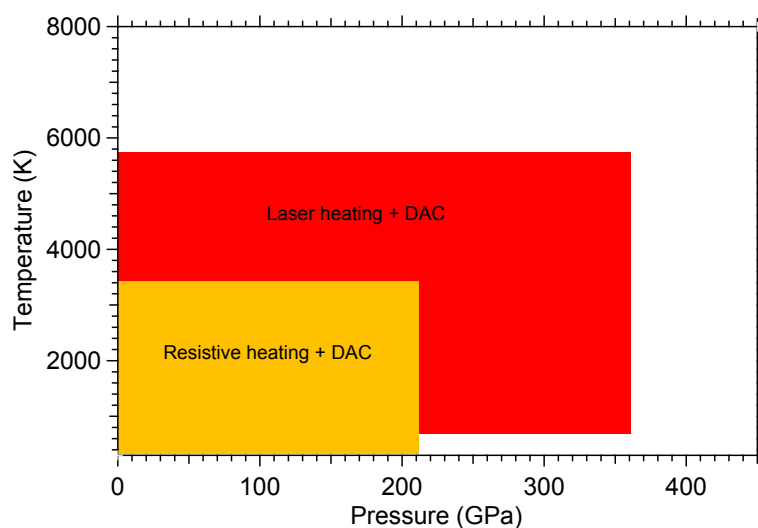


Figure 2.10: P - T domain reachable with resistive and laser heated diamond anvil cell [53, 39].

which the incandescent light from the sample is measured.

The extremely high thermal conductivity of diamond causes an important heat loss if the laser heated sample is placed directly in contact with it. In this case, it is impossible to heat the sample up. For this reason, the sample should be embedded in a medium with a low thermal conductivity that doesn't absorb the laser radiation but thermally insulate the sample from the diamond. The adopted pressure medium should not react chemically with the sample and can also be used to prevent chemical reactions between the diamond and the sample.

However, even when an insulating medium is used, thermal gradients exist in the sample. A 2D simulation done by *Geballe et al.* [83] of the temperature distribution in a laser heated DAC is reported in Fig.2.11. In this simulation a sample of $5 \mu\text{m}$ of thickness is laser heated from both sides assuming the sample absorption coefficient to be $10 \mu\text{m}^{-1}$ and a thermal conductivity of $84 \text{ W}/(\text{m}\cdot\text{K})$. The sample is thermally insulated by a material of $2.5 \mu\text{m}$ thickness and thermal conductivity of $18 \text{ W}/(\text{m}\cdot\text{K})$.

According to this simulation, in such an experiment the temperature decreases by 2000 K $5 \mu\text{m}$ away in radial direction from the laser hot spot. Axially this temperature difference is of the order of 1500 K in $2.5 \mu\text{m}$. In general, radial thermal gradient can be minimized by using lasers with a large FWHM. The thickness and thermal conductivities of the sample and insulating material also influence the axial thermal gradients produced in the

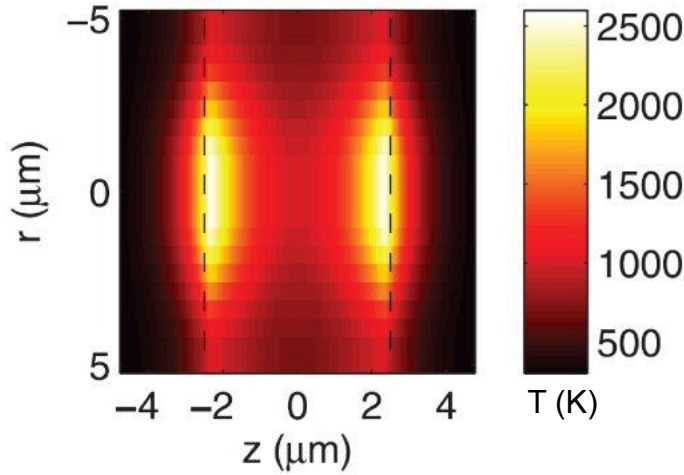


Figure 2.11: Distribution of temperature in a laser-heated diamond anvil cell according to the simulation of *Geballe et al.* [83].

pressure chamber of a LH-DAC. We can make an estimation of the thermal gradient for a typical sample loading adopted in this work. Using Ref. [83] with an iron sample (conductivity $\sim 30 \text{ W}/(\text{m}\cdot\text{K})$ at 2500 K [84]) of $\sim 4 \mu\text{m}$ thickness, is insulated by two KCl layers (conductivity $\sim 1.7 \text{ W}/(\text{m}\cdot\text{K})$ at 2500 K [85]) of the same thickness, we estimate that there is a temperature difference of $\sim 200 \text{ K}$ between the center and the surface of the sample.

2.2 X-ray techniques

X-rays are an important and widely used tool in the investigation of the electronic and crystalline structure of materials.

For *in situ* experiments at high pressure (and at high temperature), a very intense and highly focused beam is crucial because of the very small sample dimensions (a typical dimension of the sample adopted in this work for experiment above 150 GPa is of the order of $3 \mu\text{m}$). Moreover, high-pressure experiments require a high X-ray energy because of the limited X-ray aperture of the DAC and the high absorbing pressure window (sample and diamonds).

During this work the experiments have been performed at the beamlines ID24 [64] and ID27 [86] of the European Synchrotron Radiation Facility (ESRF) in Grenoble (France). These two beamlines have been designed for *in situ* experiment at extreme conditions. In fact, the high photon fluxes ($\sim 10^{14}$ photons/s) from the insertion devices in the energy range between 5-30 KeV, are highly focalized to a very small size ($2 \times 3 \mu\text{m}^2$ and $3 \times 3 \mu\text{m}^2$ for ID27 and ID24 respectively) by the alignment of X-ray mirrors in the Kirkpatrick-Baez geometry [87].

Two different X-ray technique have been adopted during this work: X-Ray Diffraction (XRD) has been extensively used to investigate the phase transition of Fe in different P - T domains and the Equation Of State (EOS) of Re at room temperature, while X-Ray Absorption Fine Structure (XAFS) spectroscopy has been used as a technique complementary to XRD in the study of the phase diagram of iron.

2.2.1 X-ray diffraction in a DAC

XRD allows determining the structure, the symmetry and the crystallographic parameters of a crystalline phase. In what follows a brief review of the well known principle is done.

X-rays are electromagnetic waves with a wavelength of the same order of magnitude as the interatomic distances in condensed matter. As a consequence, the interaction of X-ray with the electrons produces a diffraction phenomenon. In addition, when X-rays interact with a crystalline sample, interference phenomena can occur. The analysis of the resulting interference pattern lead to a characterization of the microscopical structural properties of the sample. In the framework of the far field approximation [88] the scattered amplitude from a solid with a volume V is written as:

$$A = \int_V dV \rho_e(r) \exp(2i\pi(\mathbf{k} - \mathbf{k}') \cdot \mathbf{r}) \quad (2.1)$$

In this expression $\rho_e(r)$ represents the local electron density; \mathbf{k} and \mathbf{k}' are the wave numbers of the incoming and scattered radiation. In a crystal, the atoms are arranged in a periodic way and a base can be defined in the forms $\{\mathbf{a}, \mathbf{b}, \mathbf{c}\}$, in the way that a translation vector (direct lattice) $\mathbf{T} = u\mathbf{a} + v\mathbf{b} + w\mathbf{c}$ (u, v, w integer) will leave unchanged the electronic density. This electronic density can be expressed as:

$$\rho_e(r) = \sum_{\mathbf{h}} \rho_{e,\mathbf{h}} e^{2i\pi\mathbf{h} \cdot \mathbf{r}} \quad (2.2)$$

where \mathbf{h} is defined as $\mathbf{h}=h\mathbf{a}^*+k\mathbf{b}^*+l\mathbf{c}^*$ (h,k,l are integer) and $\{\mathbf{a}^*,\mathbf{b}^*,\mathbf{c}^*\}$ is the base of the reciprocal lattice defined as:

$$\begin{cases} \mathbf{a}^* = \frac{1}{2\pi v} \mathbf{b} \times \mathbf{c} \\ \mathbf{b}^* = \frac{1}{2\pi v} \mathbf{c} \times \mathbf{a} \\ \mathbf{c}^* = \frac{1}{2\pi v} \mathbf{a} \times \mathbf{b} \end{cases}$$

where v is the volume of the parallelepiped formed by the vector \mathbf{a} , \mathbf{b} and \mathbf{c} ; $v=|\mathbf{a} \cdot (\mathbf{b} \times \mathbf{c})|$. The vector \mathbf{h} , is perpendicular to the planes (hkl) and its modulus is given by $|\mathbf{h}|=1/d_{hkl}$, where d_{hkl} is the distance between two planes of the lattice.

Combining the two equations 2.1 and 2.2 to have a nonzero amplitude, we can obtain in the hypothesis of elastic scattering (i.e. $|\mathbf{k}|=|\mathbf{k}'|$) the diffraction condition:

$$2\mathbf{k} \cdot \mathbf{h} = |\mathbf{h}|^2 \quad (2.3)$$

This is the vectorial expression of the *Bragg's law*, that can be equivalently expressed as:

$$2d_{hkl} \sin \theta = \lambda \quad (2.4)$$

In Fig. 2.12 a representation of the diffraction of an X-ray from a family of planes at a distance d_{hkl} with each other is shown. The angle θ is the half of the so-called *diffraction angle* which represents the total deviation of the X-ray beam due to the diffraction process. λ is the wavelength of the X-ray and $k=1/\lambda$.

The Bragg's law provides information on the inter-planar distances (d_{hkl}) and the relative positions of the planes, these information permit to extrapolate the structure of the primitive cell. However it doesn't permit to determine the position of the atoms in the cell. This information can be extrapolated from the relative intensities of the peaks: for a Bragg's reflection in fact, the amplitude of a diffracted wave is given by the expression:

$$F_{hkl} = \sum_i f_{at,i}(\mathbf{h}) e^{-2i\pi\mathbf{h}\cdot\mathbf{r}_i} \quad (2.5)$$

$$f_{at,i}(\mathbf{k}) = \int_{V_{at}} dV \rho_e(r) e^{-2i\pi\mathbf{k}\cdot\mathbf{r}_i} \quad (2.6)$$

The term $f_{at,i}$ is called *atomic form factor*. Considering I as the intensity of the diffracted beam, we can simply demonstrate that $I = |F|^2$ and considering that $f_{at,i} = Z$ for $k = 0$, the intensities of the diffracted beams will scale with Z^2 (Z =atomic number). The term F_{hkl} is called *structure factor* and it contains information on the atomic positions inside the cell.

During this work the X-ray diffraction experiments have been performed in angle dispersive mode. In this geometry, a monochromatic beam is diffracted by the sample and the scattered signal is collected on image plates (CCD or

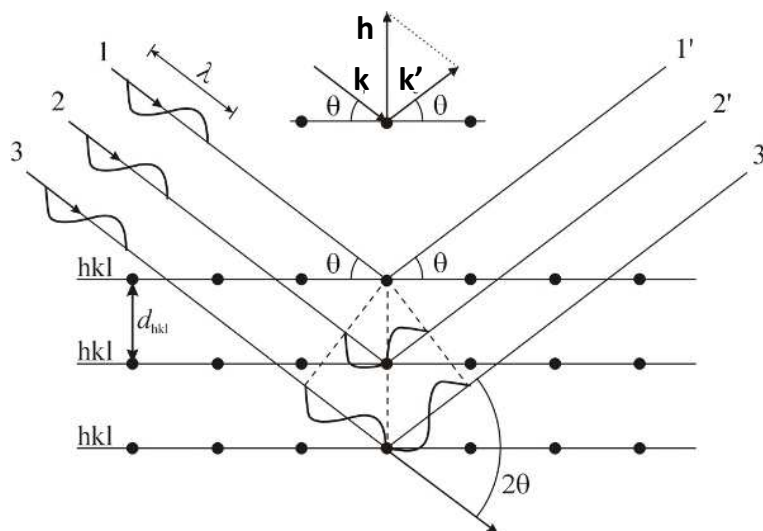


Figure 2.12: Representation of Bragg's reflection from a family of planes at a distance d_{hkl} from each other.

MAR345) (Fig. 2.13a). The collected signal is circularly integrated with the Fit2D software [89]. The integration parameters (sample-detector distance, beam center, etc..) are obtained from a LaB_6 reference sample. From the analysis of the obtained I versus 2θ plot a structural characterization of the sample can be done. In particular, the position of the XRD lines yields the space group and lattice parameters of the probed sample. While the analysis of the relative intensities yield information on the atomic position within the cell.

In Fig. 2.13, a schematic representation of an angle dispersive XRD experiment is reported together with an example of 2D XRD pattern and the corresponding integrated signal.

2.2.2 X-ray absorption fine structure in a DAC

X-ray Absorption Fine Structure spectroscopy (XAFS) is an experimental method allowing to study the local order of materials in every state (solid, liquid, vapor), crystalline or amorphous, from bulk to nano-scale systems. XAFS allows studying phase transitions (structural or magnetic) [90, 91, 92] of materials under extreme conditions of pressure and/or temperature [93, 94]. *Time resolved* XAFS techniques have been developed down to the ps scale [95]. All these features make XAFS a basic probe for material science, widely complementary to XRD.

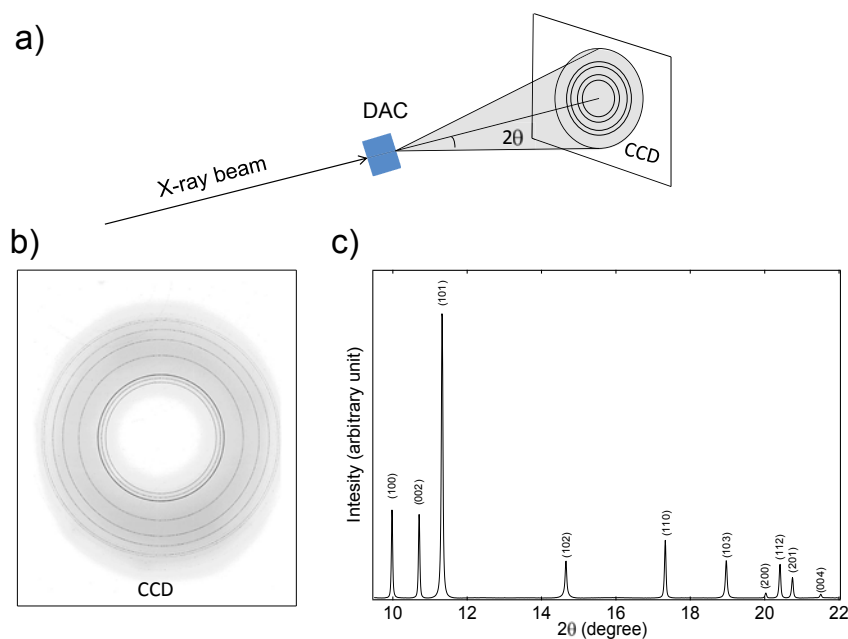


Figure 2.13: a) Schematic representation of an angle dispersive XRD experiment in a DAC. b) Example of the diffraction image of a Re powder sample and the corresponding circularly integrated signal (c).

In what follows, a phenomenological introduction to XAFS will be reported.

Consider a monochromatic X-ray beam passing through a material of thickness t , the transmitted intensity (I) is reduced with respect to the incident one (I_0) according to the *Beer – Lambert* law:

$$I = I_0 e^{-\mu t} \quad (2.7)$$

where μ , the linear absorption coefficient, depends on the photon energy and on the sample composition and density. In general, when the energy $h\nu$ of X-ray photons increases, the absorption coefficient $\mu(\nu)$ decreases. This smooth behavior is interrupted by sharp discontinuities, the absorption edges (Fig. 2.14a), which originate when the photons gain high enough energy to extract an electron from an energy level. The highest-energy absorption edges, the K edges, correspond to the extraction of an electron from the deepest level (1s level). The following table establishes the connection between high energy edges and core electronic levels.

Edge:	M _V	M _{IV}	M _{III}	M _{II}	M _I	L _{III}	L _{II}	L _I	K
Core level:	3d _{5/2}	3d _{3/2}	3p _{3/2}	3p _{1/2}	3s	2p _{3/2}	2p _{1/2}	2s	1s

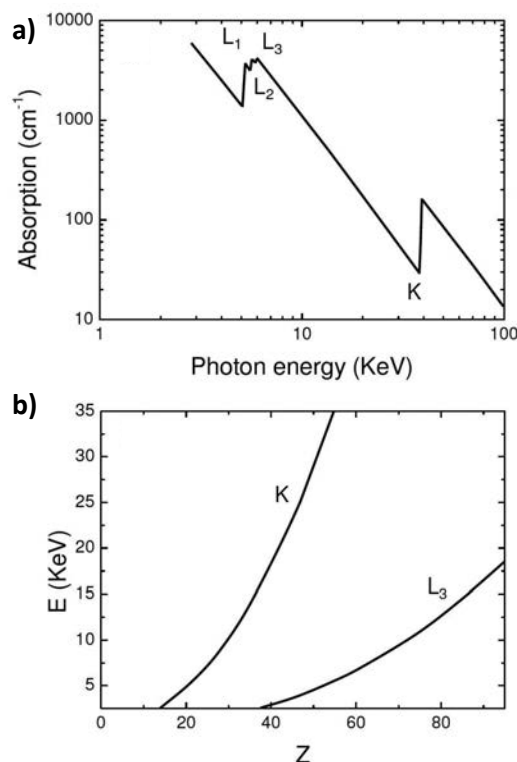


Figure 2.14: a) Absorption coefficient of Ce evidencing the discontinuities associated to the edges. b) Binding energy at the K- and L₃-edges as a function of the atomic number Z .

Since the binding energies of electrons increase with the atomic number (Fig. 2.14b), an edge energy corresponds to a well defined atomic species.

After the absorption of an X-ray photon, an isolated atom can be either excited, if the photon energy corresponds to the energy difference between an electronic core level and an unoccupied bound level, or ionized, if the photon energy is larger than the binding energy, so that the electron (photo-electron) is ejected from the atom.

In correspondence of an edge, the absorption coefficient exhibits the *X-ray Absorption Fine Structure* (XAFS) [96, 97]. For isolated atoms (noble gases, metallic vapors) the XAFS is limited to a few eV around the edge, and reflects the transitions of the core electron to unoccupied bound levels. In molecular gases and condensed systems the XAFS is strongly influenced by the presence of the atoms surrounding the absorber one. In fact, when an

X-ray photon of high enough energy is absorbed by an atom, a core electron, whose orbital is small with respect to the atomic size, is ejected from the atom.

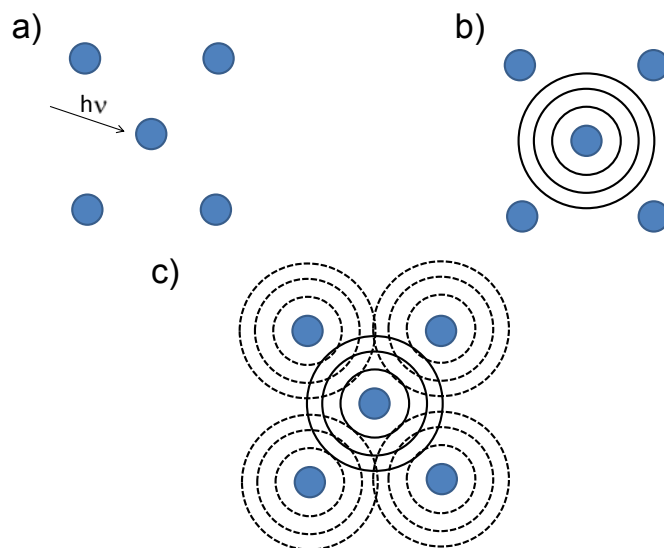


Figure 2.15: Schematic representation of the XAFS process. a) The atom absorbs a photon. b) The photoelectron is emitted as an outgoing spherical wave. c) The spherical wave is backscattered by the nearby atoms and interfere with the outgoing wave.

The outgoing photo-electron is described by a wavefunction whose wavelength λ decreases when the photon energy $h\nu$ increases. The absorption coefficient $\mu(\nu)$ of the isolated atom is proportional to a superposition integral of the localized core wavefunction and the outgoing wavefunction. If the absorber atom is not isolated, the photo-electron can be scattered by the neighbouring atoms, giving rise to an incoming wavefunction (Fig. 2.15). As a consequence, the total photo-electron wavefunction is now a superposition of the outgoing and the scattered waves. The phase relationship between the outgoing wave and the scattered waves, evaluated at the core site of the absorbing atom, depends on the photo-electron wavelength and on the distance R between the atoms involved. The variation of the phase relationship as a function of photon energy $h\nu$ influences the amplitude of the total wavefunction at the core site, giving rise to a modulation of the absorption coefficient. The frequency of the XAFS oscillations depends on the distance between absorber and back-scatterer atoms. Their amplitude is proportional to the number of back-scatterer atoms.

Two main peculiarities characterize XAFS:

- a) The selectivity of atomic species, which is obtained by tuning the X-ray energy at the corresponding absorption edge.
- b) The insensitivity to long-range order, due to the short mean free path of the photo-electron, typically limited to about 10 Å.

These peculiarities make XAFS a local structural probe permitting to get information on the coordination number and interatomic distances around an absorbing atom. In addition, XAFS sensitivity to local order, permit to indiscriminately characterize crystalline, amorphous and liquid material with the same precision.

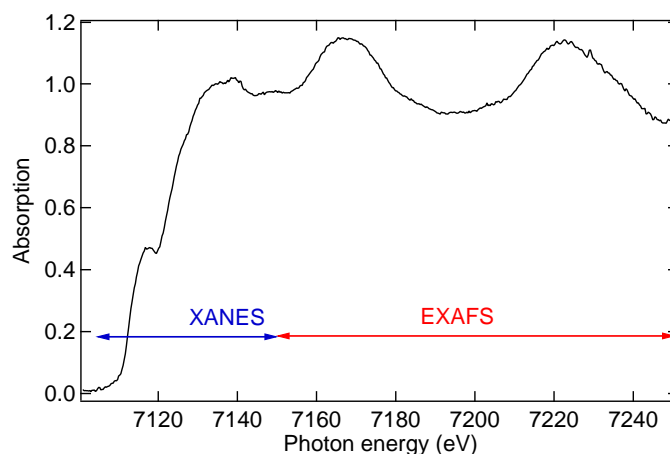


Figure 2.16: Absorption K-edge of hcp-Fe at 40 GPa and room temperature.

Different regions of XAFS are usually distinguished (Fig. 2.16):

- a) A *pre-edge* and *edge* region, limited to a few eV around the edge and dominated by the effects of transitions to localized electronic states and multipole transitions. It is very sensitive to the details of the atomic potential.
- b) The structure within 30÷50 eV above the edge is called *XANES* (X-ray Absorption Near Edge Structure) or *NEXAFS* (Near Edge X-ray Absorption Fine Structure) [97, 98]. Here, the fine structures are dominated by multiple scattering processes of the photoelectrons emitted with low kinetic energy. From XANES (including the pre-edge and edge regions), information can be obtained on the local electronic as well as geometric structure.

c) The fine structure extending from the XANES region up to typically one thousand eV, is called *EXAFS* (Extended X-ray Absorption Fine Structure) and is due principally to single scattering events. EXAFS contains information on the local geometric structure surrounding a given atomic species.

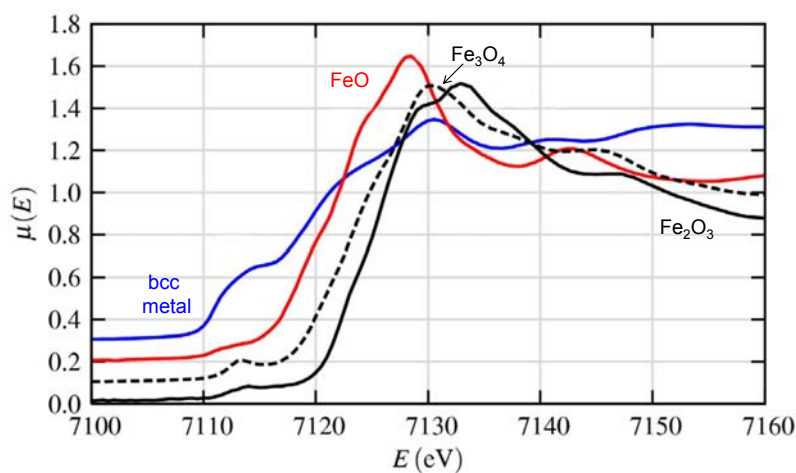


Figure 2.17: Edge-shift in the absorption spectra due to different oxidation states of Fe. The image as been taken from [99]

The quantitative interpretation of EXAFS is nowadays well established [97, 100, 101, 102, 103, 104]. On the other hand the quantitative interpretation of XANES is still complex [97, 105]. The shape, position and intensities of the XANES peaks are strongly affected by local symmetry and binding geometry (Fig. 2.17). Therefore, the XANES features are often qualitatively interpreted, which brings information on the local symmetry and geometry [106, 107], electronic structure, oxidation state and chemical coordinations [108, 109].

During this work, XAFS measurements have been performed on the energy dispersive beamline ID24 at the ESRF. The concept of this beamline is illustrated in Fig. 2.18. A polychromatic beam, is energy dispersed and focused by elliptical curved crystal [63, 110]. Because the X-rays strike the crystals at slightly different angles along its length, the bent crystal acts as a polychromator, diffracting a different energy at each point. The energy-dispersed beam converges to a focal point at the sample position. The beam transmitted through the sample, then diverges towards a Position Sensitive

Detector (PSD).

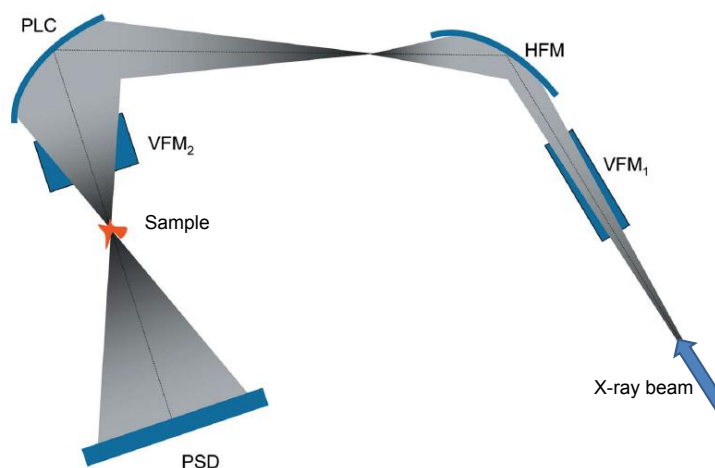


Figure 2.18: Complete optical scheme adopted on ID24, consisting of a pair of mirrors in the Kirkpatrick-Baez geometry (VFM₁ and HFM) and the polychromator crystal (PLC). A second vertically focusing mirror (VFM₂) downstream of the polychromator is used to refocus the beam onto the sample. The transmitted signal is then collected on a Position Sensitive Detector (PSD). This figure has been taken from Ref. [64].

The incident beam position on the detector, can be directly correlated to the energy.

According to the Beer-Lambert equation (2.7), the XAFS spectrum is obtained by taking the logarithm of the ratio between the I_0 and I signals, where I_0 and I are spatial X-ray intensity distribution in the absence and presence of the sample respectively. In such an experiment, the transmitted spectrum in the whole energy range is visualized at the same time on the PSD.

Compared to the scanning energy method, in which the XAFS spectra are obtained by rotating a monochromator and collecting the transmitted signal at each energy step, the energy dispersive method presents different advantages. The acquisition time is strongly reduced and can reach the millisecond temporal resolution [64]. Furthermore, higher stability of the energy scale and focal spot position is obtained, since there are no moving components during the acquisition [111].

Theoretical simulations of the XAFS spectra of selected elements or compounds in different P - T conditions, can be performed with the FEFF code

[112] and compared to the experimental results. FEFF uses an *ab initio* self-

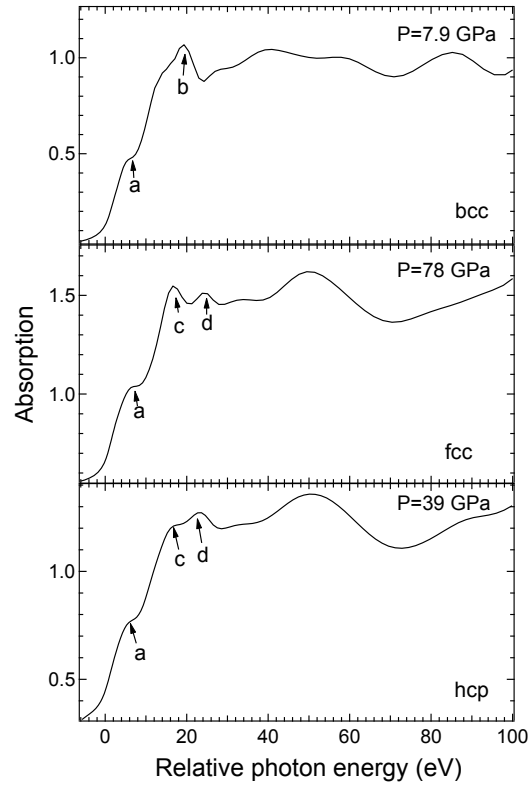


Figure 2.19: Simulated absorption spectra for bcc, fcc and hcp phases of Fe. The absorption ($A = \ln \frac{I_0}{I}$) is plotted versus the relative photon energy with respect to the K-edge of iron ($E_0 = 7.11$ keV).

consistent real space multiple-scattering approach based on a self-consistent muffin-tin scattering potential. For a given cluster of atoms around the absorber, FEFF calculates the phase and amplitude functions for different single and multiple-scattering paths of the emitted photo-electron. The cluster of atoms can be generated by the online software Atoms [113]. To generate the cluster, Atoms needs information on the atomic number, space group and lattice parameter of the selected element. When all the parameters are inserted, Atoms generates the general input file for FEFF containing all the structural and electronic information for the considered material.

In Fig. 2.19 three simulated spectra representing the K-edge XANES as a function of relative photon energy ($E - E_0$) of the hcp, bcc and fcc phase of iron are reported. The obtained spectral profiles, are characterized by a shoulder and several humped structures. The shoulder structure (**a**) located at approximately 5 eV above the edge energy E_0 , commonly appears in all

the obtained spectra, whereas the profile consisting of peaks **b**, **c** and **d** is different. The XANES profile of bcc Fe is characterized by the prominent peak **b** located on the crest. On the other hand, a double-peak structure composed of peaks **c** and **d** is associated with the close-packed structures fcc and hcp. Even though, the spectra for the fcc and hcp are very similar, the relative intensity between the peaks **c** and **d** are different. In particular, the peak **c** less intense than the peak **d** in the hcp structure, becomes the most intense of the two in the fcc structure.

From a comparison of the simulated spectra and the ones experimentally obtained with energy dispersive XAFS, is thus possible to perform a *time-resolved* characterization of the phase transitions undergone by the probed sample.

Chapter 3

High pressure - high temperature metrology

This chapter surveys the techniques adopted to perform reliable measurement of pressure and temperature in a laser-heated diamond anvil cell experiment. We have also examined whether a rhenium gasket can be used as a pressure gauge for multi Mbar experiments using its XRD signal.

3.1 Introduction

The determination of the phase diagram of a material, requires a reliable measurement of the pressure and temperature conditions at which a particular phase is observed.

However, in DAC experiments, a direct relation between the pressure exerted on the sample and the one exerted on the diamond's back is not easy to estimate because of the diamond's deformation with increasing pressure [114, 70]. It is thus necessary to measure the pressure *in situ* by placing a pre-calibrated pressure gauge near the sample in the high pressure chamber of a DAC.

The temperature can be directly measured (under certain approximations) by pyrometry i.e. by analyzing the intensity irradiated from the heated surface to the Planck's law. However, the approximations made can lead to erroneous measurement of the temperature and an accurate analysis of the obtained signal must be performed to check the obtained results.

In this chapter, the pressure gauges adopted in this work will be reviewed and the approximations made for the pyrometry measurement will be discussed together with the method used to check the temperature measurement.

3.2 Measuring P in a DAC

Unlike for shock-wave experiments, where the pressure is directly determined according to the Rankine-Hugoniot equations [2] which express the conservation of mass, momentum and internal energy during a shock process, in static compression experiments the pressure cannot be directly measured. Therefore, luminescence gauges and X-ray gauges must be used for an *in situ* measurement of the pressure.

3.2.1 The ruby gauge

Forman et al. [115] first showed that the luminescence doublet of peaks R_1 and R_2 of Cr^{3+} -doped Al_2O_3 (ruby) shifts with hydrostatic pressure in the range of 1-22 kbar, and that the two lines broaden if the ruby experiences non-hydrostatic stresses. *Barnett et al.* [116] described the optical system they used to perform quantitative pressure measurements using a ruby gauge in a DAC. In this method [116] a tiny chip of ruby (5-10 μm) is placed in the pressure medium along with the sample, and its luminescence is excited by a doubled YAG laser (532 nm) and analyzed by a monochromator. The shift in wavelength is followed as a function of pressure. The calibration

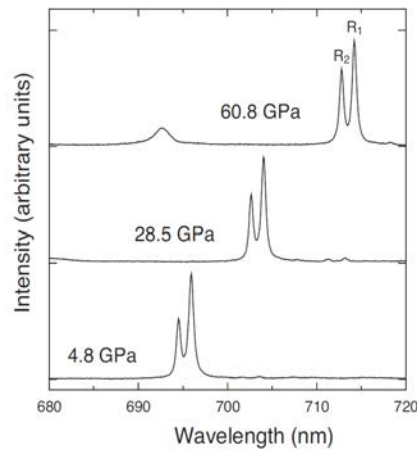


Figure 3.1: Representative ruby luminescence spectra taken at different pressures in a He pressure medium. The figure has been taken from Ref. [117].

procedure for the R -line shift with pressure, is to measure the wavelengths (λ_R) of the R -lines and simultaneously, by using X-ray diffraction, the molar volume V_M of a marker compound of known equation of state, assumed to

be exposed to the same stress conditions as the ruby.

Over the years, several calibration have been used. To date, the most popular calibration is due to *Mao et al.* [118] and is based on the measurements of the R_1 line shift of ruby luminescence in Ar pressure medium up to a pressure of 80 GPa. The pressure was determined from the room-temperature isotherms of Cu and Ag reduced by *Carter et al.* [119] from shock-wave data. The resulting pressure scale of *Mao et al.* [118] is expressed as:

$$P = \frac{A}{B} \left[\left(\frac{\lambda}{\lambda_0} \right)^B - 1 \right] \quad (3.1)$$

where P is the pressure in GPa, $A = \lambda(\partial P / \partial \lambda) = 1904$ GPa, $B = 7.665$, λ_0 is the wavelength of the luminescence at ambient P and need to be measured for each ruby (~ 694.24 nm). However, important improvement of this calibration to higher pressure have been performed since the use of He as quasi-hydrostatic pressure transmitting medium up to 100 GPa [120, 121, 122] (read the work of *Syassen* [123] for a detailed review). All the recently proposed ruby's pressure scale arrive at roughly the same correction of 7 % to the extrapolated scale of Ref.[118] at $P = 150$ GPa. During this work we have adopted the pressure scale proposed by *Dorogokupets et al.* in 2007 [122]. According to [122], the relation between the pressure and the R_1 shift is expressed by:

$$P = 1884 \left(\frac{\Delta\lambda}{\lambda_0} \right) \left(1 + 5.5 \frac{\Delta\lambda}{\lambda_0} \right) \quad (3.2)$$

where $\Delta\lambda = \lambda - \lambda_0$. In Ref. [124], the uncertainty in the pressure measurement with this calibration scale have been reported to be of the order of 2.5 GPa at 160 GPa.

The position of the ruby luminescence lines varies with T with a slope of 0.068 \AA/K , which means that a $\Delta T \sim 0.5$ K produces the same shift as the application of a pressure of 0.01 GPa. Above ~ 400 K, the fluorescence lines also broaden. Temperature effects on the ruby luminescence spectrum scale has been studied in the 1990s [125, 126] and more recently up to 95 GPa and 800 K [127]. In this work, we have used ruby gauge only at ambient temperature.

3.2.2 X-ray gauge

In high pressure experiment where an X-ray source is used it is possible to evaluate by the means of X-ray diffraction techniques, the evolution with pressure of the lattice parameters of a standard material whose equation of state $P(V, T)$ is known. Placing the standard material together with the sample in the high pressure chamber of a DAC and supposing the two materials to experience the same stress, we can measure the pressure on the sample.

At ambient temperature, $P(V, 300 \text{ K})$ EOS reduced from shock-wave measurements [128, 129, 130] are generally used to calibrate the X-ray gauges. The accuracy of these EOS are cross-checked by compressing several standards in the DAC and comparing the corresponding pressure obtained from the volumes measured by XRD [121, 131].

At higher temperature, the total pressure can be expressed according to Ref. [2]:

$$P(V, T) = P(V, 300K) + (P_{Th}(V, T) - P_{Th}(V, 300K)) \quad (3.3)$$

where $P(V, 300 \text{ K})$ represents the ambient temperature part of the total EOS and P_{Th} is the thermal pressure essentially created by the thermal motion of the atoms in the lattice.

The accuracy of the measured P can be determined from:

$$\Delta P = \left(\frac{\partial P}{\partial V} \right)_T \Delta V + \left(\frac{\partial P}{\partial T} \right)_V \Delta T \quad (3.4)$$

where ΔV and ΔT are respectively the uncertainties of the measured V and T . From thermodynamic relations Eq. 3.4 can be expressed as:

$$\Delta P = K_T \frac{\Delta V}{V} + \alpha K_T \Delta T \quad (3.5)$$

Where K_T is the isothermal bulk modulus and α represents the volumetric thermal expansion coefficient. Thus, considering a typical $\Delta V/V \sim 10^{-3}$ [121, 124], the pressure at ambient temperature ($\Delta T=0$) of a standard material with a K_T of the order of 200 GPa will be measured with an accuracy of the order of 0.2 GPa according to Eq. 3.5.

In this project the pressure reached at high temperature conditions, have been measured using KCl and Fe as X-ray gauges.

- For the KCl, we have used a semi-empirical thermal EOS built in Ref. [132]. In this work, the ambient temperature part of the total pressure (Eq. 3.3) has been obtained by fitting the P - V data obtained in the XRD experiment up to 178 GPa to the Rydberg-Vinet [133] equation of state. The pressure has been measured with a ruby gauge following the calibration of *Dorogokupets et al.* [122].

The thermal part of the equation of state has been calculated by molecular dynamic simulations and was found to vary linearly according to:

$$P_{Th}(V, T) - P_{Th}(V, 300K) = \int_{300}^T \left(\frac{\partial P}{\partial T} \right)_V dT = \int_{300}^T \alpha K_T dT \simeq \overline{\alpha K_T} (T - 300) \quad (3.6)$$

where $\overline{\alpha K_T} = 0.00224 \text{ GPa/K}$.

The total EOS is thus expressed as ($x = \frac{V}{V_0}$):

$$P(V, T) = 3K_0 x^{-\frac{2}{3}} (1 - x^{\frac{1}{3}}) \exp \left\{ 1.5(K'_0 - 1)(1 - x^{\frac{1}{3}}) \right\} + \overline{\alpha K_T} (T - 300) \quad (3.7)$$

where V_0 , K_0 and K'_0 are respectively the ambient pressure volume, the bulk modulus and its pressure derivative and their values are respectively 32.82 cm³/mol, 17.2 GPa and 5.89.

According to Eq. 3.5, for a temperature overestimation of 1000 K (ΔT), the use of the KCl EOS of [132] would lead to an overestimation of the pressure of only 2 GPa.

- The thermal equation of state of the ϵ -Fe has been semi-empirically determined in Ref. [134] using X-ray diffraction, shock wave data [135] and *ab initio* modeling [136].

As in the KCl case, the ambient temperature part of the total pressure (Eq. 3.3) has been determined by fitting the P - V values obtained from X-ray diffraction experiment up to 200 GPa to the Rydberg-Vinet formulation of equation of state. The pressure has been measured with ruby and W gauges calibrated according to Ref. [122]. The obtained V_0 , K_0 and K'_0 are respectively 6.753 cm³/mol, 163.4 GPa and 5.38.

The thermal pressure P_{Th} has been expressed using a formalism simplified from Ref.[137]:

$$P_{Th}(V, T) = \frac{9R\gamma}{V} \left(\frac{\theta}{8} + T \left(\frac{T}{\theta} \right)^3 \int_0^{\frac{\theta}{T}} \frac{z^3 dz}{e^z - 1} \right) + \frac{3}{2} \frac{R}{V} m a_0 x^m T^2 + \frac{3}{2} \frac{R}{V} g e_0 x^g T^2 \quad (3.8)$$

$R=8.314$ J/(mol·K) is the gas constant. The first term on the right-hand side of Eq. 3.8 is the quasi-harmonic Debye thermal pressure [2], which represents the main part of P_{Th} . The second and third terms are, respectively, the anharmonic and electronic thermal pressure. Their parameters have been obtained by fitting the corresponding terms *ab initio* obtained [136]: $a_0=3.7 \times 10^{-5}$ K⁻¹, $m=1.87$, $e_0=1.95 \times 10^{-4}$ K⁻¹, $g=1.339$.

The Debye temperature (θ) of ϵ -Fe under ambient condition has been fixed to 417 K [138]. The Grüneisen parameters γ has been derived from shock-wave data up to 200 GPa together with the X-ray diffraction data at ambient temperature and is expressed in the following form ($x = \frac{V}{V_0}$):

$$\gamma = 1.305 + 0.57x^{3.289} \quad (3.9)$$

In this case, a ΔT of 1000 K in the temperature measurement would lead to an uncertainty of ~ 10 GPa in the measured P .

- The EOS of the γ -Fe has been empirically constructed in Ref. [139] from XRD data obtained from internally-heated DAC experiment up to 69 GPa and 2400 K. The pressures have been measured in the ϵ - γ coexistence region of Fe using the equation of state of *Dewaele et al.* [134] for ϵ -Fe.

The ambient temperature part of the total EOS has been represented with a third order Birch-Murnaghan equation of state [2] and the volumetric

thermal expansion has been evaluated fitting the obtained P - V - T data to the Anderson-Grüneisen relation [140]:

$$\frac{\partial \ln \alpha}{\partial \ln V} = \delta_T = \delta_0 x^k \quad (3.10)$$

where δ_T is the Anderson-Grüneisen parameter, δ_0 is its value at ambient pressure and k is the dimensionless thermoelastic parameter.

According to Ref. [139], the total EOS of the γ phase of iron can be expressed as:

$$P(V, T) = \frac{3}{2} K_0 \left(x^{-\frac{7}{3}} - x^{-\frac{5}{3}} \right) \left[1 - \frac{3}{4} (4 - K'_0) (x^{-\frac{2}{3}} - 1) \right] + 0.009(T - 300) \quad (3.11)$$

In this expression V_0 , K_0 and K'_0 are from [141] and are respectively 6.835 cm³/mol, 165.3 GPa and 5.5.

In this case, the uncertainty in the pressure measurement for a ΔT of 1000 K would be of the order of 10 GPa.

3.2.3 The case of Rhenium

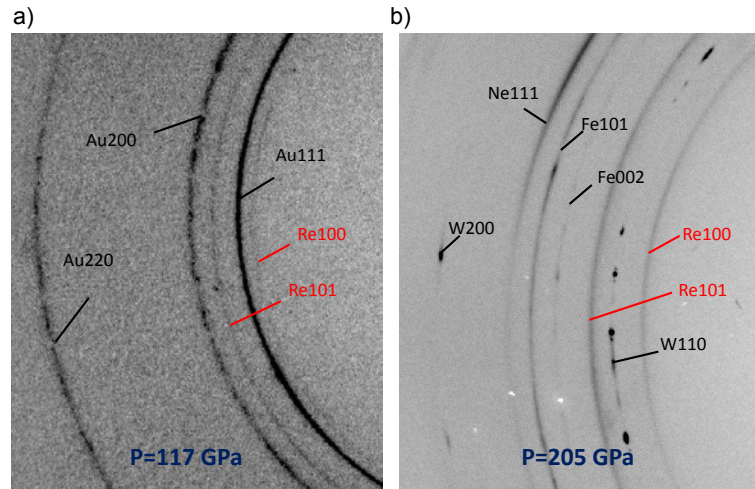


Figure 3.2: Examples of X-ray diffraction patterns in which the signal from the Re gasket is visible (indicated in red) for experiments performed with Au (a) and Fe + W samples (b) at 117 and 205 GPa respectively.

As we have seen in the previous paragraphs, pressure measurement in a DAC implies the use of pressure gauges placed in the high pressure chamber

together with the sample.

For experiment at ultra-high pressure, the diameter of the obtained high pressure chamber is less than $10\ \mu\text{m}$ and adding new material is not always possible. However, the XRD signal of the gasket is always present in such experiments (Fig. 3.2). For these reasons we wondered if this signal can be used for pressure calibration purpose for experiments in the multi-Mbar range. At this purpose, the quasi-hydrostatic EOS of Re (generally used as gasket material for experiment above 100 GPa) has been measured and compared to the one previously measured by *Dubrovinsky et al.* [142]. This comparison shows a progressive divergence of the two EOS. For the same volume, the pressure obtained from the EOS of *Dubrovinsky et al.* is up to 13 % higher than in our measurement. This difference has been explained by a non-hydrostatic compression of Re in Ref. [142].

The pressure and volume obtained from the gasket signals of several high pressure experiments have been compared with our Re EOS. This comparison has led to the conclusion that the diffraction signal from the Re gasket can be used for pressure estimation at multi-Mbar pressure within 5 %, if the signal is taken at the sample/gasket interface.

In the following, a paper published on the *Journal of Applied Physics* in which the obtained results are discussed is reported.

Equation of state of rhenium and application for ultra high pressure calibration

Simone Anzellini,¹ Agnès Dewaele,¹ Florent Occelli,¹ Paul Loubeyre,¹
 and Mohamed Mezouar²

¹CEA, DAM, DIF, F-91297 Arpajon, France

²European Synchrotron Radiation Facility, BP220, 38043 Grenoble Cedex, France

(Received 20 December 2013; accepted 13 January 2014; published online 24 January 2014)

The isothermal equation of state of rhenium has been measured by powder X-ray diffraction experiments up to 144 GPa at room temperature in a diamond anvil cell. A helium pressure transmitting medium was used to minimize the non-hydrostatic stress on the sample. The fit of pressure-volume data yields a bulk modulus $K_0 = 352.6$ GPa and a pressure derivative of the bulk modulus $K'_0 = 4.56$. This equation of state differs significantly from a recent determination [Dubrovinsky *et al.*, Nat. Commun. **3**, 1163 (2012)], giving here a lower pressure at a given volume. The possibility of using rhenium gasket X-ray diffraction signal, with the present equation of state, to evaluate multi-Mbar pressures in the chamber of diamond anvil cells is discussed. © 2014 AIP Publishing LLC. [<http://dx.doi.org/10.1063/1.4863300>]

I. INTRODUCTION

Rhenium (Re) belongs to the group VII of transition metals with a half filled *d* band. The crystalline structure observed for this metal is hexagonal close packed (hcp) up to 660 GPa.^{1–4} First principle calculations⁵ predict that hcp is more stable against other simple structures up to 1000 GPa at least. Surprisingly, the equation of state (EOS) of hcp rhenium measured in diamond anvil cells under non-hydrostatic compression³ does not significantly deviate from the recent measurements under quasi-hydrostatic compression in helium pressure transmitting medium.⁴ This is in contrast to what has been reported for other metals, such as Ta.⁶ Also, there is a disagreement between the EOS of rhenium measured using shock wave experiments, reduced to ambient temperature⁷ and the most recent static measurement under quasi-hydrostatic conditions.⁴ The two compression curves, which should be identical, differ by 15% in pressure, for the same compression, around 150 GPa.

Rhenium is ductile but has high bulk and shear moduli,⁸ a high strength,^{9,10} and a high melting point—3453 K, the second of all metals. For these reasons, rhenium has been used as a gasket material for studies under ultra-high pressures in diamond anvil cell. The fact that a rhenium gasket is present in the vast majority of diamond anvil cell experiments performed above 100 GPa makes it a convenient potential pressure X-ray calibrant. In fact, adding new materials in a few micrometers-sized pressure chamber of multi-Mbar experiments⁴ is not always possible. For that purpose, a reference EOS has to be established. In addition, it should be determined whether the specific volume of the gasket measured by X-ray diffraction (XRD) can be used for pressure determination without any bias. In fact, the gasket being directly compressed between the anvils, its stress state is complex and probably different from one experiment to another.

We present here data taken under quasi-hydrostatic compression, which reconcile static and dynamic measurements of the EOS of rhenium. We also analyze the XRD signal of

rhenium gaskets recorded during several ultra-high pressure experiments, and we evaluate to which extent this signal can be used with the present EOS for an estimation of the sample pressure.

II. MEASUREMENTS WITH HELIUM PRESSURE MEDIUM

Three different experimental runs were carried on the ID27 and ID09 beamlines of the European Synchrotron Radiation Facility. For each run, a sample composed of a grain of powder of Re (Alpha Aesar product, 99.99% purity) was embedded in helium pressure transmitting medium and put a few micrometers away from the pressure gauge in the high pressure chamber of a diamond anvil cell. Re was also used as the gasket material, but thanks to the dimension of the X-ray spot size ($2 \times 3 \mu\text{m}$), much smaller than the high pressure chamber diameter ($20 \mu\text{m}$ minimum), we were able to collect only the signal scattered by the rhenium grain. The pressure was measured from the luminescence of a ruby gauge or from the measurement of the atomic volume of helium pressure medium or tungsten X-ray gauge (see Table I). Tungsten has been chosen as an X-ray pressure gauge because of its high X-ray scattering power and the accuracy of its EOS, attested by the consistency between static, dynamic, and ultrasonic measurements.^{11,12} The calibration of ruby and tungsten gauges has been taken from Ref. 13. The calibration of helium gauge is from Ref. 14, with a modification that takes into account the update of the ruby pressure scale.^{11,13}

The monochromatic XRD signal has been collected on image plates. The diffraction geometry was determined using LaB₆ and Si reference samples. The signal was circularly integrated using the FIT2D¹⁵ software. Fig. 1 shows the raw and integrated angle-dispersive XRD pattern of Re at different pressures. All the diffraction peaks belong to the hcp structure. The diffraction lines (100), (002), (101), (102), (110), (103), and (112) have been used for the measurement

TABLE I. Conditions of each experimental run. Sizes are in μm ; PTM: pressure transmitting medium.

Run	P range (GPa)	P gauge	PTM	Diamond's culet size	Sample size
1	0.64–36.9	Ruby	He	300	4
2	14.0–64.8	He	He	150	3
3	1.45–144	W + Ruby	He	100	3

of the lattice parameters. The raw images of the powder sample show diffraction rings with some texturing, which was already present in the starting sample. With increasing pressure, the diffraction peaks become larger, which is a sign of an increase of the micro-stress in the sample.¹⁶ This micro-stress is different from the macroscopic non-hydrostatic stress, which is qualitatively discussed in the next section.

A. Macroscopic non-hydrostatic stress

It is desirable to achieve purely hydrostatic conditions in the sample chamber of a diamond anvil cell, which would be provided by a liquid pressure transmitting medium. However, even helium becomes solid above about 12 GPa at room temperature and is therefore prone to sustain a

non-hydrostatic stress in the sample chamber. In addition, even at lower pressure, the stress on the sample can become non-hydrostatic if it bridges the anvils due to excessive thinning of the gasket or due to a large initial thickness of the sample. The macroscopic stress in a sample can be determined by an analysis of the measured XRD spectra,¹⁶ if the diffraction lines exhibit a measurable shift from hydrostatic compression. Table II shows the interplanar spacings measured at the highest pressure reached (144 GPa) in our experiments. They deviate from the spacings calculated using the lattice parameters obtained by a refinement of the whole spectrum by less than 0.06%. This deviation corresponds to the uncertainty on the measurement of each diffraction peak. We can thus conclude that the non-hydrostatic stress is below the detection limit of our measurements. That is in agreement with the quantification of the macroscopic non-hydrostatic stress on metals embedded in helium that reaches 0.5 GPa at 150 GPa.¹⁷

B. Evaluation of the micro-stress

From the analysis of the width of the XRD lines, it is possible to estimate the micro-stress in a powder material, i.e., the difference in stress between the crystallites that constitute the powder.¹⁶ This difference causes a broadening of each XRD peak identified by its Miller indices (hkl), which can be expressed as¹⁷

$$(2w_{hkl}\cos\theta_{hkl})^2 = (2w_{hkl}^0\cos\theta_{hkl})^2 + \eta_{hkl}^2 \sin^2 \theta_{hkl}, \quad (1)$$

where $2w_{hkl}$ is the full-width at half maximum (FWHM) of the diffraction angle $2\theta_{hkl}$, $2w_{hkl}^0$ its value at $P=0$, η_{hkl} the micro-strain on the (hkl) plane related to the micro-stress σ via

$$\sigma = \eta_{hkl}E(hkl)/2, \quad (2)$$

where $E(hkl)$ is the single crystal Young modulus along the direction (hkl). An approximate expression for the average micro-stress is

$$\sigma = \langle \eta_{hkl} \rangle E/2, \quad (3)$$

where $\langle \eta_{hkl} \rangle$ represents the average value of η_{hkl} over measured diffraction peaks and E the Young modulus of the

TABLE II. Measured reflections for rhenium at 144 GPa. (hkl) are the Miller indices of the reflection. d_m is the corresponding interreticular distance measured by individual peak fitting. d_{calc} is the interreticular distance calculated by a fit of the whole spectrum.

(hkl)	d_m (\AA)	d_{calc} (\AA)	$d_m - d_{calc}$ (\AA)
(100)	2.2116	2.2103	0.0013
(002)	2.0550	2.0561	-0.0011
(101)	1.9480	1.9469	0.0011
(102)	1.5056	1.5054	0.0001
(110)	1.2765	1.2761	-0.0004
(103)	1.1650	1.1649	0.0001
(112)	1.0834	1.0843	-0.0009

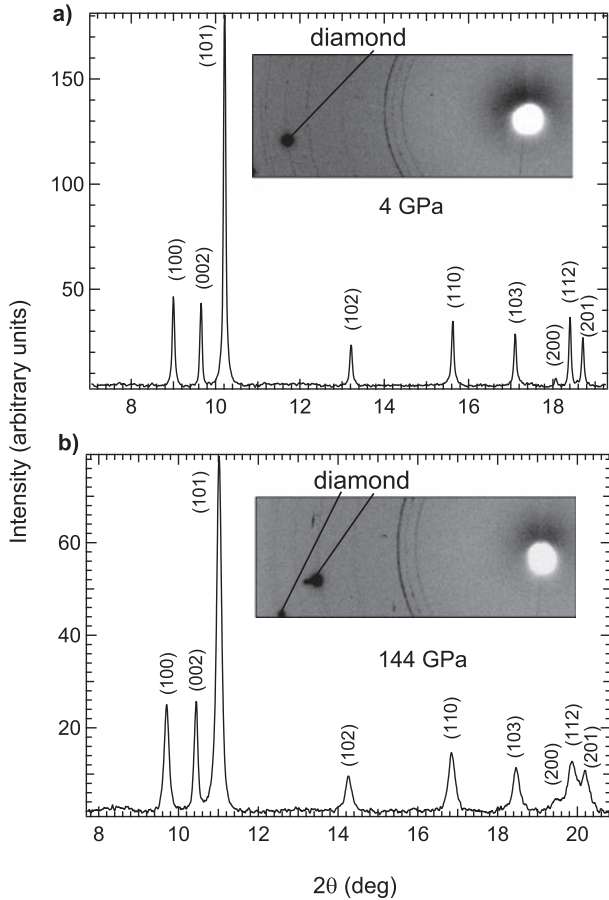


FIG. 1. Integrated powder X-ray diffraction patterns of Re at low (a) and high (b) pressure. The insets show a part of the recorded raw diffraction images. The diamond contribution to the X-ray raw spectra are masked during the integration.

polycrystalline aggregate.¹⁸ E is related to the bulk and shear moduli K and G of the aggregate

$$E = \frac{9KG}{3K + G}. \quad (4)$$

The variation of E with pressure have been computed using one Re EOS,⁷ and the extrapolation of ultrasonic data⁸ using the relation¹⁰

$$G = G_0 x^{-\frac{5}{3}} \left[1 + \frac{1}{2} \left(\frac{3K_0 G'_0}{G_0} - 5 \right) (x^{-\frac{2}{3}} - 1) \right], \quad (5)$$

with $x = V/V_0$, $G_0 = 179$ GPa, and $G'_0 = 1.8$.⁸ The micro-stress σ has been estimated using Eqs. (1) and (3) for seven diffraction peaks and is plotted on Fig. 2. It increases from 0 at the beginning of the experiment to $\simeq 7$ GPa at 144 GPa. These values are smaller than the macroscopic uniaxial stress sustained by a rhenium sample (yield strength) compressed directly between the anvils, measured in two studies.^{3,9} In Ref. 3, the measured yield strength of Re exceeded 20 GPa at 120 GPa. It is expected that the micro-stress is upper bounded by the yield strength: our measurements are thus compatible with earlier yield strength estimates.^{3,9} This micro-stress is isotropic and so does not affect the EOS measurements whereas the macroscopic stress leads to measurable effects.

C. Equation of state

The bulk modulus K_0 , its pressure derivative K'_0 , and the volume V_0 at ambient pressure are determined by a least-squares fit of the present pressure-volume data (Table III) to the Rydberg-Vinet²⁰ EOS formulation ($x = V/V_0$):

$$P(V) = 3K_0 x^{-\frac{2}{3}} (1 - x^{\frac{1}{3}}) \exp \left\{ 1.5 (K'_0 - 1) \times (1 - x^{\frac{1}{3}}) \right\}. \quad (6)$$

The resulting values are as follows: $V_0 = 8.8726 \pm 0.01$ cm³/mol, $K_0 = 352.6 \pm 8$ GPa and $K'_0 = 4.56 \pm 0.17$. The current and literature EOS parameters are listed in Table IV. The error bars correspond to the 95% confidence interval of the fitted values. The current EOS agrees with the EOS based on shock experiments reduced to ambient temperature⁷ (Fig. 3) and with earlier measurements performed in a moderate pressure range.^{1,9} It also agrees with a recent density-functional theory calculation within generalized

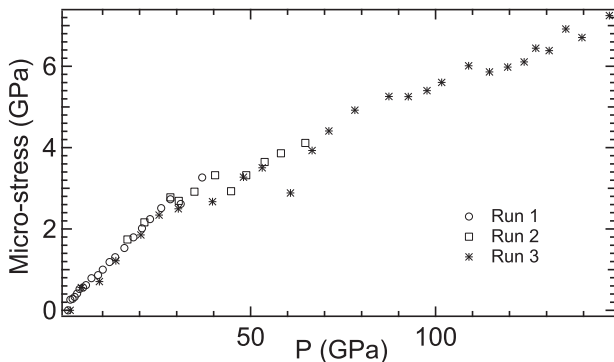


FIG. 2. Micro-stress in the rhenium sample as a function of pressure.

TABLE III. Measured pressures in GPa (P_R : ruby pressure, P_W : tungsten pressure, and P_{He} : helium pressure) and lattice parameters of tungsten (a_W) and rhenium (a and c) for the three experimental runs. The data are listed in the order they have been taken. Experimental uncertainty on lattice parameters is lower than 0.003 Å. Uncertainty on pressure measurement increases from 0.05 GPa at 1 GPa to $\simeq 2$ GPa at 150 GPa.¹⁹

Run	P_R	P_{He}	a (Å)	c (Å)	Run	P_W	a_W (Å)	a (Å)	c (Å)
1	0.65		2.7619	4.4590	3	1.42	3.1599	2.7587	4.4536
	1.26		2.7598	4.4557		4.43	3.1500	2.7501	4.4416
	1.88		2.7579	4.4526		9.31	3.1347	2.7388	4.4223
	2.43		2.7561	4.4499		13.8	3.1216	2.7275	4.4039
	3.07		2.7546	4.4472		20.5	3.1031	2.7131	4.384
	3.74		2.7531	4.4446		25.3	3.0904	2.7035	4.3668
	4.69		2.7506	4.4410		30.5	3.0777	2.6958	4.3514
	5.48		2.7485	4.4372		39.6	3.0566	2.6791	4.3245
	6.96		2.7449	4.4310		47.8	3.0390	2.6670	4.3016
	8.77		2.7407	4.4247		52.8	3.0289	2.6577	4.2916
	10.0		2.7372	4.4196		60.3	3.0143	2.6478	4.2706
	11.9		2.7331	4.4134		66.1	3.0038	2.6395	4.2590
	13.4		2.7295	4.4063		70.5	2.9959	2.6308	4.2476
	15.9		2.7240	4.3994		77.4	2.9841	2.6238	4.2350
	18.3		2.7183	4.3901		86.3	2.9694	2.6112	4.2117
	20.6		2.7137	4.3815		91.5	2.9614	2.6063	4.2013
	22.8		2.7088	4.3739		96.4	2.9540	2.6003	4.1896
	25.8		2.7033	4.3637	100	2.9482	2.5947	4.1847	
	28.3		2.6989	4.3574	107	2.9380	2.5872	4.1709	
	31.1		2.6943	4.3475	113	2.9304	2.5819	4.1622	
	36.9		2.6847	4.3322	118	2.9238	2.5770	4.1549	
2		16.7	2.7225	4.3943	122	2.9182	2.5719	4.1472	
		21.3	2.7140	4.3802	125	2.9141	2.5696	4.1429	
		28.3	2.6995	4.3588	129	2.9096	2.5649	4.1358	
		30.6	2.6958	4.3511	133	2.9041	2.5620	4.1308	
		34.8	2.6883	4.3400	137	2.8989	2.5582	4.1226	
		40.4	2.6797	4.3241	144	2.8902	2.5537	4.1147	
		44.7	2.6740	4.3132					
		48.8	2.6643	4.3002					
		53.8	2.6580	4.2880					
		58.2	2.6505	4.2779					
		64.8	2.6422	4.2636					

gradient approximation.²¹ However, it progressively diverges from the EOS recently measured⁴ using diamond anvil cell and helium pressure transmitting medium as the pressure increases. For the same volume, the pressure is higher by up to 13% in Ref. 4 measurements than in our measurements. Only a very small part of this difference can be attributed to pressure gauges calibration issues: if the calibration of Ref. 22 is used for gold X-ray gauge, instead of the calibration of Ref. 23 used in work of Dubrovinsky *et al.*, the pressures differ by less than 2% (see Fig. 3(a), open circles). The calibration of Ref. 22 has been shown to be compatible with the current gauges calibration.¹¹ The difference between the two sets of data can only be explained by a non-hydrostatic compression of the rhenium sample in Ref. 4 experiments, for instance, by a direct compression of the sample between the diamond anvils. In fact, in the conventional diffraction geometry in diamond anvil cells, the volume is overestimated under non-hydrostatic compression and Ref. 4 set of data agree with the measurements of Jeanloz *et al.*,³ where the sample was non-hydrostatically compressed. The large difference between the yield strength of

TABLE IV. EOS parameters of rhenium measured in different experiments. The volume V_0 , bulk modulus K_0 and its pressure derivative K'_0 are listed. Experimental methods and EOS formulation are specified. PTM: Pressure transmitting medium; XRD: X-ray diffraction; DAC: diamond anvil cell; BM: Birch-Murnaghan; GGA-PBE: generalized gradient approximation—Perdew Burke Ernzerhof.

Reference	V_0 (cm ³ /mol)	K_0, K'_0 (GPa, no unit)	P range (GPa)	PTM	Pressure gauge	EOS	Method
This study	8.8726	352.6, 4.56	0.64–144	He	Ruby, W, He	Vinet	XRD in DAC
Ref. 1		336, 4 ^a	0–35	NaCl	NaCl	BM	XRD in DAC
Ref. 7		365.2, 4.35	0–280			Vinet	Reduced Shock
Ref. 8		360.3, 5.43	0.00–0.42				Ultrasound
Ref. 4	8.87	348, 6.07 ^b	0–165	He	Au ²³	Vinet	XRD in DAC
Ref. 4	8.87	353, 5.80	0–165	He	Au ²³	BM3	XRD in DAC
Ref. 21	8.842	376, 4.58	0–200			Vinet	GGA-PBE

^aFixed parameter.

^bThe published value $K'_0 = 7.57$ has been modified because it was incompatible with P - V data points.

rhenium^{3,9} and gold (which is much lower¹⁷) would imply that the overestimate of sample and pressure marker volume under non-hydrostatic compression do not compensate. The compression curve measured in Ref. 4 becomes so stiff with increasing pressure that a fourth-order Birch-Murnaghan EOS is needed to fit the P - V data. It is not needed with the current measurements. Our data suggest that if the Re EOS established by Dubrovinsky *et al.*⁴ is used to calibrate the pressure in a diamond anvil cell, it will overestimate P by already 40 GPa around 200 GPa, an overestimation which will further increase with increasing pressure: a real pressure of 450 GPa would

correspond to a pressure of 600 GPa estimated using the calibration of Dubrovinsky *et al.*

III. USE OF Re GASKET AS AN X-RAY PRESSURE CALIBRANT

In this section, we phenomenologically discuss whether the Re gasket XRD signal can be used to estimate the pressure in the sample chamber of a diamond anvil cell. For that purpose, we have analyzed the XRD signal from the gasket collected in five experiments, where the sample pressure had been accurately measured using a pre-calibrated luminescence or X-ray marker. The conditions of these experiments are summarized in Table V. In all cases, the X-ray spot was located $\approx 5 \mu\text{m}$ away from the visual edge of the gasket, a distance slightly larger than the FWHM of the X-ray spot ($2\text{--}3 \mu\text{m}$). The collected signal was therefore scattered by the most inner part of the gasket; i.e., very close to its edge with the pressure chamber. Runs with pressure media considered as soft (He, Ne) or harder (KCl, Xe), with (runs 4 and 5) or without (runs 1–3) thermal annealing, and with a large (runs 1–3) or small (runs 4 and 5) gasket deformation during loading have been considered, so that these data represent the various gasket stress conditions in diamond anvil cell experiments.

Fig. 4(a) compares the measured volume of rhenium gasket with the volume of rhenium calculated at the sample pressure (estimated with the gauges summarized in Table IV), using the current quasi-hydrostatic EOS. The agreement between the two values is surprisingly good, the difference being smaller than 1.2%. In other words, the measured volume of Re gasket is close to what would have been expected

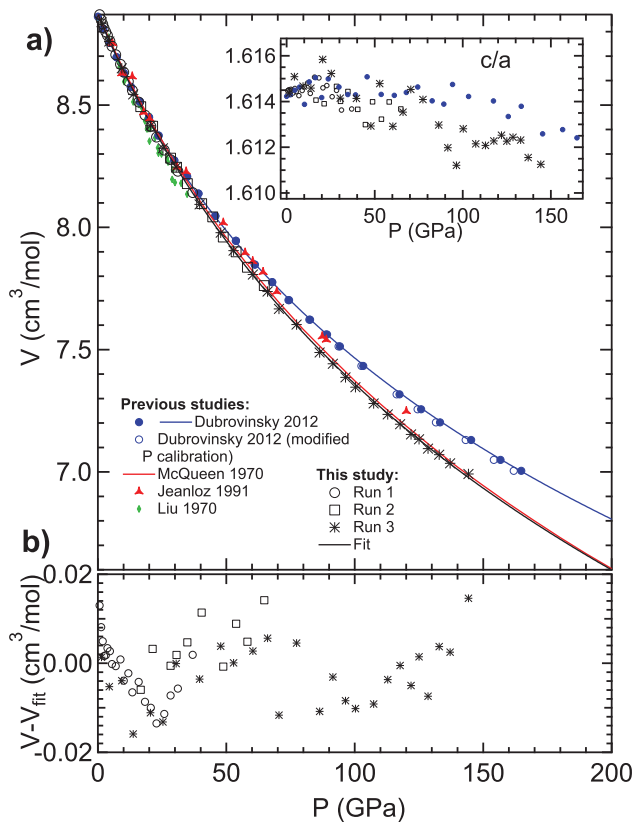


FIG. 3. (a) Measured volume of rhenium as a function of the pressure, compared with literature data. Inset: evolution of the c/a ratio. (b) Difference between measured and fitted volume, Vinet formulation with $V_0 = 8.8726$ cm³/mol, $K_0 = 352.6$ GPa, and $K'_0 = 4.56$.

TABLE V. Conditions of the runs for which the X-ray diffraction signal of the rhenium gasket has been analyzed here. PTM: pressure transmitting medium.

Run	P range (GPa)	P gauge	PTM	Published reference
1	28–131	Ruby ¹³	He	22
2	107–205	W ¹¹	Ne	24
3	141–259	Au ²²	Xe	25
4	64–204	Fe ²⁴	KCl	26
5	107–174	Fe ²⁴	KCl	26

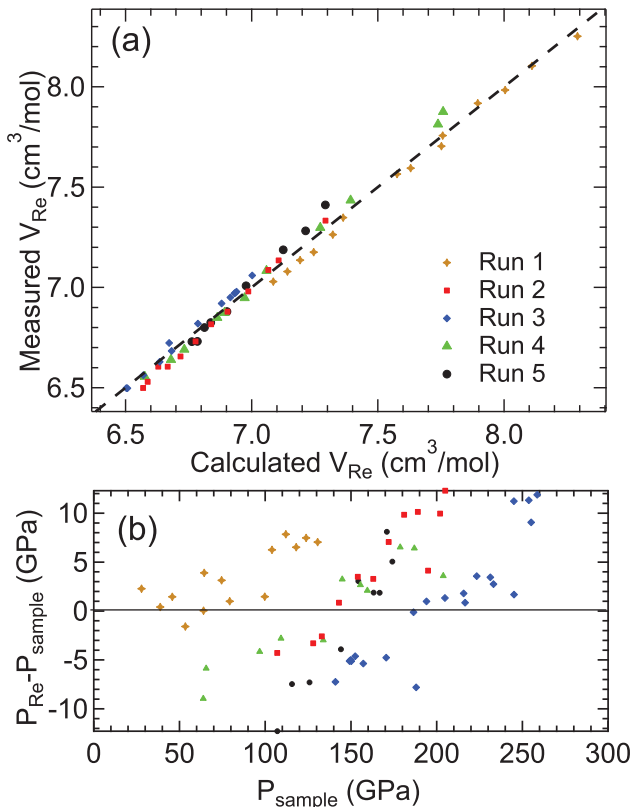


FIG. 4. (a) Volume of rhenium gasket measured by X-ray diffraction at the edge with the sample, as a function of the volume of rhenium calculated using the current quasi-hydrostatic EOS (Table IV, first line) at the sample pressure P_{sample} . The dotted line corresponds to measured volume = calculated volume. (b) Difference between P_{Re} (calculated using its quasi-hydrostatic EOS) and P_{sample} .

if Re had been compressed quasi-hydrostatically in the sample chamber. This contradicts the general view of an overestimate of volume in a material directly compressed between the anvils¹⁷ discussed above. This view is too simplistic here: it is possible that the innermost part of the gasket does not sustain a large non-hydrostatic stress because it is in contact with a relatively soft pressure medium. Indeed, preferred orientation, which is the signature of a large plastic strain under uniaxial loading, could not be detected in the XRD signal of the gaskets. However, we note that at very high pressure (low volume), the average measured volume becomes slightly smaller than the calculated volume (Fig. 4(a)), which means that a pressure from the gasket X-ray signal will be overestimated.

Fig. 4(b) shows the difference between the pressure which would have been estimated using the gasket EOS (P_{Re}) and the real sample pressure (P_{sample}). In practice, this would have been the error in pressure measurement if the gasket was used as a pressure gauge. The scatter of the measurements is large but does not drastically increase with pressure, even if above ≈ 200 GPa, the gasket has a trend to overestimate the pressure (by $\approx 5\%$ at most). We therefore propose that the use of rhenium gasket as pressure gauge can be done in a confidence interval of 5% up to 260 GPa if the XRD signal is taken at

the edge between the gasket and the high pressure chamber and the present quasi-hydrostatic rhenium EOS used. This proposal, which is based on a phenomenological approach, should be confirmed by the collection of similar data during future experiments, especially at higher pressure. We also stress that the gasket data have been collected with a micro-focused X-ray spot, and this method might not be applicable for larger beam sizes which would collect information from a large gasket volume with a heterogeneous stress state.

IV. CONCLUSION

The quasi-hydrostatic EOS of Re has been determined from a powder XRD experiment using He as a pressure transmitting medium up to 144 GPa. The XRD lines measured for rhenium show no evidence of non-hydrostatic compression. The volume, bulk modulus, and its pressure derivative at ambient pressure and temperature have been obtained with a Rydberg-Vinet EOS: $V_0 = 8.8726 \pm 0.01$ cm³/mol, $K_0 = 352.6 \pm 8$ GPa, and $K'_0 = 4.56 \pm 0.17$. This EOS agrees with shock compression data⁷ but contradicts a recent study carried out in diamond anvil cell.⁴ This suggests that the use of rhenium as an X-ray pressure gauge with the calibration using Ref. 4 data will lead to a large pressure overestimate (for instance, 600 GPa instead of 450 GPa). Using XRD, data collected on the rhenium gasket in various configurations of compression, we propose that this information and the current EOS could be used for pressure estimation at multi-Mbar pressures (within $\approx 5\%$ of the real pressure above 1 Mbar), if the diffraction signal is taken at the sample/gasket interface.

ACKNOWLEDGMENTS

The authors acknowledge the European Synchrotron Radiation Facility for provision of synchrotron radiation facilities on the beam lines ID27 and ID09. They thank M. Hanfland, C. Pépin, and R. Torchio for the help in the synchrotron experiment.

- ¹L. G. Liu, T. Takahashi, and W. A. Bassett, *J. Phys. Chem. Solids* **31**, 1345 (1970).
- ²Y. K. Vohra, S. J. Duclos, and A. L. Ruoff, *Phys. Rev. B* **36**, 9790 (1987).
- ³R. Jeanloz, B. K. Godwal, and C. Meade, *Nature* **349**, 687 (1991).
- ⁴L. Dubrovinsky, N. Dubrovinskaia, V. B. Prakapenka, and A. M. Abakumov, *Nat. Commun.* **3**, 1163 (2012).
- ⁵A. K. Verma, P. Ravindran, R. S. Rao, B. K. Godwal, and R. Jeanloz, *Bull. Mater. Sci.* **26**, 183 (2003).
- ⁶A. Dewaele, P. Loubeyre, and M. Mezouar, *Phys. Rev. B* **69**, 092106 (2004).
- ⁷R. G. McQueen, S. P. Marsh, J. W. Taylor, J. N. Fritz, and W. J. Carter, *High Velocity Impact Phenomenon* (Academic, New York, 1970).
- ⁸M. H. Manghnani, K. Katahara, and E. S. Fisher, *Phys. Rev. B* **9**, 1421 (1974).
- ⁹T. S. Duffy, G. Y. Shen, J. F. Shu, H. K. Mao, R. J. Hemley, and A. K. Singh, *Phys. Rev. B* **60**, 15063 (1999).
- ¹⁰A. K. Singh, J. Hu, J. Shu, H. K. Mao, and R. J. Hemley, *J. Phys.: Conf. Ser.* **377**, 012008 (2012).
- ¹¹A. Dewaele, P. Loubeyre, and M. Mezouar, *Phys. Rev. B* **70**, 094112 (2004).

- ¹²W. B. Holzapfel, *J. Appl. Phys.* **93**, 1813 (2003).
- ¹³P. I. Dorogokupets and A. R. Oganov, *Phys. Rev. B* **75**, 024115 (2007).
- ¹⁴P. Loubeyre, R. LeToullec, J. P. Pinceaux, H. K. Mao, J. Hu, and R. J. Hemley, *Phys. Rev. Lett.* **71**, 2272 (1993).
- ¹⁵A. Hammersley, S. Stevenson, M. Hanfland, A. Fitch, and D. Hausermann, *High Pressure Res.* **14**, 235 (1996).
- ¹⁶K. Takemura, *J. Appl. Phys.* **89**, 662 (2001).
- ¹⁷A. Dewaele and P. Loubeyre, *High Pressure Res.* **27**, 419 (2007).
- ¹⁸A. K. Singh, A. Jain, H. P. Liermann, and S. K. Saxena, *J. Phys. Chem. Solid* **67**, 2197 (2006).
- ¹⁹A. Dewaele, M. Torrent, P. Loubeyre, and M. Mezouar, *Phys. Rev. B* **78**, 104102 (2008).
- ²⁰P. Vinet, J. Ferrante, J. H. Rose, and J. R. Smith, *J. Geophys. Res.* **92**, 9319, doi:10.1029/JB092iB09p09319 (1987).
- ²¹M.-B. Lv, Y. Chang, Y.-Y. Qi, G.-F. Ji, and C.-G. Piao, *Physica B* **407**, 778 (2012).
- ²²K. Takemura and A. Dewaele, *Phys. Rev. B* **78**, 104119 (2008).
- ²³M. Yokoo, N. Kawai, K. G. Nakamura, K. Kondo, Y. Tange, and T. Tsuchiya, *Phys. Rev. B* **80**, 104114 (2009).
- ²⁴A. Dewaele, P. Loubeyre, F. Occelli, M. Mezouar, P. I. Dorogokupets, and M. Torrent, *Phys. Rev. Lett.* **97**, 215504 (2006).
- ²⁵A. Dewaele, P. Loubeyre, P. Dumas, and M. Mezouar, *Phys. Rev. B* **86**, 014103 (2012).
- ²⁶S. Anzellini, A. Dewaele, M. Mezouar, P. Loubeyre, and G. Morard, *Science* **340**, 464 (2013).

3.3 Measuring T in a LH-DAC

In LH-DAC experiment, the temperatures are determined by pyrometry. In fact, at the thermodynamic equilibrium, the light emitted by the surface of a body at uniform temperature T , follows the *Planck distribution*:

$$I_{Planck}(\lambda) = \epsilon \frac{2\pi hc^2}{\lambda^5} \frac{1}{e^{\frac{hc}{\lambda kT}} - 1} \quad (3.12)$$

where ϵ is the emissivity of the material ($\epsilon=1$ for a blackbody), c is the speed of light, h the Planck's constant, K the Boltzman's constant and λ is the wavelength of the emitted light.

The emissivity is a wavelength dependent quantity ($\epsilon=\epsilon(\lambda)$) and, the variation of this dependence within the P - T conditions of the experiment is generally unknown [143]. However, for the wavelength range collected in our LH-DAC experiment (450-900 nm), the emissivity variation with wavelength is generally considered negligible and the graybody approximation ($\epsilon < 1$) is assumed. Fig. 3.3 represents the variations of the emissivity of ϵ -Fe in the spectral range 450-900 nm at different pressures. The emissivity values have been extrapolated from measurements performed in the spectral range between 1500 nm and 1900 nm [144].

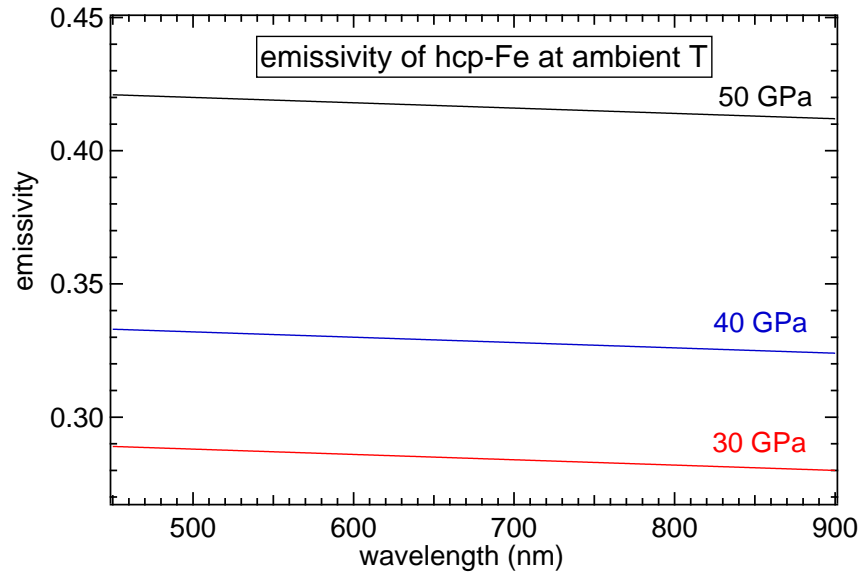


Figure 3.3: Emissivity for the hcp-Fe as a function of the wavelength at different pressure. The emissivity values are extrapolated from Ref. [144].

The temperature of the sample can be obtained from a fit of the radiance

data collected over a continuous wavelength range to the Planck distribution.

For temperature where $e^{\frac{hc}{\lambda kT}} \gg 1$, the Wien approximation to the Planck's law can be used:

$$I_{Wien}(\lambda) = \epsilon \frac{2\pi hc^2}{\lambda^5} e^{-\frac{hc}{\lambda kT}} \quad (3.13)$$

It is possible to define a linearized form of Eq. (3.13) through the Wien function:

$$Wien = \frac{K}{hc} \ln \left(I_{Wien} \frac{\lambda^5}{2\pi hc^2} \right) = \frac{K}{hc} \ln \epsilon - \frac{1}{\lambda T} \quad (3.14)$$

The obtained linear relationship between Wien and $1/\lambda$ is advantageous because deviations from linear behavior are easier to observe. The error in the temperature measurement introduced by using the Wien's approximation to Planck's law is of the order of 1 % on T at 5000 K [145, 146].

A complementary method that can underscores wavelength dependent deviations from the ideal Planck distribution is the two color pyrometry. Thanks to the linearity of the Wien function, the temperature can be determined using only two wavelengths. Thus, if the wavelength dependence of the emissivity can be neglected, a series of temperatures can be calculated from the ratio of a pairs of intensities separated by a fixed spectral difference. Defining $\omega_i = -\frac{hc}{K\lambda_i}$, the temperature can be obtained from:

$$T_{two-color} = \frac{\omega_2 - \omega_1}{Wien(\omega_2) - Wien(\omega_1)} \quad (3.15)$$

By scanning the selected spectral window across the measured spectral range, temperature can be determined as a function of wavelength. The wavelength interval must be chosen to be small enough to allow the observation of possible wavelength-dependent variation of $T_{two-color}$, but large enough so that the corresponding intensity difference is significant.

Regular data will have substantial noise, but the graybody radiation must yield a constant temperature across the wavelength range investigated. However, a wavelength-dependence of the emissivity will introduce a distinct wavelength dependence in the temperature versus wavelength plot [146], some of which might bias the average slope on a Wien plot to higher or lower values.

In Fig. 3.4 a comparison between two synthetic data representing an ideal graybody with emissivity $\epsilon=0.415$ and a body at 50 GPa with the wavelength-dependent emissivity of Ref. [144] is reported. A fit to the Planck law of the intensity obtained from the wavelength-dependent emissivity, leads to a temperature overestimation of 0.3% at 3000 K and 0.4% at 6000 K.

The experimental setup adopted on the beamline ID27 at the ESRF is reported in Fig. 3.5.

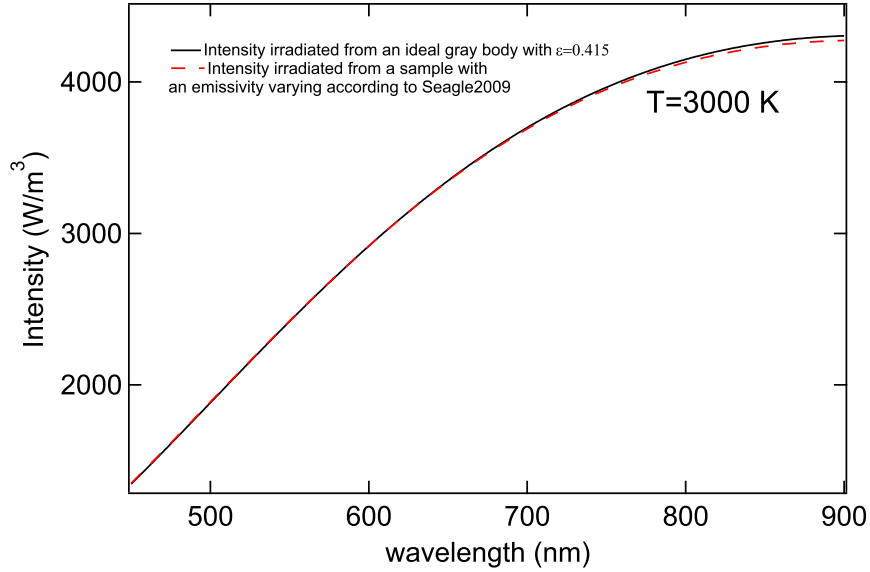


Figure 3.4: Synthetic data representing an ideal graybody with emissivity $\epsilon=0.415$ (black line) and a sample at 50 GPa with the wavelength-dependent emissivity (dashed red line) reported in Ref. [144]. The radiated intensities have been calculated at 3000 K.

Two Continuous-Wave (CW) Nd:YAG lasers ($\lambda = 1064$ nm) are used to heat each side of the sample in the DAC.

The emitted light and the image of the sample are collected using two Schwarzschild reflective objective [62] especially designed to avoid chromatic aberration that can introduce large errors in the temperature measurement [141]. The magnified signal is thus transmitted to a 300 mm Acton Spectrometer equipped with a Pixis 100 CCD camera from Princeton Instruments.

A pinhole of 50 μm diameter is laser-drilled at the entrance of the spectrometer. Considering the magnification of the Schwarzschild objective ($\sim \times 18$), the 50 μm pinhole corresponds to a probed area of 3 μm in diameter on the sample surface which is used to measure the temperature at the center of the hotspot created by the Nd:YAG lasers.

For a correct determination of the temperature, it is necessary to determine the optical system response $S(\lambda)$. This is done by collecting the radiated intensity from a calibrated tungsten lamp at 2500 K ($I_m(\lambda, T_0)$). $S(\lambda)$ then follows:

$$I_m(\lambda, T_0) = \frac{S(\lambda)\epsilon(\lambda, T_0)2\pi hc^2}{\lambda^5} \frac{1}{e^{\frac{hc}{\lambda T_0}} - 1} \quad (3.16)$$

Tungsten has been chosen as a standard material because of its well known

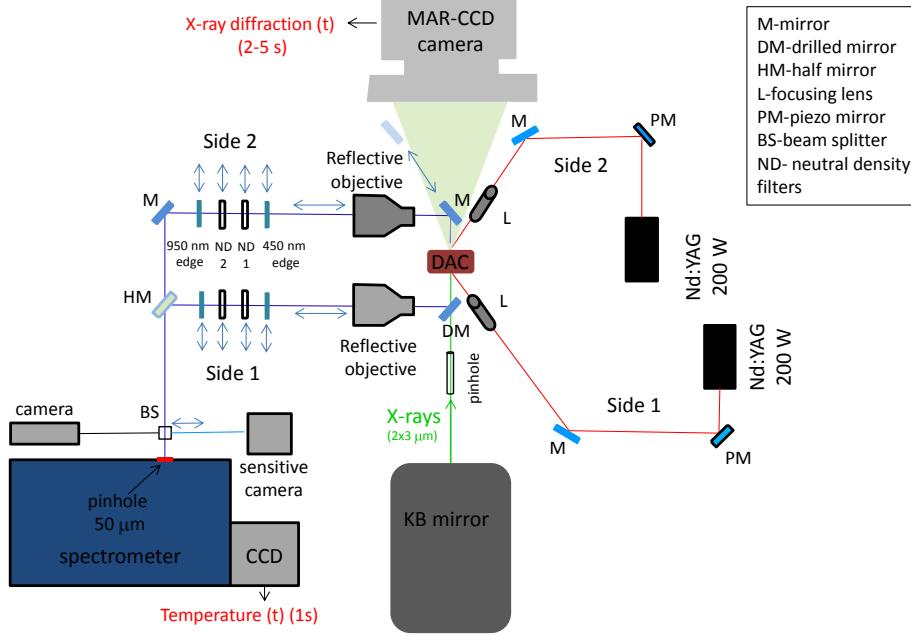


Figure 3.5: Schematic layout of the laser-heating system adopted on ID27 at the ESRF. Red lines indicate the pathway of the Nd:YAG lasers. In green the incident X-ray beam and the X-ray cone of diffraction to the image plate. In blue is the path for the double-sided temperature measurement. Double arrow signs refer to optics mounted on pneumatic stages. The symbols used for mirrors, lenses, etc. are listed in the legend. During the experiment, the mirror between the Schwarzschild and the DAC on side 2 is removed to permit the collection of the diffracted signal on the image plate. The temperature is thus measured only on side 1 during the experiment. The sketch has been modified from Ref. [147]

wavelength-dependent emissivity ($\epsilon(\lambda, T_0)$) [148, 149]. The tungsten lamp is placed at the position normally occupied by the sample and the emitted light is collected through the optical pathway to the spectrometer.

An emission spectrum is recorded in the optical range 450-900 nm and the CCD dark offset is subtracted from each spectrum, then the spectrum is normalized to the system response through $S(\lambda)$. Plank, Wien and two-color methods are used to fit the normalized intensity over the same wavelength range according to the method reported by *Benedetti and Loubeyre* [146]. In this way, it is possible to correlate deviations from the Planck's fit with

deviations from linear Wien function and with variations in the $T_{two-color}$. The temperature uncertainties are estimated from the standard deviation of a Gaussian fit to the $T_{two-color}$ histogram [146], plus a manual check of the sensitivity of the fitted temperature to the wavelength fitting region. Data presenting a difference in the temperature measured by the Plank and the Wien methods larger than 1% and/or presenting deviations from the Wien and the two-color distributions, are considered not reliable and thus discarded.

Figs. 3.6 and 3.7 represent examples of data that verify the graybody approximation and data that have been discarded.

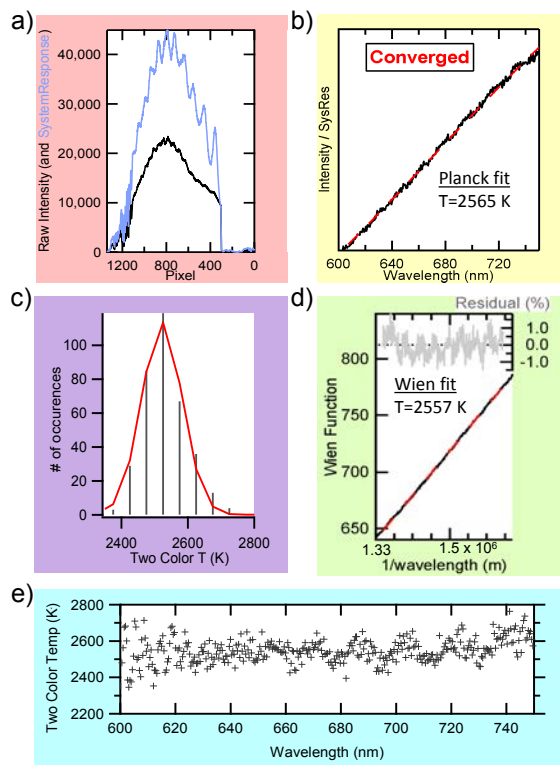


Figure 3.6: Example of reliable temperature measurement. a) Measured raw intensity (black line) and the system response (blue line). b) Planck's distribution normalized to the system response (black line) and the corresponding fit (red dotted line). c) Histogram of the measured $T_{two-color}$ (gray lines) fitted to a gaussian function (red line). d) Wien function of the normalized intensity (black line), fit to the Wien function (red dotted line) and the corresponding residual (gray line). e) Two color temperature reported as a function of wavelength obtained with a wavelength window of 40 nm. The fit have been performed between 600 and 750 nm.

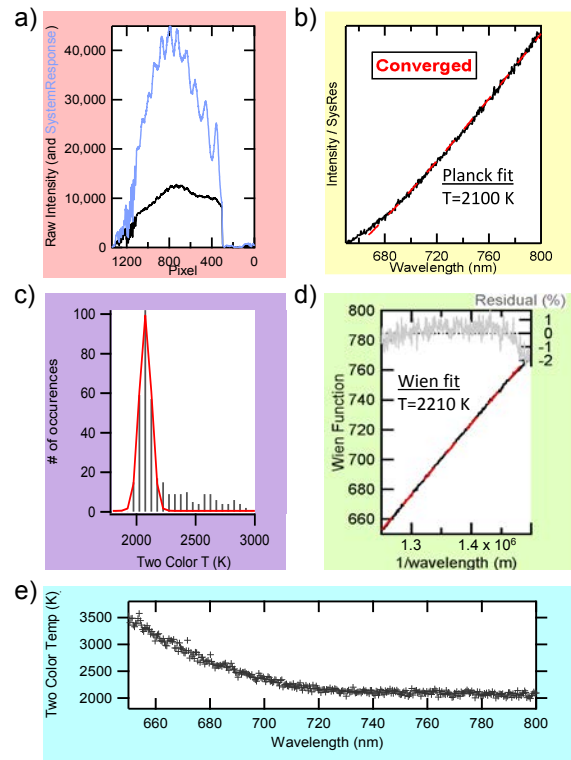


Figure 3.7: Example of a temperature measure that has been discarded. a) Measured raw intensity (black line) and the system response (blue line). b) Planck's distribution normalized to the system response (black line) and the corresponding fit (red dotted line). c) Histogram of the measured $T_{two-color}$ (gray lines) fitted to a gaussian function (red line). d) Wien function of the normalized intensity (black line), fit to the Wien function (red dotted line) and the corresponding residual (gray line). e) Two color temperature reported as a function of wavelength obtained with a wavelength window of 40 nm. In this figure both the residual of the fit to the Wien function and the $T_{two-color}$ present a wavelength dependent trend. The fit have been performed between 650 and 800 nm.

As a further verification of the reliability of the pyrometric measurement, the measured temperatures have been cross-checked with the temperature expected from the thermal expansion of the Fe sample measured by X-ray diffraction (see chapter 4).

Chapter 4

XRD study of the Fe melting curve

In this chapter, the experimental setup and the results obtained on the melting curve of Fe studied in LH-DAC by fast XRD are reported.

4.1 Introduction

In the previous chapters, the techniques associated to LH-DAC experiment have been presented. In what follows, a description of the sample loading procedure and experimental setup adopted to study the melting curve of iron by fast XRD is made. The experimental results are discussed together with the implication in the determination of the Earth's geotherm.

4.2 Sample loading

Generally and particularly for LH-DAC experiment, a good sample preparation is mandatory for the collection of good quality data. In fact, thermal and pressure gradients, together with chemical reactions can bias the P - T measurements in a LH-DAC experiments. These phenomena can be minimized if the sample is loaded in the high pressure chamber of a DAC following certain precautions.

In this work, Fe samples were loaded in a KCl pressure transmitting medium which insulated the Fe from the diamond surface and the rhenium gasket. The KCl (>99.5%, Fluka) has been chosen because in the P - T range investigated has a melting curve higher than the one predicted for iron [150, 33, 28]. In addition, it has a simple XRD pattern with no superimposition with the diffraction peaks of Fe. The KCl was also used as pressure gauge using a recent EOS [132], so that the number of materials involved is minimized to two. The KCl was dried at 570 K in a vacuum oven to remove any presence of water that can react with Fe under high temperature.

The sample must have a regular shape to guarantee the most uniform response of the sample's surface heated by the laser. The thermal insulating layers must be flat in order to help homogeneous heating. In what follows, the procedure adopted for the sample loading at "high" (100-210 GPa) and "low" (50-100 GPa) pressure conditions will be described.

4.2.1 "Low" pressure

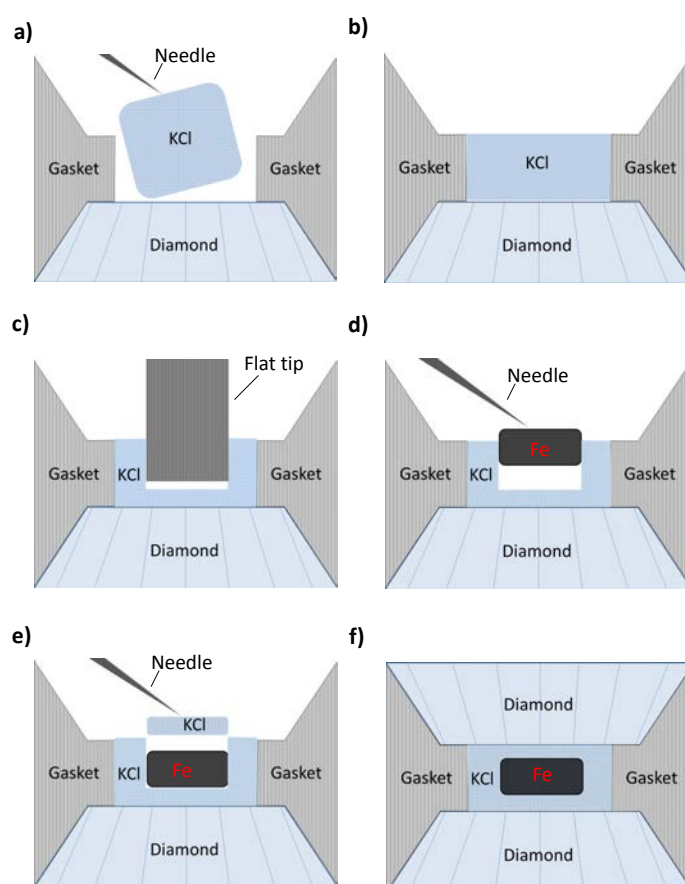


Figure 4.1: Schematic representation of the principle adopted to load the sample in the high pressure chamber of a DAC equipped with diamonds with culets ranging from 300 to 150×300 μm .

In Fig.4.1, a schematic representation of the principle adopted for the sample loading is reported. A dried crystal of KCl, with a diameter similar to the one of the laser-drilled hole of the Re gasket, is placed in the

high pressure chamber of a DAC (Fig.4.1a). The crystal is then compressed between the two anvils to completely fill the hole of the gasket. The KCl leaked from the high pressure chamber must be cleaned up from both the diamond's anvils and from the gasket. This procedure must be repeated until a homogeneous disk of KCl is obtained (Fig.4.1b).

At this point a containment chamber for the sample must be prepared. For this purpose we have used a flat-tip-equipped spark-erosion machine in off mode. In fact, this machine is equipped with an optical system that permits to center the flat tip on the high pressure chamber, preserving the vertical position of the tip with respect to the KCl disk surface (Fig.4.1c). Furthermore, if equipped with a thickness gauge digital indicator, it is possible to obtain information on the depth of the hole drilled in the KCl. During this procedure, the hole have been drilled with a depth of the order of 2/3 of the total thickness of the pre-indented gasket. The KCl leaked at the sides of the hole is removed with a micromanipulator.

Fe powder (>99.9%, Alfa Aesar) grains are pre-shaped into thin (3-7 μm thickness) disk by compression between the two diamonds anvils. The obtained disk is then placed in the containment chamber (Fig.4.1d). The sample is handled in a manner to be perfectly positioned at the base of the containment chamber and the parallelism of the sample with respect to the diamonds is checked by changing the polarization of the microscope's light.



Figure 4.2: Picture of a Fe sample completely embedded in a KCl pressure transmitting. The ruby pressure gauge is also visible in the picture near the gasket-KCl interface (circle on the left).

Then, flat plates of KCl are pre-shaped by compression of the KCl crystals between the two anvils and needle-cut to a diameter slightly larger than the one of the hole in the KCl disk. The KCl plates are positioned to perfectly cover the containment chamber and the KCl-Fe-KCl set (Fig.4.1e) is compressed between the two anvils. By changing the focalization of the mi-

crosscope it is possible to have an idea of the quantity of KCl placed on the Fe on both sides. If the two quantities are different, the KCl at the interface with the gasket is scraped off and a plate of KCl is placed in the way to completely cover the Fe sample. As before, the set is compressed between the anvils and the leaked KCl is cleaned up. This procedure is repeated until the quantity of KCl on both side is similar and no more leaking of KCl is observed. A scheme of the final sample loading is reported in Fig.4.1f while a picture is reported in Fig.4.3.

4.2.2 "High" pressure

In the cases of culet's size ranging from 100×300 to $70 \times 300 \mu\text{m}$ (~ 110 - 210 GPa), the diameter of the high pressure chamber is too small (40 - $30 \mu\text{m}$) to apply the procedure described before.

Two different sample loading procedures have been made. The first kind of loading is schematically represented in Fig. 4.3. In this case, flat plates of KCl (Fe) are pre-shaped by compressing the starting crystals (powder) between the diamonds. The plates are then placed at the center of the anvil on the cylinder side of the cell. This procedure is subsequently repeated for each plates in the order KCl-Fe-KCl.

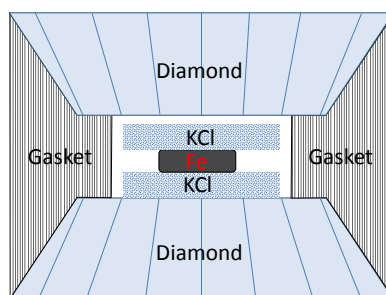


Figure 4.3: Schematic representation of the sample loading adopted at higher pressure for diamond with flat tips.

For diamonds with very small culet ($70 \mu\text{m}$), the volume of the obtained pressure chamber doesn't permit to load big quantity of insulating material. For this reason pits of $3 \mu\text{m}$ thickness have been machined by Focused Ion Beam (FIB) at the center of the diamond's culets (Fig. 4.4). In this way in fact, it is possible to increase the thickness of the pressure chamber without changing the diamond's culet size. After been machined, the diamond have been treated with a mixture of H_2SO_4 and KNO_3 to remove any trace of graphite that can easily react with Fe with the increasing pressure and temperature.

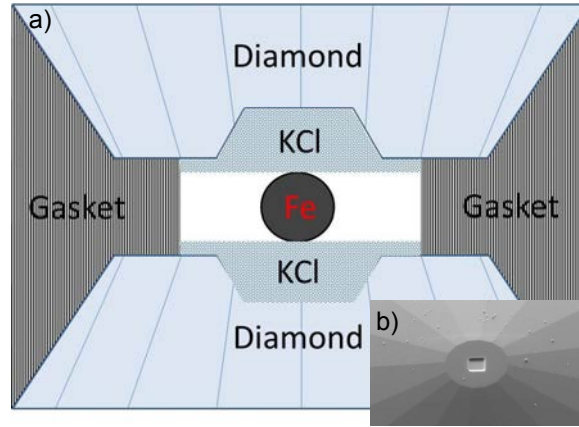


Figure 4.4: a) Schematic representation of the sample loading adopted at higher pressure for diamond with pits. b) Picture of the culet of a diamond with a pit machined with FIB on its center.

In this case, the KCl crystals are pre-shaped into plates and placed at the center of both diamond's culets. A grain of Fe is then placed on the KCl in the way to be centered on the pit. In Fig. 4.4 a schematic representation of the loading in the case of diamonds with pits is reported.

4.3 Experimental setup

The experimental runs have been carried out on the ID27 beamline at the ESRF. The double-sided laser heating system of this beamline is optimized for *in situ* monochromatic X-ray diffraction experiment with LH-DAC and, since its development in 2005 [62], it has permitted to several groups to study the matter under extreme P - T conditions with applications in condensed matter physics and geophysics fields [124, 61, 151, 152, 153].

The laser-heating experimental setup adopted on ID27 has been described in chapter 3 and a schematic layout is represented in Fig. 3.5.

During our experiment, two CW lasers Nd:YAG fiber lasers (IPG photonics) with $\lambda=1064$ nm and providing a maximum total power of 200 W were focused on both the sample surfaces through UV-grade fused silica lenses with a typical focusing distance of 70 mm [147]. The beam spot is in the fundamental transfer mode TEM_{00} or Gaussian profile; the beam has a very high quality with $M^2=1.02$ (for an ideal Gaussian profile $M^2=1$) and the laser output power has a very high stability of ± 0.5 %.

For the runs at lower pressures, the two lasers were defocused in order to increase the hot spot size on the sample to 20 μm of FWHM. At higher pressure the smallest laser-heating spot used was 5 μm of FWHM.

The angular dispersive ($\lambda=0.3738 \text{ \AA}$) XRD patterns were collected on a CCD detector located at a distance of $\sim 200 \text{ mm}$ from the sample.

The intense monochromatic X-ray beam of ID27 is focused using an achromatic multi-layered Kirkpatrick-Baez (KB) double mirror device [86] and cleaned by two pinholes to a $2 \mu\text{m} \times 2.7 \mu\text{m}$ FWHM spot on the sample.

In order to ensure the collection of XRD and radiance data from the same region of the sample, the area used for the pyrometry measurement was aligned on the X-ray beam before each heating ramp. The adopted alignment procedure is as described in Fig. 4.5. The X-ray beam can be visualized with a high sensitivity camera, using the X-ray induced fluorescence of the pressure medium. The image of the pinhole entrance in the spectrometer through the Schwartzschild objective can be seen on the same camera. Then the lasers are aligned with the X-ray and the pinhole.

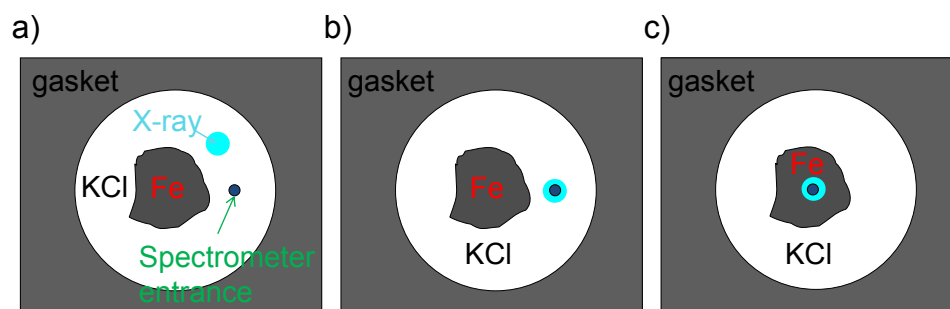


Figure 4.5: Schematic representation of the pinhole-X-ray alignment procedure. a) X-ray fluorescence signal can be observed through the high sensitivity camera. b) The X-ray beam is centered on the spectrograph's pinhole by moving the Schwartzschild beam. c) The cell is then moved to align the sample with the X-ray beam.

The sample was gradually heated up to melting (in best cases) and quenched. The alignment of the X-ray and the pinhole can be lost if the objective is

heated by an unwanted reflection of the YAG laser. To check that this didn't happen, we checked the alignment between the X-ray and the pinhole immediately before and after each heating ramp.

To prevent the probing of skewed or reacted area (melt percolation through the pressure medium, chemical diffusion...), the samples were heated at different position after each heating ramp.

We performed *fast* XRD experiments [61], in which the XRD spectra were collected every 2-5 s, while radiance spectra from the laser-heated surface of the sample were collected every second. The collecting procedure is automated and can be easily controlled during the experiment. The XRD images and the temperature profiles (Planck, Wien and two color) can be followed during a heating ramp.

4.4 Experimental results

During each heating ramp, the temperatures were measured by pyrometry according to the method described in chapter 3. The pressure P was deduced from the P - V - T equation of state of KCl [132] using the molar volume measured by XRD. For that purpose, the temperature in KCl was assumed to be equal to the pyrometry temperature *i.e.* the temperature at the Fe-KCl interface.

Axial temperature gradients were present in the KCl volume scanned by XRD, the KCl in contact with the diamond anvil being cooler than the KCl in contact with the sample. However, a temperature difference of 1000 K leads to a pressure difference of only 2 GPa because of the low thermal pressure factor in the KCl EOS [132].

The temperatures and the pressures measured at each heating ramp are reported in Appendix A and represented in Fig. 4.6.

Temperature uncertainties have been measured, as described in chapter 3, from the pyrometry signal fitting errors [146], plus a manual check of the sensitivity of the fitted temperature to the wavelength fitting region. They range from 3 % to 6 % (100 K to 300 K).

A *time-resolved* analysis of the structural, textural and chemical evolution of the sample and the insulating material with the rise of the laser power has been performed.

4.4.1 Textural evolution of the solid sample

The only iron phases observed during the experiment are the ϵ and γ phases. For each heating ramp, the textural evolution of Fe and KCl have been followed over all the P - T range investigated. The textural evolution of Fe, always shows the same trend. The starting powder signal slowly recrystallizes with increasing temperature. Above a certain pressure-dependent temperature, *fast recrystallization* phenomena appear *i.e.* single crystal spots of

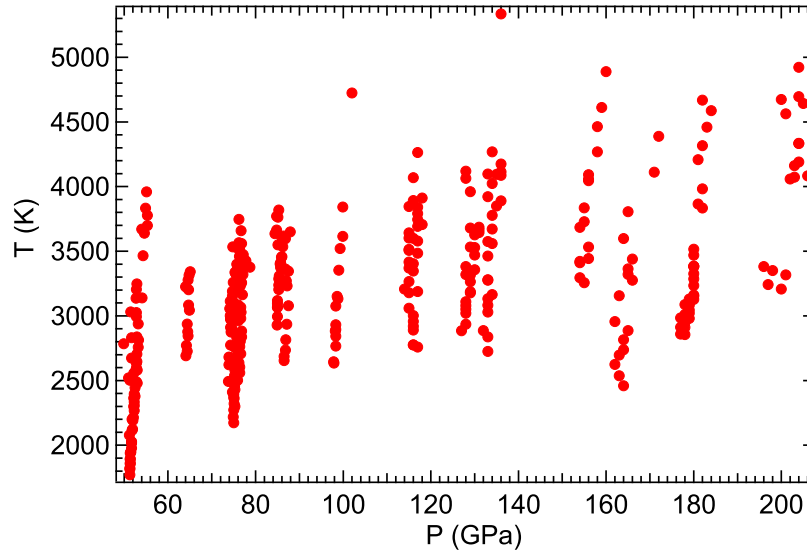


Figure 4.6: P - T domain investigated during the experiments performed on ID27.

Fe (sometimes appearing as broad but well-individualized diffraction spots) disappear and appear in different region on the CCD image plate at each XRD exposure (Fig. 4.7).

This *fast recrystallization* phenomena have been observed in ϵ -Fe and γ -Fe. Concerning the textural evolution of the KCl, it shows a powder signature in almost all the P - T range investigated (see Fig. 4.7). Only for pressure above 178 GPa and temperature above 4500 K a (slow) recrystallization texturing of KCl has been observed.

4.4.2 Detection of melting

Our melting criterion was the apparition on the image plate of the diffuse XRD signal characteristic of liquids. This signal was observed in several heating ramps up to ~ 160 GPa and appears from 400 K to 900 K above the onset of the *fast recrystallization*. In Fig. 4.8 a XRD pattern collected at 76 GPa and presenting the characteristic diffuse ring is reported together with its corresponding integrated signal.

Once detected, the diffuse signal was visible also at higher values of the laser power and, in most of the studied cases, single crystal XRD spots from solid Fe, undergoing *fast recrystallization* phenomena, were still present on the image plate. This is due to the thermal gradient formed within the sample during a heating ramp. In fact, the innermost regions of the sample are

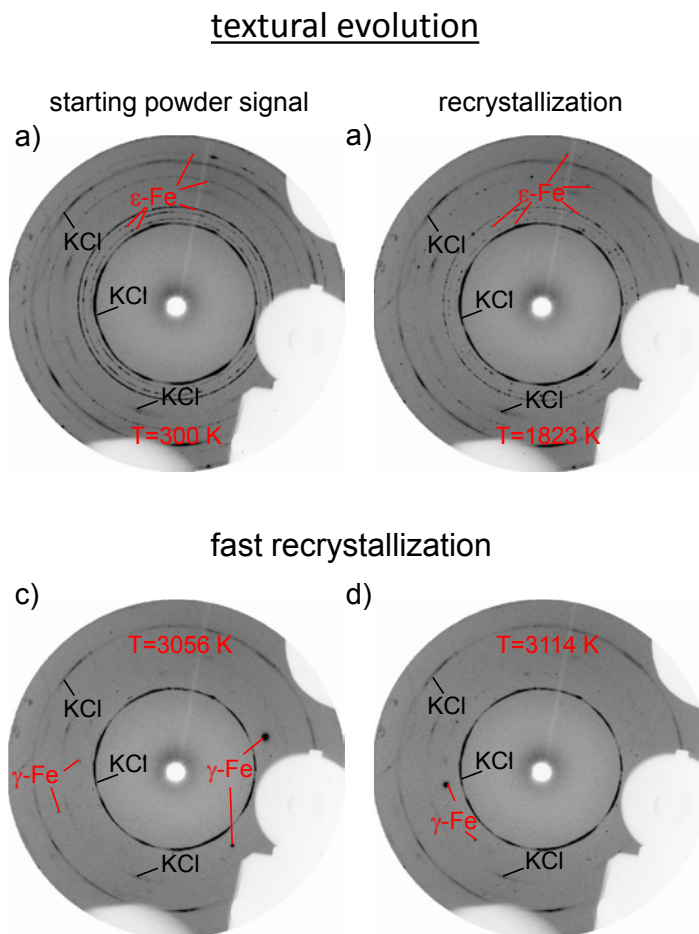


Figure 4.7: Example of the XRD textural evolution observed for an iron sample embedded in KCl at ~ 73 GPa. With the increasing temperature, the starting powder signal from iron (a) start to recrystallize (b). Above a certain temperature, *fast recrystallization* phenomena appear. Figure (c) and (d) represent the XRD signal obtained at two consecutive exposure after the *fast recrystallization* onset. The single crystal spots of iron disappear and appear in different region of the image plate.

at lower temperatures with respect to the sample's surfaces directly heated by the lasers. Thus, the onset of melting is firstly reached at the sample's surfaces, while the rest of the sample remains solid.

This interpretation is also supported by the fact that the intensity of the liquid signal on the XRD pattern increases with the rise of the laser power, indicating that the amount of molten Fe scanned by XRD increases with time (Fig. 4.9).

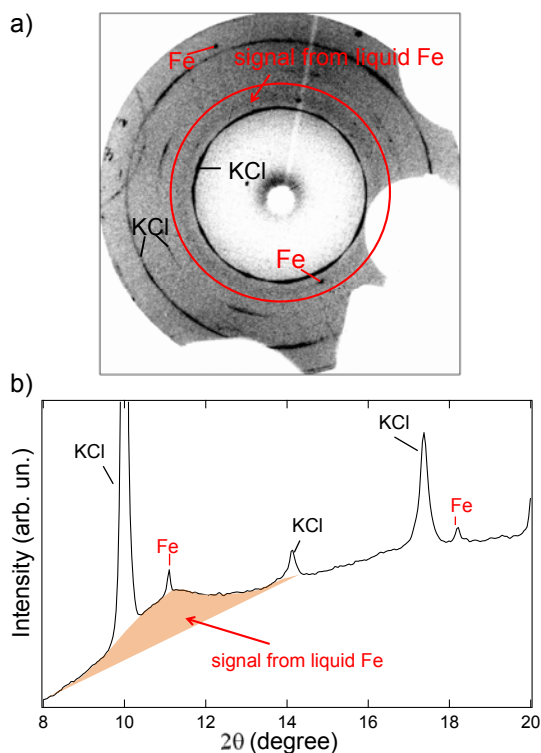


Figure 4.8: a) CCD image plate in which the characteristic XRD diffuse ring from liquid Fe observed at 76 GPa is visible. b) Corresponding integrated signal.

The apparition of a diffuse signal on the image plate provides a bulk signature of melting. However, this signal is weak compared to the signal coming from the solid part of the sample. In order to obtain the most accurate determination of the onset of melting, it is important to remove from the XRD pattern all the contributions that can cover the weak diffuse signal from the liquid Fe. At this purpose, the XRD single crystal spots on the image plate are masked during the integration procedure with Fit2D. The obtained spectra are normalized and compared with each other in order to determine when the first "clear" signal of diffuse appears. The melting temperature was taken as the average between the temperature at which the first "clear" diffuse signal from the liquid was detected and the last temperature at which the signal from a completely solid Fe was observed.

In Fig. 4.9 a comparison between normalized spectra at ~ 76 GPa is reported.

The obtained melting points, have been fitted together with previous low-

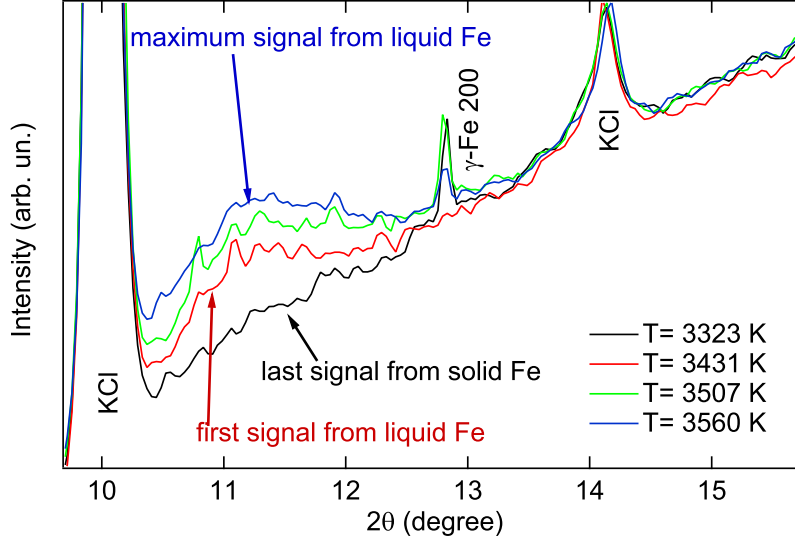


Figure 4.9: Comparison between normalized XRD patterns collected during a heating ramp at ~ 76 GPa.

pressure data [18] to two Simon's equations [6]. The resulting relations are:

$$\frac{P - P_0}{27.39} = \left(\frac{T_m}{T_0} \right)^{2.38} - 1 \quad (4.1)$$

for the γ -liquid coexistence curve and:

$$\frac{P - P_{TP}}{161.2} = \left(\frac{T_m}{T_{TP}} \right)^{1.72} - 1 \quad (4.2)$$

for the ϵ -liquid coexistence curve. $P_0 = 5.2$ GPa and $T_0 = 1991$ K have been taken from Ref. [18], while $P_{TP} = 98.5$ GPa and $T_{TP} = 3712$ K are the measured pressure and temperature of the observed γ - ϵ -liquid triple point. The melting curve of pure iron, can thus be extrapolated at 330 GPa (ICB) according to 4.2 giving $T_m(330\text{GPa}) = 6230 \text{ K} \pm 500 \text{ K}$. The error has been calculated from the maximum error in the pyrometry measurement and the uncertainty in the detection of the melting temperature (200 K).

4.4.3 Chemical reactions

Generally, we didn't observe signature of chemical reactions during a heating ramp. Only in a few cases, the XRD spectra exhibited a partial reaction of Fe with the diamond anvils, as shown by the existence of weak peaks that can be assigned to Fe_3C [154] as shown in Fig. 4.10.

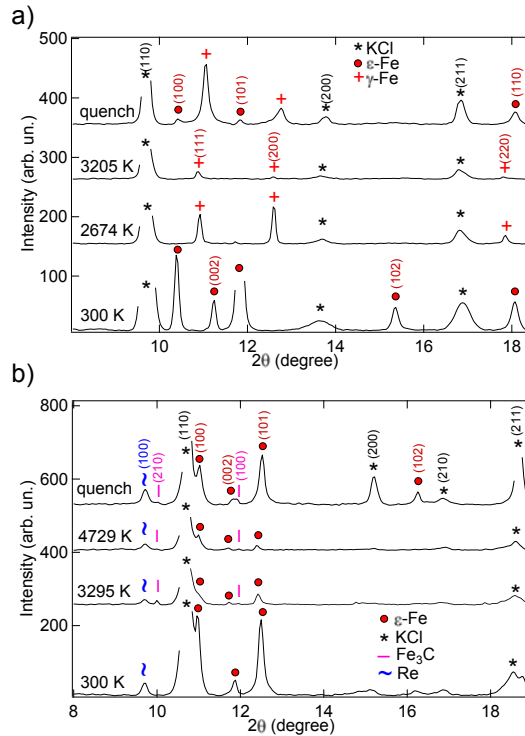


Figure 4.10: XRD spectra of two different sample during an heating ramp. a) Ramp with no chemical reactions at $P \sim 50$ GPa. b) No massive chemical reaction are present in the XRD pattern (weak peaks of Fe₃C) at $P \sim 133$ GPa.

4.4.4 Volumetric thermal expansion

For each XRD pattern, the volume of solid Fe has been calculated from the measured lattice parameter (listed in Appendix A). The XRD data have been treated as powder data at temperature below recrystallization and as single crystal data above recrystallization: in that cases, each (unsaturated) single crystal XRD peak was integrated individually and used to determine the lattice parameters. Two to five peaks have been used and the scatter of the data is attributable to temperature gradient in the scanned zone.

For several measurement, XRD peaks of Fe saturated the detector and an accurate determination of the Fe lattice parameter was impossible. No measurement of the lattice parameter is therefore reported in Appendix A for these cases.

In Fig. 4.11 the molar volume of the observed Fe-phases and the measured pyrometry temperature are plotted as a function of time for different temperature ramps at different pressures. In each graph of Fig. 4.11, the

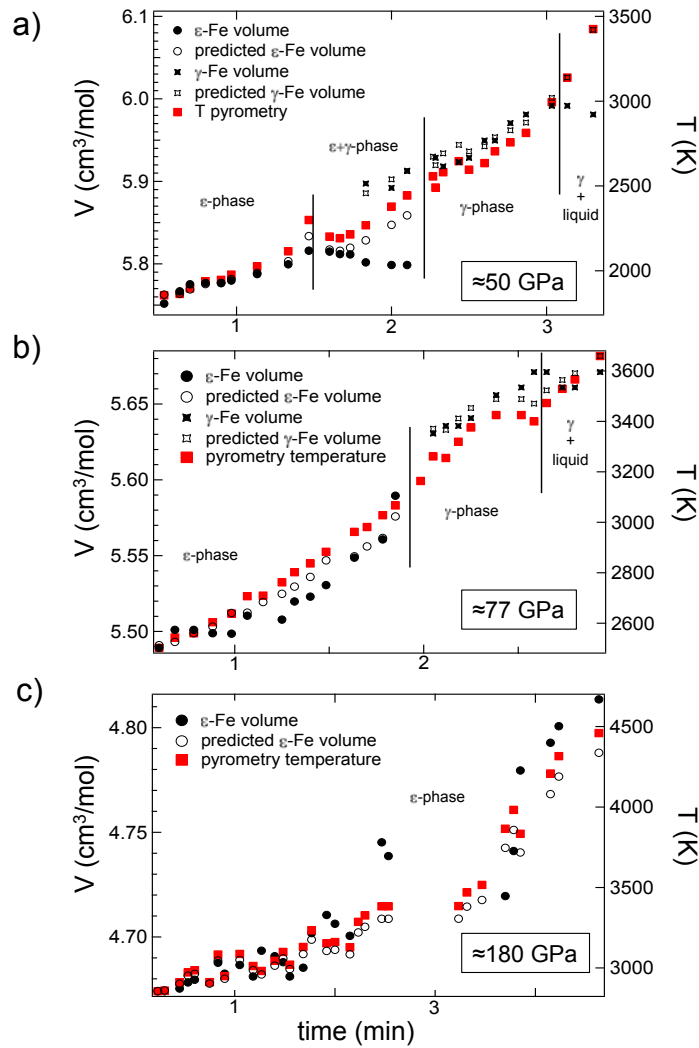


Figure 4.11: Volumetric thermal expansion of the measured phases (black solid symbols), the pyrometry measurement (red solid symbols) and the predicted volumetric thermal expansion (black empty symbols) at different P - T conditions. According to the observed structural phases, (a) and (b) are divided in different regions. A plateau in the temporal distribution of the volumes of the γ phase of Fe is observed in both (a) and (b) above the onset of melting. A plateau is also observed in the distribution of the ϵ -Fe volumes above the onset of the $\epsilon-\gamma$ phase transition (a). c) Example of a heating ramp performed at 180 GPa in which no phase transition was detected but the volumetric thermal expansion is in agreement with the pyrometry measurement.

predicted volumetric thermal expansion of ϵ -Fe [134] and γ -Fe [139] calculated at constant pressure, is compared to the measured one, providing a further check of the pyrometry measurement.

Above the onset of a phase transition (solid-solid or solid-liquid), the XRD signal from both the mother (before the transition) and the daughter (after the transition) phases are observed on the image plate. In this coexistence region, the XRD measured volume of the mother phase presents a plateau with time (Fig. 4.11). Such a plateau is a direct consequence of the thermal gradient formed within the sample. In fact, with the increasing temperature, the volume of a particular phase expands up to a threshold value after which the phase transition takes place. Due to the presence of the thermal gradients, this threshold value is firstly reached at the surfaces of the sample and then, successively, in the deepest layers of the sample.

The XRD signal from the mother phase will be visible on the image plate until the last inner-most layer of the sample has reached the threshold temperature of the phase transition.

As a consequence, a comparison between the temperature measured at the onset of the phase transition and the one measured when the last signal from the mother phase is detected, can provide information on the magnitude of the thermal gradients.

During our experiments, we have observed that these temperature gradients can be of the order of 400 K.

4.4.5 Comparison with previous LH-DAC results

The quality of the melting temperature measured in a LH-DAC experiment, depends on the reliability of the criteria used to distinguish whether the sample has molten or not. So far, several methods have been applied to determine the onset of melting. To date, the first criteria adopted and widely used for identifying the onset of melting concern the visual observation of fluid flow on the sample surface [155, 37, 28] and textural consideration on the recovered sample [37].

Laser speckle technique [156, 143] is used for direct observation of motion on the sample surface at high temperature. In this technique, the thermal radiation emitted by the heated surface is cut off by a narrow bandpass interference filter and the sample surface is lighted by a visible laser [157]. However, this method doesn't provide any information on the physical state of the sample during a heating ramp. Other phenomena such as chemical reactions, solid-solid phase transition or melting of the insulating material can lead to a motion on the sample surface and thus bias the measurement of the melting temperature.

The observation of quenched liquid balls on the laser-heated region of the recovered sample, provides a concrete proof that the sample has molten dur-

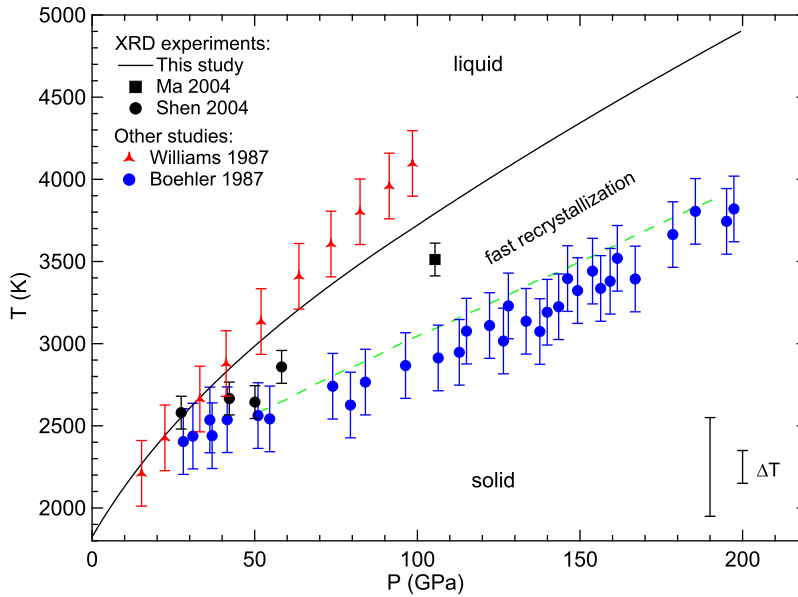


Figure 4.12: Comparison between the melting curve obtained in this study (black line) and melting points obtained in previous study using different melting diagnostic: diffuse ring on the XRD pattern (black symbols) [31, 29], textural consideration on the recovered sample (red symbols) [30, 37] and direct observation of movement on the sample surface (blue symbol) [28]. The *fast recrystallization* threshold observed in this study is also reported with a green dashed line. Our temperature uncertainties of 100 K and 300 K are reported in the graph.

ing the heating ramp [30, 37, 152]. However, due to the *ex situ* nature of this diagnostic, several samples must be used only to investigate a small regions on the P - T domain. In addition, the temperature measurements are conducted on fully molten sample spots [37], therefore the temperature is not measured at the onset of the solid-liquid phase transition. An over-estimation of the melting temperature measured with this method is thus possible.

The use of *fast* XRD measurement in LH-DAC, offers an alternative to the melting diagnostics discussed above. It provides a bulk signature of melting, characterized by the apparition of a diffuse ring on the XRD pattern and permits to obtain direct information on the physical state of the sample during a heating ramp. The textural, structural and chemical evolution of the sample and the insulating material are easily followed with the rise of the laser power. In addition, thanks to the *time-resolved* nature of the experiment, the collected information (volumetric thermal expansion, phase transition,

pyrometry temperature, etc..) can be correlated to each other for a better interpretation of the obtained results and to cross-check the accuracy of the measurement e.g. in our experiments, the simultaneous observation of a diffuse ring on the CCD and a plateau in the temporal distribution of the volumes, provides an unambiguous signature of melting.

In Fig. 4.12, melting points of iron obtained in previous LH-DAC experiments are compared to the melting curve measured in this study.

Our results agree with the ones obtained in the experiment of *Shen et al.* [29] and *Ma et al.* [31] in which a similar melting diagnostic was used.

An agreement, within the experimental uncertainties, is also observed between our melting points and the ones obtained by *Williams et al.* [30, 37] using textural consideration on the recovered sample as melting criterium.

Comparing our measured melting points with the ones obtained by direct observation of movements on the sample surface with the speckle method [28], they results up to 1000 K higher. This difference cannot be attributed to the adopted temperature measurement technique, because they were similar, neither pressure calibration issues can explain such a difference. However, it is interesting to note that the melting curve measured in Ref. [28] agrees with the onset of *fast recrystallization* observed in this study (Fig. 4.12) and in another recent work [158] in which it was used as a melting diagnostic. It is thus possible that the *fast recrystallization* phenomena, correspond to movement on the sample surface that have been detected in Ref. [28] and attributed to the onset of melting. However, during our experiment we have observed the apparition of the diffuse ring 400 to 900 K above the onset of *fast recrystallization*. Thus, iron melting temperatures determined by the observation of movements on the sample surface are underestimated.

Geotherm

From the results obtained in our experiment, we can calculate a geotherm in the Earth's outer core.

The calculation can be made under the assumption that the liquid part of the core is in a state of convection, which implies that the distribution of the temperature in the core follows an adiabat.

According to the definition of the Grüneisen parameter for adiabatic compression [6]:

$$\gamma = \left(\frac{\partial \ln T}{\partial \ln \rho} \right)_S \quad (4.3)$$

where γ is the Grüneisen parameter, T the temperature, ρ the density and S the entropy. If we consider a constant Grüneisen parameter of 1.51 within the Earth's outer core as derived in the *ab initio* model of Ref. [162], this will yield a constant T/ρ^γ . Thus, the temperature profile in the outer core

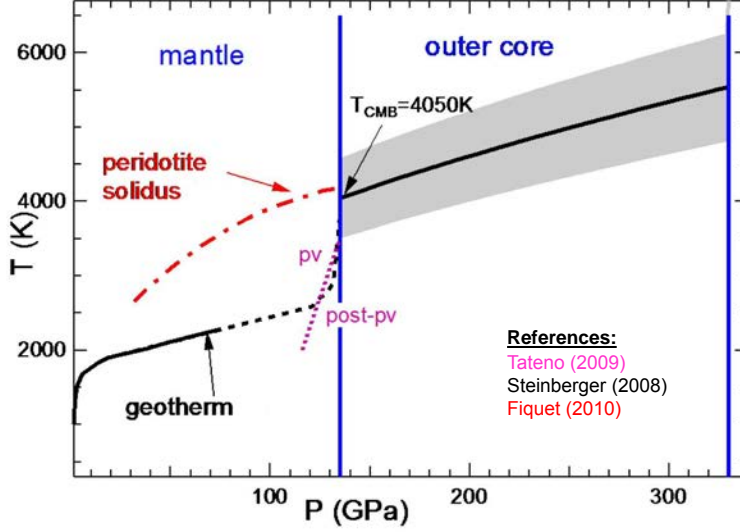


Figure 4.13: Earth's temperature profile (geotherm) inside the outer core calculated from our measurement, with the estimated geotherm in the mantle [159] peridotite solidus [160] and perovskite to post-perovskite phase boundary for MgSiO_3 [161].

can be calculated as:

$$T = T_{ICB} \left(\frac{\rho}{\rho_{ICB}} \right)^\gamma \quad (4.4)$$

In this expression, ρ is taken from the PREM model [1], while the temperature at the ICB (T_{ICB} , 330 GPa) is extrapolated from the melting temperature at the ICB of pure iron obtained in this study ($T_m(330 \text{ GPa}) = 6230 \text{ K} \pm 500 \text{ K}$) at which a depression due to the presence of light elements (S, Si and O) has been subtracted. This depression is estimated to be of the order of $700 \text{ K} \pm 100 \text{ K}$ from *ab initio* calculations for composition agreeing with seismic properties of the inner and outer core [16, 163].

Thus, according to Eq. 4.4, the Core-Mantle Boundary (CMB, 135 GPa) temperature on the core side is $4050 \text{ K} \pm 500 \text{ K}$. This value is close to the solidus of peridotite (4150 K at 135 GPa) found in Ref. [160], which means that a partial melting of the mantle is possible close to the CMB with the current geotherm.

In Fig. 4.13, the geotherm is represented together with the geotherm obtained for the mantle in Ref. [159], the perovskite - post perovskite phase boundary [161] and the peridotite solidus [160].

According to Ref. [161], the post perovskite phase is stable at 135 GPa below $3520 \text{ K} \pm 70 \text{ K}$ for MgSiO_3 . Within the experimental uncertainties,

a double crossing scenario, in which the lower mantle after the perovskite - post perovskite phase transition at 120 GPa [39], returns in a perovskite phase at 135 GPa, is possible with a T_{CMB} of 4050 K.

Comparing our obtained geotherm in the core to the one obtained for the mantle in Ref. [159], a Thermal Boundary Layer (TBL) of the order of ~ 1400 K is present at the base of the mantle. The heat flow at the CMB can be calculated from [164]:

$$Q = k \left(\frac{\partial T}{\partial r} \right)_S S_{CMB} \quad (4.5)$$

In which k is the thermal conductivity in the TBL, $(\partial T/\partial r)_S$ is the adiabatic temperature variation in the TBL and S_{CMB} is the surface area at the CMB and can be calculated considering the radius of the core ($R_{CMB} = 3486$ km [164]). Thus, considering a 200 km thick TBL with a thermal conductivity of 10 W/m/K [15], we obtain a heat flow at the CMB of the order of ~ 10 TW.

4.5 Article

In the following pages, a paper published on *Science* in April 2013 and entitled "Melting of Iron at the Earth's Inner Core Boundary Based on Fast X-ray Diffraction" is attached.

6. M. R. Showalter, *Science* **282**, 1099 (1998).
 7. R. S. French *et al.*, *Icarus* **219**, 181 (2012).
 8. E. Grün, H. A. Zook, H. Fechtig, R. H. Giese, *Icarus* **62**, 244 (1985).
 9. S. Bouley *et al.*, *Icarus* **218**, 115 (2012).
 10. L. S. Chambers, J. N. Cuzzi, E. Asphaug, J. Colwell, S. Sugita, *Icarus* **194**, 623 (2008).
 11. Some "flashes" of unknown provenance were reportedly seen in Voyager data (23, 24), but these have not been confirmed nor generally accepted.
 12. C. C. Porco *et al.*, *Space Sci. Rev.* **115**, 363 (2004).
 13. Details of our observations and data reduction are given in sections 1 and 2 (respectively) of the supplementary materials text.
 14. A. Van Helden, in *Saturn*, T. Gehrels, M. S. Matthews, Eds. (Univ. of Arizona Press, Tucson, AZ, 1984), pp. 23–43.
 15. M. S. Tiscareno, in *Planets, Stars, and Stellar Systems, Volume 3: Solar and Stellar Planetary Systems*, T. D. Oswalt, L. French, P. Kalas, Eds. (Springer, Dordrecht, Netherlands, in press); <http://arxiv.org/abs/1112.3305>.
 16. P. D. Nicholson, M. M. Hedman, *Icarus* **206**, 410 (2010).
 17. M. M. Hedman, J. A. Burns, M. W. Evans, M. S. Tiscareno, C. C. Porco, *Science* **332**, 708 (2011).
 18. All measured brightnesses are relative to the ring background.
 19. J. E. Colwell *et al.*, in *Saturn from Cassini-Huygens*, M. Dougherty, L. Esposito, S. M. Krimigis, Eds. (Springer, Dordrecht, Netherlands, 2009), pp. 375–412.
 20. A. R. Poppe, M. Horányi, *Geophys. Res. Lett.* **39**, 15104 (2012).
 21. J. N. Cuzzi, R. H. Durisen, *Icarus* **84**, 467 (1990).
 22. E. Grün, G. W. Garneau, R. J. Terrile, T. V. Johnson, G. E. Morfill, *Adv. Space Res.* **4**, 143 (1984).
 23. A. F. Cook, T. C. Duxbury, *J. Geophys. Res.* **86**, 8815 (1981).
 24. A. F. Cook, R. Barrey, G. E. Hunt, *Bull. Am. Astron. Soc.* **15**, 814 (1983).

Acknowledgments: We thank M. Showalter for helpful discussions and for the use of Mie scattering code. We thank the Cassini project and the Cassini Imaging Team for making these observations possible. M.S.T. acknowledges funding from the NASA Cassini Data Analysis program (NNX08AQ72G and NNX10AG67G) and the Cassini project. C.D.M. acknowledges funding from the Science and Technology Facilities Council (grant ST/F007566/1).

Supplementary Materials
www.sciencemag.org/cgi/content/full/340/6131/460/DC1
 Supplementary Text
 Figs. S1 to S11
 Tables S1 to S7
 References (25–38)

3 December 2012; accepted 18 March 2013
 10.1126/science.1233524

Melting of Iron at Earth's Inner Core Boundary Based on Fast X-ray Diffraction

S. Anzellini,^{1*} A. Dewaele,¹ M. Mezouar,² P. Loubeyre,¹ G. Morard³

Earth's core is structured in a solid inner core, mainly composed of iron, and a liquid outer core. The temperature at the inner core boundary is expected to be close to the melting point of iron at 330 gigapascal (GPa). Despite intensive experimental and theoretical efforts, there is little consensus on the melting behavior of iron at these extreme pressures and temperatures. We present static laser-heated diamond anvil cell experiments up to 200 GPa using synchrotron-based fast x-ray diffraction as a primary melting diagnostic. When extrapolating to higher pressures, we conclude that the melting temperature of iron at the inner core boundary is 6230 ± 500 kelvin. This estimation favors a high heat flux at the core-mantle boundary with a possible partial melting of the mantle.

Earth's inner core grows by solidification from the surrounding outer core, which is composed of molten iron (Fe) alloyed

with ~10 weight percent light elements (1). Seismological data reveal important physical properties of the core, such as density (and, hence,

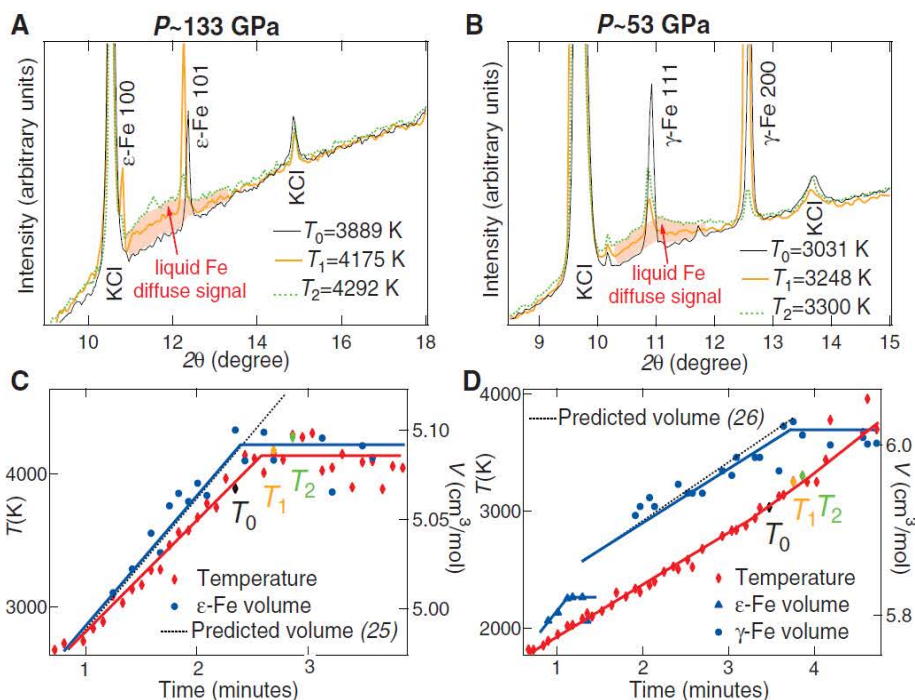
pressure) and elasticity; however, they cannot directly reveal the corresponding temperature. Temperature in the core places important constraints on parameters like heat flux to the mantle, power for the geodynamo, and cooling rate, all of which are fundamental to Earth's heat budget and dynamics (2).

The temperature at the inner core boundary (ICB) is bracketed between the melting temperature of pure Fe at 330 GPa and the liquidus temperature of the outer core iron-rich alloy (3) [expected to be depressed by ~700 K (4)]. Neither dynamic (5–7) and static (8–11) compression measurements nor thermodynamic modeling (12–15) have resulted in a consensus on ICB melt-

¹Commissariat à l'Énergie Atomique, Direction des Applications Militaires Île de France 91297 Arpajon Cedex, France. ²European Synchrotron Radiation Facility, BP 220, F-38043 Grenoble Cedex, France. ³Institut de Minéralogie et de Physique des Milieux Condensés UMR CNRS 7590, Université Pierre et Marie Curie, 75005 Paris, France.

*Corresponding author. E-mail: simone.anzellini@cea.fr

Fig. 1. XRD patterns as a function of temperature, pressure, and time. (A and B) XRD patterns of a ~3- μ m-thick (~7- μ m-thick) sample during a heating series at $P \approx 133$ GPa and 53 GPa, respectively, recorded at different temperatures. γ -Fe, ϵ -Fe, and KCl pressure medium diffraction peaks are labeled. Liquid Fe is evidenced by a diffuse ring at $2\theta = 10^\circ$ to 13.5° . (C and D) Pyrometry temperature, measured and predicted (25, 26). Fe volume as a function of time for the thin (C) and thick (D) samples. The laser's power is linear with time. Data are in table S1.



ing temperature, in part because these approaches suffer from intrinsic uncertainties. Dynamic measurements have long been considered the most promising way to determine the ICB temperature because shocked Fe melts around 230 GPa, yet the temperature determination (spanning from

5100 to 6350 K) and the possibility of superheating in shock compression (16) are major uncertainties. Using laser heating in static diamond anvil cell (DAC) experiments to produce reliable melting data above 100 GPa is also difficult because of uncertainties in the pyrometric

temperature measurements (17), the criterion used to identify the melting (18), and the possible temperature-induced chemical reactions (18, 19). In fact, estimation of Fe melting temperature at ICB pressure based on static compression data spans the range 4850 (8) to 7600 K (10). Finally, the tremendous advances in computational capacity have enabled quantum-mechanics calculations of the melting behavior, but each method has underlying approximations or assumptions. For instance, melting temperatures from 6370 (14) to 7050 K (12) have been obtained with the same melting criterion—the coexistence of a liquid and solid phase in a molecular dynamics run—but a different description of interatomic forces within density functional theory. Going beyond density functional theory with a quantum Monte Carlo simulation, melting was obtained at 6900 K (15) at 330 GPa.

Here, we report the laser-heated DAC determination of the Fe melting curve from 50 to 200 GPa, using a μm -spatial and second-time-resolved approach that has recently been applied to the determination of the Ta melting line (18). Fast x-ray diffraction (XRD) is used as the primary technique for structural determination. This approach presents several advantages: (i) The structural evolution of Fe can be followed during heating; (ii) the measured volume expansion of solid Fe provides an independent control of temperature measurements; (iii) chemical reactions, if any, can be observed within the few percentage detection limits; and (iv) most importantly, an unambiguous bulk signature of melting—i.e., the appearance of a diffuse ring—is recorded (9, 20). This technique offers an alternative to the melting diagnostics used in the past in the laser-heated DAC: motion of the sample surface (8, 10), microscopic observation of the recovered samples (10), and plateaus/drops on the temperature ramps (8, 21).

The XRD spectra obtained during heating provide direct information about the physical state of the laser-heated sample that can be correlated with additional information such as temperature T versus time (Fig. 1). From this, we determined that ϵ -Fe (hexagonal close packed) and γ -Fe (face-centered cubic) are the only structures observed in the investigated pressure-temperature range. This confirms earlier findings of a large stability field for ϵ -Fe (19, 22) and extends in temperature this domain up to the melting line at 200 GPa—e.g., under the conditions where a transformation to a body-centered cubic phase had been suggested using shock wave measurements (23) or ab initio calculations (24). XRD patterns also show, in a few cases, a partial reaction of Fe with the diamond anvil, as shown by the appearance of weak peaks that can be assigned to Fe_3C (20). Therefore, each heating series was performed on a fresh, unheated zone of the sample. Furthermore, we measured and compared the volume of solid Fe with the expected volume based on the pyrometry temperature and the equation of state of ϵ -Fe (25) or γ -Fe

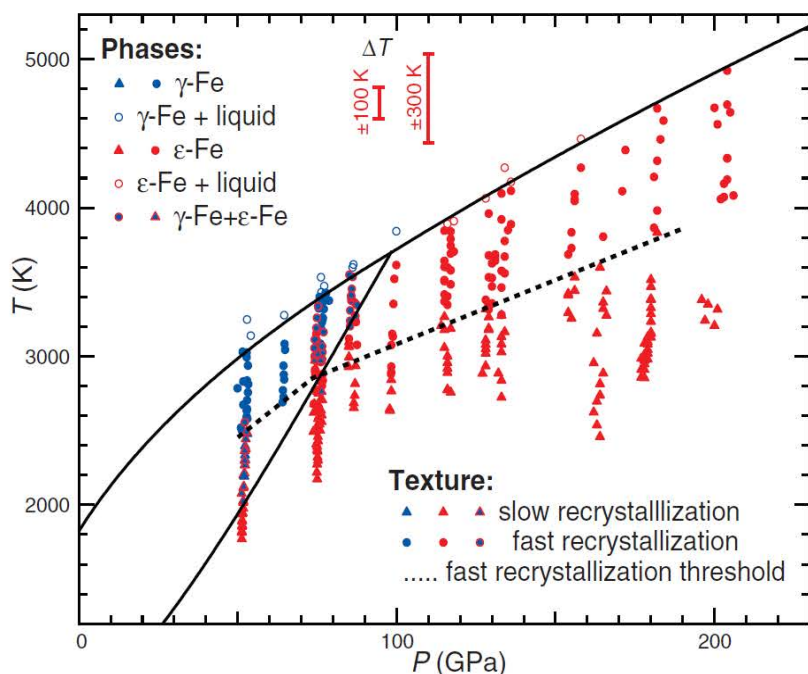


Fig. 2. Pressure (P_{KCl})–temperature conditions at which XRD patterns have been collected. Different symbols correspond to different Fe phases and textures. The continuous black lines correspond to Eqs. 1, 2, and 3. Data are in table S1.

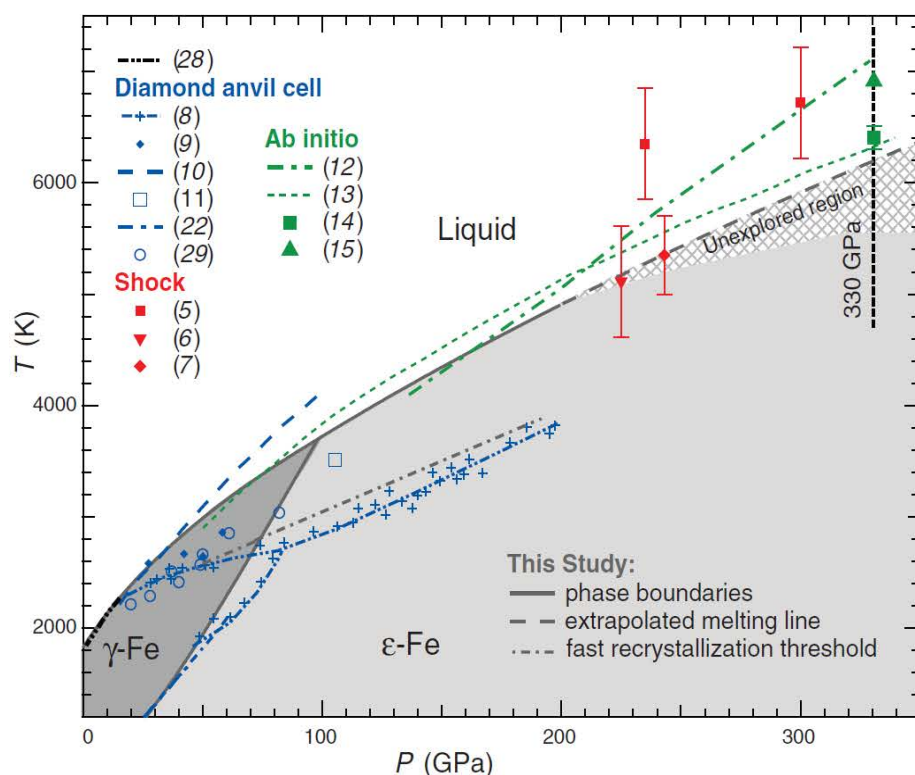


Fig. 3. Phase stability domains for Fe obtained in the literature and in this study. The stability field for ϵ -Fe is based on the current study data and data from (19).

(26), assuming that the pressure remained constant. In cases where an inconsistency was detected, the ramp data was discarded. Finally, XRD images yield information on the sample texture: The starting fine powder transformed into large single crystals upon heating. Above a certain temperature, single-crystal spots appeared and disappeared at each XRD exposure, which we refer to as “fast recrystallization.”

Changes in T versus time curves, such as plateaus or sudden drops, are often considered as a melting signature (8, 21). This is interpreted as a loss of thermal insulation in the sample assembly due to melting (27). We observed such features, but not systematically. In Fig. 1, the temporal evolutions of the temperature and the ϵ -Fe volume of a $\approx 3\text{-}\mu\text{m}$ thickness sample are parallel: a linear increase, then a marked plateau. A diffuse scattering signal of the liquid appears in the XRD signal at the beginning of this plateau; however, ϵ -Fe single crystal XRD spots indicate that the sample is not completely molten. For a thicker ($\approx 7\text{ }\mu\text{m}$) sample, the observations seem less correlated. After the expected γ -Fe to ϵ -Fe phase transition (22), the ϵ -Fe volume has a similar behavior as for the thin sample: It plateaus during melting, evidenced by the diffuse XRD signal. However, the pyrometry temperature continues to increase. With the rise of temperature, the intensity of the liquid signals increases, indicating that the amount of molten Fe scanned by XRD increases. Our interpretation is that the solid Fe is surrounded by layer of liquid Fe a few μm thick, whose surface is heated and analyzed by pyrometry. We observe that this layer sustains a sharp temperature gradient, its surface being up to 400 K warmer than solid Fe. The XRD measurement of the plateau of thermal expansion and the simultaneous observation of the diffuse diffraction peak of the liquid provide here an unambiguous signature of melting.

The melting temperature T_m is estimated as the average between, respectively, the highest (lowest) temperatures at which only solid (solid + liquid) Fe is observed (Fig. 2). The temperature of fast recrystallization is substantially (400 to 900 K) lower than the melting temperature. Two Simon equations are used to fit the melting points together with existing low-pressure data (28). The ϵ -Fe to γ -Fe phase boundary is estimated using the current data and literature data (22, 28). The γ - ϵ -liquid triple point is at a pressure of 98.5 GPa (P_{TP}) and 3712 K (T_{TP}). The following formulations are obtained [T in K, P in GPa, $T_0 = 1991$ K, and $P_0 = 5.2$ GPa (28)].

$$T = 575 + 18.7P + 0.213P^2 - 0.000817P^3$$

$$(\epsilon - \text{Fe}/\gamma - \text{Fe}) \quad (1)$$

$$(P - P_0)/27.39 = (T_m/T_0)^{2.38} - 1$$

$$(\gamma - \text{Fe}/\text{liquid}) \quad (2)$$

$$(P - P_{\text{TP}})/161.2 = (T_m/T_{\text{TP}})^{1.72} - 1$$

$$(\epsilon - \text{Fe}/\text{liquid}) \quad (3)$$

The present melting curve closely follows the one determined by Alfè *et al.* (13) on the basis

of a Gibbs free-energy minimization (Fig. 3). It goes through the dynamic determinations of melting (6, 7), around 230 GPa. The melting temperatures of Fe obtained with the laser-heated DAC are bracketed by two studies (8, 10), which mainly differ in their melting criteria. The present melting curve is within the error bars of the measurements based on the observation of textural changes on recovered samples up to 100 GPa (10)—a method which is probably not possible above that pressure—and agrees correctly with determinations based on a similar method (9, 11) and a recent indirect measurement (29). The current melting points are up to 1000 K higher than the melting points obtained by the observation of surface motion of a laser-heated sample (8). Neither temperature measurement techniques, which are similar, nor pressure calibration issues can explain such a difference. It is possible that the melting diagnostic used in (8) detects fast recrystallization instead of melting. Indeed, it is interesting to note that the melting line of (8) coincides with the temperature of fast recrystallization, observed in this study and in another recent work (30). In the latter study, it was interpreted as melting evidence. We propose instead that fast recrystallization begins at temperatures below melting and causes the surface motion observed in (8), which had been wrongly attributed to melting.

Eq. 3 extrapolates to $T_m(330\text{ GPa}) = 6230 \pm 500$ K. The error is the sum of the maximum pyrometry error and the uncertainty on the detection of melting temperature (200 K). A temperature profile inside Earth’s core can be estimated using this value, which leads to a temperature at the core-mantle boundary (T_{CMB}) of 4050 ± 500 K (20). This corresponds to a thermal boundary layer of ~ 1400 K at the base of the mantle and, subsequently, a high CMB heat flux (~ 10 TW) (2). Such a value is needed to sustain the geodynamo with recent estimate of the core conductivity (31). At CMB pressure, partial melting of the mantle material has been observed at 4180 ± 150 K (32) and would therefore be possible with strong geodynamical and geochemical implications. At 135 GPa, the post-perovskite phase is stable below 3520 ± 70 K for MgSiO_3 (33); a double-crossing scenario (33) is therefore compatible with the current T_{CMB} , given the error of experimental determinations.

Our experiments result in better agreement between calculations, and dynamic and static DAC approaches, and reduce uncertainty on the expected melting temperature of Fe at the ICB pressure. Because this study spans the 50 to 205 GPa range, we cannot rule out the possibility of a phase transition in Fe at higher P - T (unexplored region in Fig. 3), which could slightly change the extrapolation of the current determination of the Fe melting curve.

References and Notes

1. J. P. Poirier, *Phys. Earth Planet. Inter.* **85**, 319 (1994).
 2. T. Lay, J. Hernlund, B. A. Buffett, *Nat. Geosci.* **1**, 25 (2008).

3. D. Gubbins, B. Sreenivasan, J. Mound, S. Rost, *Nature* **473**, 361 (2011).
 4. D. Alfè, M. J. Gillan, G. D. Price, *Contemp. Phys.* **48**, 63 (2007).
 5. C. S. Yoo, N. C. Holmes, M. Ross, D. J. Webb, C. Pike, *Phys. Rev. Lett.* **70**, 3931 (1993).
 6. J. H. Nguyen, N. C. Holmes, *Nature* **427**, 339 (2004).
 7. J. M. Brown, R. G. McQueen, *J. Geophys. Res.* **91**, (B7), 7485 (1986).
 8. R. Boehler, *Nature* **363**, 534 (1993).
 9. G. Shen, V. B. Prakapenka, M. L. Rivers, S. R. Sutton, *Phys. Rev. Lett.* **92**, 185701 (2004).
 10. Q. Williams, R. Jeanloz, J. Bass, B. Svendsen, T. J. Ahrens, *Science* **236**, 181 (1987).
 11. Y. Z. Ma *et al.*, *Phys. Earth Planet. Inter.* **143-144**, 455 (2004).
 12. A. B. Belonoshko, R. Ahuja, B. Johansson, *Phys. Rev. Lett.* **84**, 3638 (2000).
 13. D. Alfè, G. D. Price, M. J. Gillan, *Phys. Rev. B* **65**, 165118 (2002).
 14. D. Alfè, *Phys. Rev. B* **79**, 060101 (2009).
 15. E. Sola, D. Alfè, *Phys. Rev. Lett.* **103**, 078501 (2009).
 16. S. N. Luo, T. J. Ahrens, *Phys. Earth Planet. Inter.* **143-144**, 369 (2004).
 17. Q. Williams, E. Knittle, R. Jeanloz, *J. Geophys. Res.* **96**, 2171 (1991).
 18. A. Dewaele, M. Mezouar, N. Guignot, P. Loubeyre, *Phys. Rev. Lett.* **104**, 255701 (2010).
 19. S. Tateno, K. Hirose, Y. Ohishi, Y. Tatsumi, *Science* **330**, 359 (2010).
 20. Materials and methods are available as supplementary materials on Science Online.
 21. R. Boehler, N. Vonbargen, A. Chopelas, *J. Geophys. Res.* **95**, 21731 (1990).
 22. T. Komabayashi, Y. Fei, Y. Meng, V. Prakapenka, *Earth Planet. Sci. Lett.* **282**, 252 (2009).
 23. J. M. Brown, *Geophys. Res. Lett.* **28**, 4339 (2001).
 24. A. B. Belonoshko, R. Ahuja, B. Johansson, *Nature* **424**, 1032 (2003).
 25. A. Dewaele *et al.*, *Phys. Rev. Lett.* **97**, 215504 (2006).
 26. T. Komabayashi, Y. Fei, *J. Geophys. Res.* **115**, (B3), B03202 (2010).
 27. Z. M. Geballe, R. Jeanloz, *J. Appl. Phys.* **111**, 123518 (2012).
 28. L. J. Swartzendruber, *Bull. Alloy Phase Diagr.* **3**, 161 (1982).
 29. J. M. Jackson *et al.*, *Earth Planet. Sci. Lett.* **362**, 143 (2013).
 30. R. Boehler, D. Santamaría-Pérez, D. Errandonea, M. Mezouar, *J. Phys. Conf. Ser.* **121**, 022018 (2008).
 31. M. Pozzo, C. Davies, D. Gubbins, D. Alfè, *Nature* **485**, 355 (2012).
 32. G. Fiquet *et al.*, *Science* **329**, 1516 (2010).
 33. S. Tateno, K. Hirose, N. Sata, Y. Ohishi, *Earth Planet. Sci. Lett.* **277**, 130 (2009).

Acknowledgments: The authors acknowledge the European Synchrotron Radiation Facility for provision of beamtime. G.M. is funded by grant ANR-12-BS04-001504. We thank G. Garbarino and A. Salamat for experimental help and C. Sanloup and D. Spaulding for their comments on this manuscript. Data are available in the supplementary materials.

Supporting Materials

www.sciencemag.org/cgi/content/full/340/6131/464/DC1
 Materials and Methods
 Supplementary Text
 Figs. S1 to S4
 Table S1
 References (34–41)

3 December 2012; accepted 25 March 2013
 10.1126/science.1233514

Chapter 5

XAFS study of the Fe phase diagram

In this chapter, the possibility of measuring the phase diagram of iron in LH-DAC with dispersive X-ray absorption diagnostic is studied. We show encouraging results in a preliminary experiment.

5.1 Introduction

In the previous chapter, the criterium adopted to determine the onset of melting was the apparition of the diffuse XRD signal from the liquid. However, due to the long range order sensitivity of XRD, the signal of the liquid is low compared to the signal of a crystalline solid sample. As a consequence, the structural characterization of the liquid phase is difficult to deduce from an XRD signal in a LH-DAC experiment [29, 165].

XAFS technique can be used as a method complementary to XRD to study the phase diagram of iron. Thanks to the short range order sensitivity of XAFS, the configuration of a liquid and a solid sample are measured with the same precision. This peculiarity permit to use the same method to structurally characterize liquid and solid samples [166, 167]. In addition, with this technique solid-solid phase transitions and chemical reactions (if any) can also be monitored [93, 168, 169]. Finally, with an energy dispersive setup [63, 64], a *time resolved* XAFS experiment can be performed with an acquisition time that can reach the millisecond temporal resolution [64].

If a clear signature of the onset of melting, similar to the apparition of the diffuse ring in the case of *fast* XRD, can be found in the XAFS signal during a laser heating experiment, we can use this technique not only to characterize the liquid part of the phase diagram of iron, but also to study its melting curve.

To our knowledge, the only experimental measurement of the melting curve of Fe with an energy dispersive XAFS technique has been performed at 78

GPa by *Boehler et al.* [93].

5.2 Sample preparation

High-quality X-ray absorption spectra can only be obtained if the sample is homogeneous and of equal thickness over a diameter equal or larger than the X-ray beam. In particular, during a XAFS experiment in transmission mode, the signal to noise ratio in the absorption spectra must be optimized: -by decreasing the anvil thickness and thus, the absorption of X-ray photons by the diamonds at the selected energy edge (7.11 keV for the K edge of Fe) [71]. For that purpose, two DACs with *Almax-Boehler* anvils design with a thickness of the order of 1.5 mm have been used for this test.

-by optimizing the sample thickness t to obtain an edge jump $\Delta\mu t \sim 1$ [99]. In this expression $\Delta\mu$ is the difference between the linear absorption coefficient of the selected element before and after the edge. In the case of iron, the ideal absorption signal is obtained for sample with a thickness of the order of 4 μm .

A list with the adopted diamond's culet size, indentation thickness and diameter of the gasket's holes are reported in Table 5.1. We have adopted

culet size (μm)	indentation thickness (μm)	Φ (μm)	sample thickness (μm)
300	31	125	4
150 \times 300	23	67	3

Table 5.1: Values of the Re gasket parameters according to the culet size of the adopted diamonds. Φ : diameter of the laser-drilled hole.

the sample loading procedure used for the XRD experiment at moderate pressure (chapter 4) with KCl as pressure transmitting medium and Re foil of 250 μm initial thickness as gasket material.

5.3 Experimental setup

X-ray absorption spectra at the Fe K-edge (7.11 keV) were measured at the energy-dispersive X-ray absorption beamline ID24 at the ESRF [64]. A schematic representation of the beamline is reported in Fig. 2.18. In this beamline, the polychromatic X-ray beam from an undulator source is reflected by a pair of mirror in a Kirkpatrick-Baez geometry (VFM₁ and HFM in the figure). The beam is then reflected by the elliptically bended silicon crystal in the [111] orientation, that creates angular-energy correlation of the photons. The beam is focused horizontally on the sample by the

polychromator crystal and vertically by a silicon mirror mounted in downstream of the polychromator with a grazing incident geometry (VFM₂). The resulting X-ray beam size on the sample is approximately $4 \times 4 \mu\text{m}^2$ FWHM.

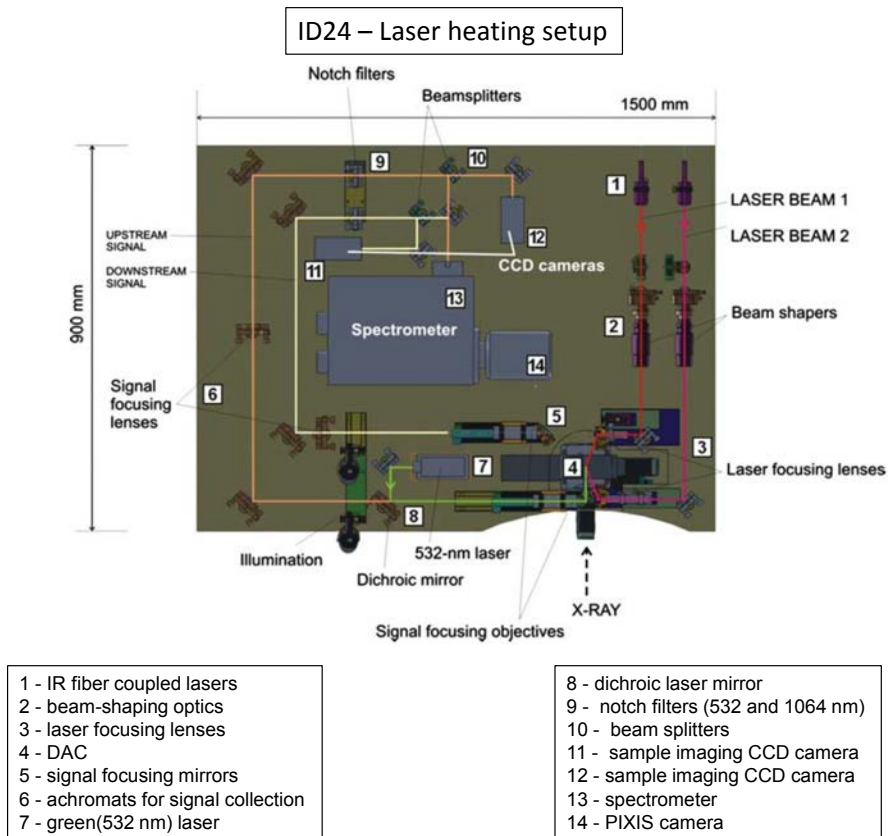


Figure 5.1: Scheme of the laser-heating experimental setup adopted on the beamline ID24. The different components are listed in the legend and indexed with numbers. The scheme has been taken from Ref. [170].

The transmitted signal is analyzed on a linear position sensitive detector (*Labiche et al., 2007*) [171] mounted at approximately two meters from the sample. Pixel to energy calibration is performed using a standard reference (α -Fe) foil.

The double-sided laser heating setup is based on the optical scheme proposed by *Boehler et al.* [93] with aberration-free objectives and is represented in Fig. 5.1. Two independent infrared ($\lambda = 1064 \text{ nm}$) lasers are used to heat the sample up. The focusing point of the two lasers is $\sim 40 \mu\text{m}$ in diameter, about ten times bigger than the X-ray spot. An imaging system with

x16 magnification is used to visualize the sample and to collect the emitted radiation of the hot spot on the sample. The radiated signal is collected through a pinhole to a spectrograph and analyzed in the optical spectrometer ($F=300$ mm, 150 lines/mm grating) equipped with the back-illuminated "Pixis" CCD camera in the spectral range between 450 and 900 nm by pyrometry (chapter 3).

The pressure is measured with a ruby pressure gauge before and after each heating ramp.

The acquisition time for the XAFS spectra, imposed by the diamonds absorption, is about 2 seconds. Acquisition time for T measurement is temperature dependent and varies from few seconds at low T down to 20 milliseconds for high temperatures. When the spectrum is still saturated at this exposure, a neutral density optical filter is used to reduce the signal intensity.

The alignment of the x-ray beam with the two lasers and the spectrograph's pinhole is performed as described in chapter 4 (Fig. 4.5) i.e. the X-ray fluorescence signal of KCl is collected through a high sensitivity camera and aligned with the pinhole at the entrance of the spectrometer by moving the objective. The sample is then centered on the X-ray beam and the two lasers are aligned with the pinhole. This alignment is checked before and after each heating ramp.

5.4 Experimental results

We have performed three heating ramps between 23 and 63 GPa. Before each ramp, the samples are pre-compressed at ambient temperature to the target pressure. The powers of the two lasers are then increased. Radiance data from both the sample surfaces are collected and the corresponding Planck intensities are visualized through a software. The obtained Planck distributions are fitted online to obtain the two temperatures. Once reached the desired temperature on both the sides of the cell, XAFS and radiance data are collected in trigger mode.

Before and after each heating ramp, a hyperspectral μ -XANES mapping [172] of the sample is performed to choose the best region to move on. During the mapping, the sample is scanned horizontally and vertically in the focal plane of the X-ray beam. At each step a Fe K-edge XANES is recorded on a different pixel and normalized. Thus, from the analysis of the edge-jump obtained at each pixel, we can get information on the quantity of iron present in a particular region of the sample. In Fig. 5.2 the μ -XANES edge-jump mapping of a sample at 40 GPa before and after a heating ramp are reported.

The results obtained during this preliminary test are reported in Table 5.2. The reported temperatures are rounded values of the average between

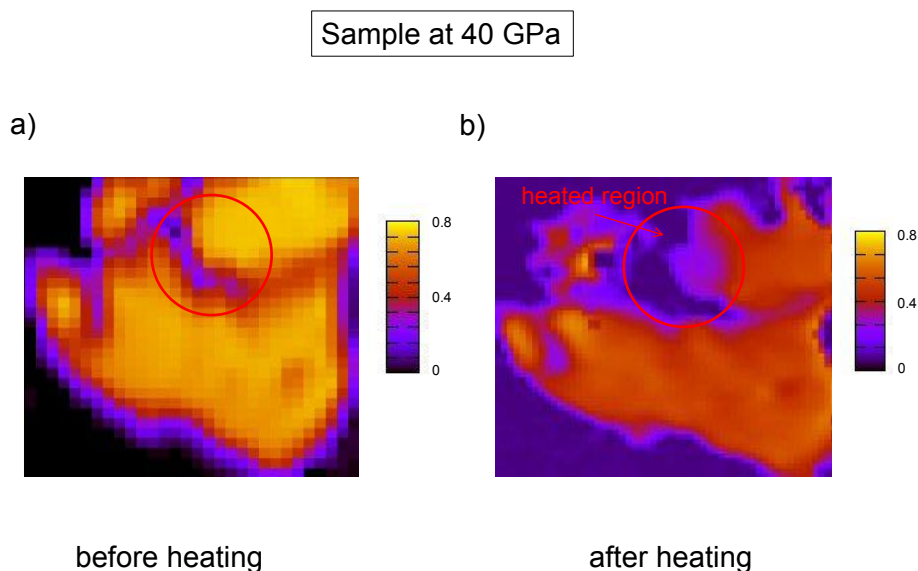


Figure 5.2: Pre-normalized XANES edge-jump maps collected in the DAC at 40 GPa: (a) before laser heating and (b) after laser heating. The red circle indicates the region heated by the laser. The different colors in the figures, indicate different values of the edge jumps of the XANES spectra recorded at each pixel.

the temperatures measured on both the sample surfaces. In a commissioning performed before our test, the beamline scientists of ID24 detected a problem in the alignment of the collecting optics for the radiance data. The temperature reported in Table 5.2 are indicative values with an uncertainty of ~ 300 K.

Fig. 5.3 shows some of the K-edge X-ray absorption spectra of iron obtained during the heating ramps at 40 GPa and 63 GPa.

A part from the presence of two glitches at 7140 eV and 7229 eV due to a problem on the polychromator, we have obtained good quality spectra that do not present any evidence of chemical reactions (Fig. 5.3).

The evolution of the XAFS spectra can be easily followed during the heating ramp. In particular, in Fig 5.3 we can observe a damping of the oscillations in the EXAFS region (above 1750 eV) with increasing temperature, as expected for the increasing thermal disorder.

In Fig. 5.3, a variation of the relative intensities of the double oscillations

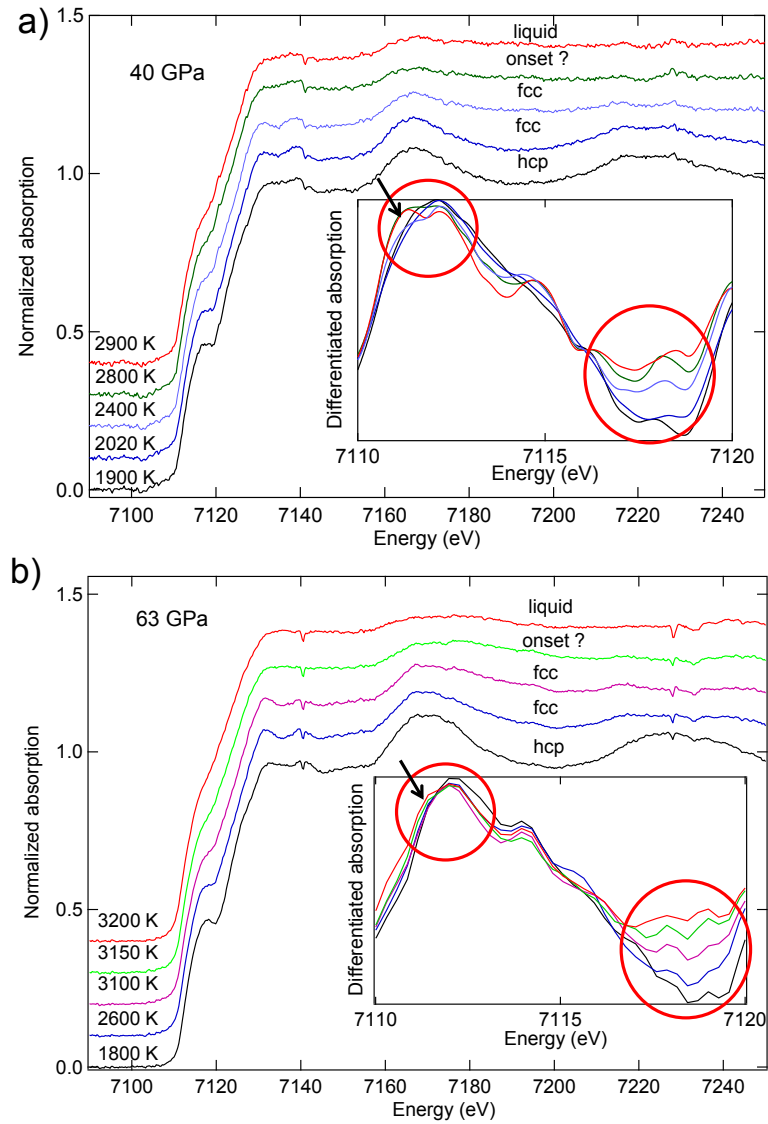


Figure 5.3: X-ray absorption spectra obtained during the heating ramps at 40 GPa (a) and 63 GPa (b). The insets report the differentiated signal of the pre-edge region of the represented spectra.

in the energy range between 7130 eV and 7140 eV is observed. According to the simulated spectra in Fig. 2.19, we can interpret this variation as the $\epsilon - \gamma$ solid-solid phase transition of iron.

Variation in the shape of the pre-peak at 7119 eV are also observed with increasing temperature. In particular, we can see a gradual smoothing of

Table 5.2: List of the results obtained during the preliminary XAFS experiment.

Name	P (GPa)	T (K)	phase	Name	P (GPa)	T (K)	phase
CL1-6	23	1800	γ	D63-11	63	1950	ϵ
CL1-7	23	1800	γ	D63-12	63	2000	ϵ
CL1-8	23	1960	γ	D63-13	63	2100	ϵ
CL1-9	23	2000	γ	D63-14	63	2200	ϵ
CL1-10	23	2060	γ	D63-15	63	2300	γ
CL1-11	23	2100	γ	D63-16	63	2500	γ
CL1-12	23	2300	γ	D63-17	63	2600	γ
CL1-13	23	2400	liquid	D63-18	63	2700	γ
CL1-14	23	2700	liquid	D63-19	63	2800	γ
D40-4	40	1900	ϵ	D63-20	63	2900	γ
D40-5	40	1970	ϵ	D63-21	63	3000	γ
D40-6	40	2020	γ	D63-22	63	3100	γ
D40-7	40	2160	γ	D63-23	63	3100	γ
D40-8	40	2300	γ	D63-24	63	3150	liquid
D40-9	40	2400	γ	D63-25	63	3150	liquid
D40-10	40	2800	liquid	D63-26	63	3200	liquid
D40-11	40	2900	liquid	D63-27	63	3400	liquid
D63-9	63	1800	ϵ	D63-28	63	3500	liquid
D63-10	63	1860	ϵ				

the minimum at 7120 eV after the pre-peak. Above a certain temperature ($T=2800$ K at 40 GPa and $T=3150$ K at 63 GPa), we can observe at 7120 eV an inversion of the slope of the absorption signal and a simultaneous disappearance of the double oscillation between 7130 eV and 7140 eV. In Ref. [93] the same structural evolution of the XAFS spectra has been observed and has been interpreted as the occurrence of the solid-liquid phase transition.

Following the interpretation for the solid-liquid phase transition used in Ref. [93], we can differentiate the XAFS signal in the edge region between 7105 eV and 7130 eV to better characterize the slope change at 7120 eV and try to find a clear signature for the onset of melting.

In the inset of Fig. 5.3 the differentiated signal of the represented XAFS spectra are reported. In the figure, two red circles are used to evidence the observed evolutions of the signal. The smoothing of the pre-peak in the absorption spectra, corresponds to an increase in the intensities between 7116

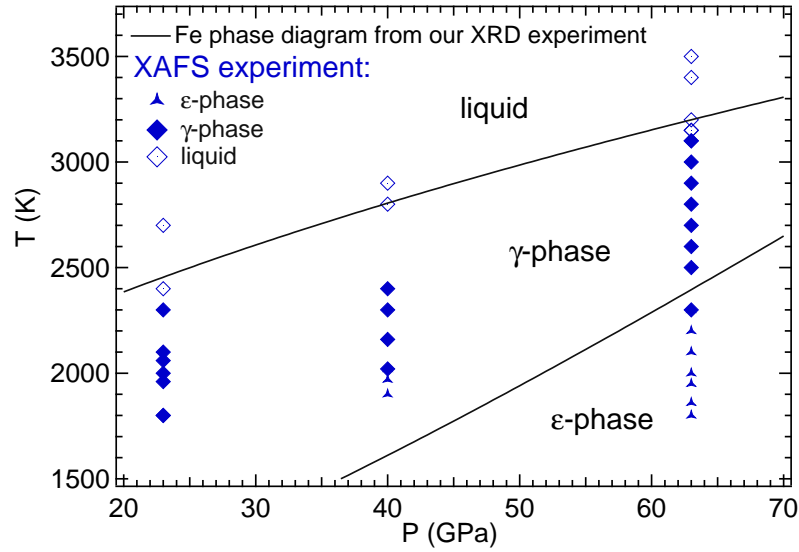


Figure 5.4: Pressure(ruby)-temperature conditions at which the XAFS spectra (blue symbols) have been collected. The different symbols correspond to the different Fe-phases observed. The phase diagram of iron (black continuous lines) obtained from the XRD experiment [173] is also reported.

eV and 7120 eV in the differentiated signal.

Considering the energy region around 7112 eV, we can see the formation of a second peak (indicated by arrows in the figure) in the differentiated signals. The formation of this second peak is observed for signals corresponding to the XAFS spectra in which the double oscillations disappear.

In Fig. 5.4 the iron phase diagram obtained in this study, considering the apparition of the second peak in the differentiated signal as the onset of melting, is compared with the iron phase diagram obtained with *fast* XRD. The agreement between the results obtained with the two different techniques is encouraging. However, the future experiments must be performed in optimized experimental conditions to check the validity of the adopted method.

5.5 Conclusion

The phenomenological analysis performed in this preliminary test in the 20-63 GPa pressure range, gives encouraging results.

The adopted sample loading procedure has permitted to obtain good quality data. The evolution of the XAFS spectra can be easily followed during the heating ramp and provides information on the structural changes undergone

by the sample.

During the test, we have observed the same structural evolution of the XAFS spectra as the one observed in Ref. [93]. The ϵ - γ phase transition has been interpreted with a change in the relative intensities of the double oscillations in the energy range between 7130 eV and 7140 eV, while the simultaneous disappearing of this double oscillation and the inversion in the slope of the signal at 7120 eV, has been interpreted as the apparition of the solid-liquid phase transition. To better constraint the pre-peak evolution with increasing temperature, the XAFS spectra have been differentiated in the edge region between 7105 eV and 7130 eV. The analysis of the obtained signal has shown the apparition of a second peak at energy lower than 7112 eV and an increasing in the intensities of the signal in the energy range between 7116 eV ad 7120 eV.

A comparison with the phase diagram obtained by *fast* XRD, shows an agreement between the results obtained with these two techniques. However, future experiments must be performed in optimized experimental conditions, in order to validate the method.

In the near future, theoretical simulations will be performed to accurately characterize the features obtained on the XANES regions of the spectra. A development of this study foresees the extension of the experimental condition to a larger P - T domain of the iron phase diagram and an extension of the recorded XAFS energy interval to allow the EXAFS characterization of the collected signal.

A proposed experiment has been accepted at the ESRF and will be performed in April 2014.

Chapter 6

Conclusion

The phase diagram of iron, the main constituent of the Earth's core, is of primary geophysical importance. The main results expected from the mineral physics community are the following: (i) the determination of the stable solid phase of iron under the conditions of the Earth's inner core ($P=330$ - 360 GPa, T 6000 K); (ii) the determination of the melting points of iron at the inner core boundary pressure, 330 GPa.

The aim of this PhD was the resolution of the discrepancies found in the characterization of the phase diagram of iron under high pressure and high temperature with static and dynamic experiments. In particular, the melting curve measured in static laser-heated diamond anvil cell (LH-DAC) experiments, is significantly lower than the melting points obtained along the Hugoniot curve in shock compression experiments.

During this work, we have investigated the phase diagram of iron in LH-DAC using synchrotron-based fast X-ray diffraction (XRD) to detect phase changes up to ~ 205 GPa and 5000 K. This technique, based on the second-scale *time-resolved* experimental set-up developed on the beamline ID27 at the ESRF, has already led to the resolution of the static/dynamic discrepancy on the study of the melting curve of Ta under high pressure [61]. X-ray diffraction provides a bulk signature of melting, characterized by the apparition of a diffuse ring on the diffraction pattern and allows obtaining direct information of the physical state of the sample. Thanks to the *time-resolved* nature of this technique, the structural, textural and chemical evolution of the sample can be followed during the heating ramps and the obtained information can be correlated to each other for a better interpretation of the results and to cross-check the accuracy of the measurement.

The reliability of the temperatures measured by pyrometry, have been cross-checked by comparing the volumetric thermal expansion of Fe measured by XRD to the theoretical one obtained in the same temperature conditions.

During this work, new sample loading procedures have been worked out and have permitted to prevent chemical reactions, heat the sample up even at

very high pressure (~ 205 GPa) and observe the apparition of the diffuse ring on the diffracted signal up to ~ 160 GPa.

In the P - T domain investigated, the ϵ and γ solid phases of iron have been observed. However, because this study spans the 50 GPa to 205 GPa range, we cannot rule out the possibility of a solid-solid phase transition of iron at higher P - T conditions.

The melting temperatures obtained in our experiment, agrees with calculations and dynamic experiments and reduce the uncertainties on the expected melting temperature of iron at the ICB pressure.

The discrepancies with previous static measurement of the melting curve of iron, has been correlated with the *fast recrystallization* phenomenon, which is a dynamic recrystallization of the solid sample, at a sub-second time scale, under laser heating. In fact, the melting curve obtained in [28] using the direct observation of movements on the sample surface as melting diagnostic, coincides with the *fast recrystallization* threshold observed in this study. It is thus possible that *fast recrystallization* induces movements on the sample surface that have been erroneously attributed to melting. Further investigation are needed to better understand these *fast recrystallization* processes.

Finally, we have studied the possibility of measuring the phase diagram of iron in LH-DAC with a dispersive X-ray Absorption Fine Structure (XAFS) diagnostic. The interest of this technique, lies in the short range order sensitivity of XAFS which allows detecting the local order in solid and liquid sample with the same precision. Dispersive XAFS, which can also be performed at the sub-second time scale, can thus be used as a method complementary to XRD in the study of the phase diagram of iron. In particular, if a signature of the onset of melting can be found in the XAFS signal, this diagnostic can be used to characterize the liquid part of the phase diagram and investigate the melting curve of iron.

The preliminary tests performed between 23 GPa and 63 GPa in LH-DAC, shows encouraging results.

Solid-solid and solid-liquid phase transitions, which influence the XAFS oscillations, can be monitored with increasing temperature. The phase diagram of iron obtained in this preliminary test agrees with the one obtained by *fast* X-ray diffraction.

In the near future, a dispersive XAFS experiment will be performed to validate the obtained results and to extend the P - T region on the phase diagram of iron characterized with this technique. An accurate analysis of the EXAFS region will be performed to characterize the local structure of the laser-heated sample. Theoretical simulations will be performed to correctly characterize the features obtained in the XANES region.

Appendix A

Table 6.1: Summary of observations made by X-ray diffraction (XRD) at different P-T. KCl, γ -Fe and ϵ -Fe lattice parameters measured by XRD are listed. The temperature has been measured by pyrometry, with error bars of 3% to 6%. The pressures P_{KCl} and P_{Fe} have been calculated using KCl and Fe equations of state [134, 139, 156]. The symbol (F) means that fast recrystallization was observed.

Name	P_{KCl} (GPa)	a_{KCl} (\AA)	T (K)	phase	a_{hcp} (\AA)	c_{hcp} (\AA)	a_{fcc} (\AA)	P_{Fe} (GPa)
X6R2-145	73.8	3.037	2493	ϵ	2.356	3.800		76.3
X6R2-146	73.9	3.038	2622	ϵ	2.351	3.799		79.5
X6R2-147	74.1	3.037	2679	ϵ	2.350	3.805		79.8
X6R2-149	73.9	3.038	2681(F)	ϵ	2.358	3.810		76.3
X6R2-150	74.3	3.038	2774(F)	ϵ				
X6R2-154	74.4	3.037	2875(F)	ϵ				
X6R2-151	74.5	3.038	2880(F)	ϵ				
X6R2-152	74.5	3.038	2894(F)	ϵ	2.357	3.809		79.0
X6R2-153	74.3	3.038	2911(F)	ϵ	2.357	3.810		79.0
X6R2-156	74.7	3.039	2966(F)	ϵ	2.364	3.805		77.7
X6R2-155	74.6	3.037	2984(F)	ϵ				
X6R2-161	74.2	3.038	3001(F)	$\epsilon+\gamma$				
X6R2-157	74.8	3.039	3040(F)	$\epsilon+\gamma$	2.364	3.805		78.5
X6R2-158	74.3	3.038	2979(F)	$\epsilon+\gamma$	2.366	3.810		76.6
X6R2-159	74.4	3.039	3007(F)	$\epsilon+\gamma$	2.360	3.805		79.5
X6R2-162	74.7	3.039	3191(F)	$\epsilon+\gamma$				

Name	P_{KCl} (GPa)	a_{KCl} (Å)	T (K)	phase	a_{hcp} (Å)	c_{hcp} (Å)	a_{fcc} (Å)	P_{Fe} (GPa)
X6R2-163	74.1	3.039	3056(F)	$\epsilon+\gamma$				
X6R2-164	74.7	3.041	3114(F)	$\epsilon+\gamma$				
X6R2-165	74.2	3.039	3113(F)	$\epsilon+\gamma$	2.362	3.822		78.1
X6R2-166	74.9	3.041	3259(F)	$\epsilon+\gamma$	2.361	3.822		80.0
X6R2-167	74.7	3.039	3153(F)	$\epsilon+\gamma$	2.364	3.828		77.2
X6R2-172	75.3	3.039	3337(F)	γ			3.346	78.8
X6R2-175	75.7	3.038	3352(F)	γ			3.350	79.8
X6R2-177	76.9	3.037	3368(F)	γ			3.351	79.6
X6R2-180	75.5	3.033	3323(F)	γ			3.354	78.1
X6R2-181	76.7	3.037	3431(F)	γ +liquid				
X6R2-182	76.4	3.034	3507(F)	γ +liquid			3.352	80.2
X6R2-183	76.3	3.036	3460(F)	γ +liquid			3.353	79.7
X6R2-184	76.8	3.035	3560(F)	γ +liquid			3.354	80.3
X6R4-276	86.5	2.995	2654	ϵ	2.342	3.786		84.8
X6R4-277	86.5	2.995	2687	ϵ	2.342	3.787		85.0
X6R4-278	86.8	2.994	2736	ϵ	2.343	3.787		85.1
X6R4-279	86.9	2.995	2816	ϵ	2.343	3.799		84.5
X6R4-280	87.1	2.995	2936	ϵ	2.345	3.797		85.2
X6R4-281	87.5	2.994	3078(F)	ϵ	2.348	3.803		84.9
X6R4-282	87.2	2.996	3232(F)	ϵ	2.348	3.790		88.1
X6R4-283	86.9	2.998	3272(F)	$\epsilon+\gamma$	2.350	3.801		86.5
X6R4-284	87.0	2.997	3270(F)	$\epsilon+\gamma$	2.348	3.810		86.2
X6R4-285	86.8	2.999	3362(F)	$\epsilon+\gamma$	2.354	3.811		84.8
X6R4-286	87.5	2.996	3346(F)	$\epsilon+\gamma$	2.352	3.780		89.0
X6R4-287	85.7	3.002	3374(F)	$\epsilon+\gamma$	2.352	3.812		85.6
X6R4-290	85.9	3.002	3454(F)	$\epsilon+\gamma$	2.342	3.785	3.329	93.4
X6R4-291	86.1	3.003	3598(F)	γ +liquid				
X6R4-296	87.9	2.997	3650(F)	γ +liquid			3.328	91.3
X6R4-297	86.8	3.001	3597(F)	γ +liquid			3.328	90.8
X6R4-298	86.0	3.002	3458(F)	γ +liquid			3.331	88.3
X6R6-336	85.0	3.002	2995	ϵ	2.343	3.797		86.6
X6R6-337	84.9	3.002	2929	ϵ	2.343	3.794		86.3
X6R6-338	85.0	3.002	3065	ϵ	2.346	3.794		86.6
X6R6-339	85.0	3.002	3068	ϵ	2.345	3.795		86.9
X6R6-340	85.0	3.003	3097	ϵ	2.348	3.800		85.4
X6R6-341	85.0	3.003	3119(F)	ϵ	2.348	3.802		85.5
X6R6-342	85.3	3.003	3286(F)	ϵ				
X6R6-343	85.4	3.003	3309(F)	$\epsilon+\gamma$	2.348	3.790		88.9
X6R6-344	85.3	3.003	3239(F)	$\epsilon+\gamma$	2.348	3.795		87.6
X6R6-345	85.3	3.002	3203(F)	$\epsilon+\gamma$	2.349	3.805		85.6
X6R6-346	85.8	3.002	3395(F)	$\epsilon+\gamma$		3.813		
X6R6-347	85.6	3.003	3402(F)	$\epsilon+\gamma$	2.352	3.797		87.6
X6R6-348	86.2	3.002	3535(F)	$\epsilon+\gamma$	2.350	3.805		88.9
X6R6-349	85.7	3.003	3411(F)	$\epsilon+\gamma$	2.352	3.805		86.8
X6R6-352	85.1	3.004	3549(F)	$\epsilon+\gamma$	2.353	3.812	3.328	87.1
X6R6-355	86.4	3.006	3618(F)	γ +liquid	2.353	3.812	3.330	87.9

Name	P_{KCl} (GPa)	a_{KCl} (Å)	T (K)	phase	a_{hcp} (Å)	c_{hcp} (Å)	a_{fcc} (Å)	P_{Fe} (GPa)
X6R6-356	84.8	3.008	3771(F)	γ +liquid			3.329	92.0
X6R6-357	85.1	3.007	3763(F)	γ +liquid			3.330	91.3
X6R6-358	84.4	3.009	3635(F)	γ +liquid			3.325	92.4
X6R6-359	84.8	3.007	3664(F)	γ +liquid			3.326	92.3
X6R6-360	85.3	3.007	3818(F)	γ +liquid			3.329	92.3
X6R1m-1	51.3	3.127	1771	ϵ	2.390	3.861		52.0
X6R1m-2	51.3	3.128	1823	ϵ	2.390	3.856		52.9
X6R1m-3	51.4	3.128	1855	ϵ	2.390	3.861		52.7
X6R1m-4	51.4	3.128	1863	ϵ	2.390	3.871		51.9
X6R1m-5	51.4	3.128	1896	ϵ	2.393	3.867		51.7
X6R1m-6	51.4	3.129	1938	ϵ	2.393	3.868		52.0
X6R1m-7	51.5	3.129	1946	ϵ	2.393	3.868		52.0
X6R1m-8	51.7	3.128	1977	ϵ	2.393	3.870		52.1
X6R1m-10	51.7	3.128	2025	ϵ	2.394	3.872		52.1
X6R1m-12	51.8	3.129	2115	ϵ	2.398	3.867		52.3
X6R1m-15	51.8	3.130	2201	ϵ	2.395	3.887		52.2
X6R1m-16	52.0	3.129	2192	ϵ	2.395	3.885		52.3
X6R1m-17	52.1	3.128	2214	ϵ	2.394	3.888		52.5
X6R1m-18	52.3	3.128	2268	ϵ + γ	2.392	3.888	3.396	53.6
X6R1m-19	52.2	3.129	2299	ϵ + γ	2.394	3.891	3.398	53.1
X6R1m-20	52.5	3.128	2378	ϵ + γ	2.400	3.860	3.395	54.8
X6R1m-21	52.5	3.129	2444	ϵ + γ	2.400	3.860	3.399	55.5
X6R1m-22	52.8	3.128	2491	γ			3.402	54.5
X6R1m-23	52.2	3.132	2556(F)	γ				
X6R1m-24	53.0	3.128	2581(F)	ϵ + γ	2.394	3.866	3.400	55.9
X6R1m-25	52.9	3.129	2646(F)	γ			3.401	56.2
X6R1m-26	52.8	3.129	2596(F)	γ			3.402	55.5
X6R1m-27	52.8	3.129	2635(F)	γ			3.406	54.6
X6R1m-28	52.9	3.130	2704(F)	γ			3.406	55.3
X6R1m-29	53.2	3.129	2757(F)	γ			3.410	54.6
X6R1m-30	53.3	3.129	2813(F)	γ			3.412	54.5
X6R1m-32	52.8	3.134	2994(F)	γ			3.414	55.6
X6R1m-33	54.1	3.129	3139(F)	γ +liquid			3.414	56.9
X6R1m-35	54.3	3.132	3465(F)	γ +liquid			3.412	56.3
X6R1m-36	54.6	3.132	3639(F)	γ +liquid			3.417	56.9
X6R1m-37	54.9	3.133	3833(F)	γ +liquid			3.417	59.0
X6R5m-125	51.3	3.128	1815	ϵ	2.394	3.859		51.4
X6R5m-128	51.4	3.128	1889	ϵ	2.396	3.870		50.5
X6R5m-129	51.5	3.128	1945	ϵ	2.398	3.870		50.4
X6R5m-130	51.7	3.128	2016	ϵ + γ	2.398	3.881	3.402	50.1
X6R5m-131	51.7	3.128	2026	ϵ + γ	2.398	3.882		50.1
X6R5m-132	51.2	3.131	2078	ϵ + γ	2.398	3.882		50.6
X6R5m-133	51.9	3.128	2124	ϵ + γ				
X6R5m-139	52.3	3.129	2335	γ			3.400	53.7
X6R5m-140	52.3	3.129	2307	γ			3.402	52.9
X6R5m-141	52.2	3.129	2364	γ			3.404	52.8

Name	P_{KCl} (GPa)	a_{KCl} (Å)	T (K)	phase	a_{hcp} (Å)	c_{hcp} (Å)	a_{fcc} (Å)	P_{Fe} (GPa)
X6R5m-142	52.3	3.129	2397	γ			3.402	53.7
X6R5m-143	53.0	3.127	2480	γ				
X6R5m-145	51.3	3.136	2502(F)	γ			3.407	53.1
X6R5m-146	52.7	3.130	2582(F)	γ			3.405	54.5
X6R5m-147	51.0	3.138	2520(F)	γ			3.405	53.9
X6R5m-148	51.7	3.136	2674(F)	γ			3.405	55.3
X6R5m-151	49.9	3.147	2785(F)	γ			3.410	54.8
X6R5m-152	51.7	3.137	2831(F)	γ			3.409	55.5
X6R5m-153	52.9	3.131	2837(F)	γ			3.413	54.4
X6R5m-155	53.2	3.131	2938(F)	γ			3.413	55.3
X6R5m-156	52.8	3.134	3026(F)	γ			3.413	56.1
X6R5m-158	51.5	3.141	3031(F)	γ			3.410	57.0
X6R5m-159	52.7	3.136	3137(F)	γ			3.420	55.2
X6R5m-160	52.8	3.136	3205(F)	γ			3.421	55.5
X6R5m-161	52.9	3.136	3248(F)	γ +liquid			3.418	56.7
X6R5m-164	65.5	3.077	3312(F)	γ +liquid			3.415	58.1
X6R5m-165	55.3	3.130	3778(F)	γ +liquid			3.416	62.1
X6R5m-169	54.0	3.135	3670(F)	γ +liquid			3.417	60.8
X6R5m-170	55.1	3.133	3959(F)	γ +liquid			3.416	63.7
X6R5m-171	55.3	3.129	3699(F)	γ +liquid			3.416	61.3
X6R6m-190	64.1	3.077	2692(F)	γ			3,368	67.3
X6R6m-191	64.4	3.076	2726(F)	γ			3.372	66.3
X6R6m-192	64.2	3.077	2772(F)	γ			3.375	65.7
X6R6m-193	64.6	3.076	2845(F)	γ			3.377	65.6
X6R6m-194	64.5	3.077	2877(F)	γ			3.374	66.9
X6R6m-195	64.4	3.078	2937(F)	γ			3.374	67.5
X6R6m-196	64.9	3.077	3044(F)	γ			3.380	66.4
X6R6m-197	64.7	3.078	3084(F)	γ			3.384	65.5
X6R6m-199	64.6	3.081	3277(F)	γ +liquid			3.381	68.2
X6R6m-200	65.1	3.079	3342(F)	γ +liquid			3.381	68.9
X6R6m-201	64,8	3,080	3314(F)	γ +liquid			3,380	69,0
X6R6m-202	64,7	3,080	3202(F)	γ +liquid			3,380	68,0
X6R6m-203	64,0	3,083	3225(F)	γ +liquid			3,379	68,5
X6R8m-248	75,0	3,030	2173	ϵ	2,354	3,805		73,3
X6R8m-249	74,9	3,030	2219	ϵ	2,356	3,801		73,5
X6R8m-250	75,0	3,031	2273	ϵ	2,355	3,806		73,8
X6R8m-251	75,3	3,030	2300	ϵ	2,355	3,805		74,2
X6R8m-252	75,1	3,031	2321	ϵ	2,355	3,806		74,2
X6R8m-253	75,1	3,031	2360	ϵ	2,353	3,811		74,8
X6R8m-254	75,0	3,031	2371	ϵ	2,355	3,804		75,0
X6R8m-255	75,0	3,032	2394	ϵ	2,355	3,804		75,2
X6R8m-256	74,7	3,033	2410	ϵ	2,355	3,804		75,3
X6R8m-257	75,3	3,031	2430	ϵ	2,358	3,819		72,8
X6R8m-258	75,2	3,032	2460	ϵ	2,360	3,814		72,9
X6R8m-259	75,1	3,032	2510	ϵ	2,357	3,817		74,2
X6R8m-260	75,2	3,032	2540	ϵ	2,360	3,815		73,6

Name	P_{KCl} (GPa)	a_{KCl} (Å)	T (K)	phase	a_{hcp} (Å)	c_{hcp} (Å)	a_{fcc} (Å)	P_{Fe} (GPa)
X6R8m-261	75,6	3,031	2597	ϵ	2,360	3,812		74,5
X6R8m-262	75,3	3,032	2580	ϵ	2,361	3,816		73,6
X6R8m-263	75,1	3,033	2646	ϵ				
X6R8m-264	75,3	3,033	2678	ϵ	2,358	3,812		76,1
X6R8m-265	75,4	3,033	2752	ϵ				
X6R8m-266	75,0	3,035	2764	ϵ	2,360	3,822		75,1
X6R8m-267	75,7	3,033	2834	ϵ	2,360	3,824		75,6
X6R8m-268	74,8	3,036	2880	ϵ				
X6R8m-269	74,5	3,038	2913	ϵ				
X6R8m-270	74,3	3,039	2973	ϵ	2,362	3,816		77,3
X6R8m-271	76,1	3,032	2973	$\epsilon+\gamma$	2,360	3,825		77,0
X6R8m-272	75,2	3,036	3013	$\epsilon+\gamma$	2,365	3,822		76,0
X6R8m-273	74,9	3,038	3105(F)	γ			3,355	75,7
X6R8m-274	76,0	3,034	3085(F)	γ			3,352	76,7
X6R8m-275	76,2	3,034	3191(F)	γ			3,350	78,4
X6R8m-276	76,5	3,033	3230(F)	γ				
X6R8m-278	76,8	3,033	3400(F)	γ			3,352	79,5
X6R8m-279	76,2	3,037	3532(F)	γ +liquid				
X6R8m-280	74,8	3,040	3534(F)	γ +liquid			3,348	82,1
X6R8m-281	76,4	3,036	3504(F)	γ +liquid			3,347	82,3
X6R8m-284	76,2	3,038	3746(F)	γ +liquid			3,351	82,8
X6R9m-319	75,9	3,029	2502	ϵ	2,355	3,795		77,3
X6R9m-320	75,7	3,030	2543	ϵ	2,356	3,800		76,8
X6R9m-321	76,4	3,028	2560	ϵ	2,356	3,800		76,9
X6R9m-322	76,4	3,028	2604	ϵ	2,358	3,792		77,5
X6R9m-323	76,2	3,029	2638	ϵ	2,357	3,795		77,9
X6R9m-324	76,6	3,029	2707	ϵ	2,358	3,800		77,7
X6R9m-325	76,1	3,030	2709	ϵ				
X6R9m-326	76,4	3,030	2762	ϵ	2,359	3,795		78,5
X6R9m-327	76,5	3,030	2802(F)	ϵ	2,360	3,800		77,9
X6R9m-328	76,8	3,029	2837(F)	ϵ	2,361	3,799		78,1
X6R9m-329	76,8	3,029	2883(F)	ϵ	2,362	3,801		78,0
X6R9m-330	76,1	3,032	2962(F)	ϵ	2,364	3,807		77,4
X6R9m-331	76,6	3,031	2981(F)	$\epsilon+\gamma$				
X6R9m-332	76,7	3,031	3028(F)	$\epsilon+\gamma$	2,365	3,812		77,2
X6R9m-333	76,6	3,031	3067(F)	$\epsilon+\gamma$	2,364	3,835		75,5
X6R9m-334	77,0	3,031	3164(F)	$\epsilon+\gamma$			3,346	79,7
X6R9m-335	76,7	3,033	3261(F)	γ			3,344	76,7
X6R9m-336	76,8	3,032	3255(F)	γ			3,345	76,8
X6R9m-337	77,1	3,032	3319(F)	γ			3,345	77,1
X6R9m-338	78,7	3,026	3376(F)	γ			3,346	78,7
X6R9m-339	77,8	3,030	3425(F)	γ			3,349	77,8
X6R9m-340	77,6	3,031	3425(F)	γ			3,350	77,6
X6R9m-341	75,7	3,037	3400(F)	γ			3,352	75,7
X6R9m-342	77,2	3,032	3473(F)	γ +liquid			3,352	77,2
X6R9m-343	75,7	3,039	3529(F)	γ +liquid			3,350	81,6

Name	P_{KCl} (GPa)	a_{KCl} (Å)	T (K)	phase	a_{hcp} (Å)	c_{hcp} (Å)	a_{fcc} (Å)	P_{Fe} (GPa)
X6R9m-344	76.2	3.037	3566(F)	γ +liquid			3.350	81.6
X6R9m-345	76.7	3.036	3659(F)	γ +liquid			3.352	82.0
X19R4-138	97.9	2.960	2635	ϵ	2.321	3.755		97.3
X19R4-139	97.8	2.961	2645	ϵ	2.325	3.760		95.0
X19R4-140	98.3	2.960	2767	ϵ	2.322	3.755		98.2
X19R4-141	98.3	2.960	2842	ϵ	2.325	3.760		97.0
X19R4-143	98.2	2.961	2882(F)	ϵ	2.326	3.762		96.7
X19R4-142	98.3	2.961	2894(F)	ϵ				
X19R4-144	98.3	2.961	2931(F)	ϵ				
X19R4-145	98.3	2.962	3076(F)	ϵ	2.328	3.768		97.2
X19R4-146	98.8	2.961	3133(F)	ϵ				
X19R4-147	98.6	2.962	3151(F)	ϵ	2.331	3.771		96.3
X19R4-148	99.0	2.962	3353(F)	ϵ				
X19R4-149	99.3	2.962	3521(F)	ϵ	2.334	3.776		98.5
X19R4-150	99.9	2.961	3615(F)	ϵ				
X19R4-151	99.9	2.962	3842(F)	ϵ + γ +liq.	2.336	3.780		101.0
X19R4-152	102.0	2.961	4724(F)	ϵ + γ +liq.			3.301	113.0
X19R4-153	99.3	2.970	4784(F)	ϵ + γ +liq.	2.330	3.792		113.0
X131R1-8	114.0	2.920	3207	γ +liquid	2.315	3.685		116.0
X131R1-9	115.0	2.920	3266	γ +liquid	2.315	3.685		117.0
X131R1-10	115.0	2.919	3370(F)	γ +liquid	2.315	3.685		118.0
X131R1-11	115.0	2.920	3416(F)	ϵ	2.308	3.697		120.0
X131R1-12	115.0	2.919	3506(F)	ϵ	2.307	3.729		117.0
X131R1-13	115.0	2.920	3514(F)	ϵ				
X131R1-18	115.0	2.920	3642(F)	ϵ	2.305	3.733		119.0
X131R1-19	115.0	2.921	3846(F)	ϵ				
X131R1-22	116.0	2.920	3892(F)	ϵ +liquid	2.308	3.725		121.0
X131R1-23	116.0	2.922	4069(F)	ϵ +liquid	2.302	3.753		122.0
X131R1-26	117.0	2.919	4264(F)	ϵ +liquid	2.321	3.689		125.0
X131R2-44	117.0	2.911	2759	ϵ	2.300	3.710		115.0
X131R2-45	116.0	2.913	2775	ϵ	2.301	3.706		115.0
X131R2-46	116.0	2.913	2775	ϵ	2.301	3.701		116.0
X131R2-47	116.0	2.914	2890	ϵ	2.298	3.712		117.0
X131R2-48	116.0	2.915	2920	ϵ	2.301	3.718		115.0
X131R2-49	116.0	2.915	3002	ϵ	2.303	3.722		114.0
X131R2-50	116.0	2.914	2957	ϵ	2.305	3.714		114.0
X131R2-51	115.0	2.917	3059	ϵ	2.303	3.719		115.0
X131R2-52	115.0	2.918	3179	ϵ	2.303	3.721		116.0
X131R2-53	117.0	2.915	3188	ϵ	2.303	3.720		116.0
X131R2-54	116.0	2.917	3347(F)	ϵ	2.304	3.731		116.0
X131R2-56	116.0	2.917	3403(F)	ϵ	2.305	3.728		117.0
X131R2-57	117.0	2.916	3485(F)	ϵ				
X131R2-60	116.0	2.917	3599(F)	ϵ				
X131R2-62	115.0	2.921	3602(F)	ϵ				
X131R2-63	117.0	2.916	3692(F)	ϵ	2.309	3.718		119.0
X131R2-64	117.0	2.916	3745(F)	ϵ				

Name	P_{KCl} (GPa)	a_{KCl} (Å)	T (K)	phase	a_{hcp} (Å)	c_{hcp} (Å)	a_{fcc} (Å)	P_{Fe} (GPa)
X131R2-65	118,0	2,914	3706(F)	ϵ	2,308	3,739		117,0
X131R2-66	117,0	2,915	3579(F)	ϵ	2,305	3,735		118,0
X131R2-67	117,0	2,916	3791(F)	ϵ				
X131R2-68	117,0	2,917	3841(F)	ϵ	2,315	3,750		114,0
X131R2-69	118,0	2,916	3911(F)	ϵ +liquid				
X131R3-86	128,0	2,886	2935	ϵ	2,290	3,691		125,0
X131R3-87	128,0	2,887	3109	ϵ	2,289	3,703		125,0
X131R3-88	129,0	2,887	3178	ϵ	2,290	3,710		124,0
X131R3-89	129,0	2,887	3264	ϵ	2,290	3,700		127,0
X131R3-90	128,0	2,889	3381(F)	ϵ	2,301	3,715		120,0
X131R3-91	129,0	2,888	3532(F)	ϵ	2,299	3,719		122,0
X131R3-92	129,0	2,889	3679(F)	ϵ	2,301	3,704		125,0
X131R3-93	129,0	2,890	3961(F)	ϵ	2,298	3,704		130,0
X131R3-94	128,0	2,893	4064(F)	ϵ +liquid	2,301	3,728		126,0
X131R3-96	128,0	2,892	4119(F)	ϵ +liquid	2,297	3,726		129,0
X131R4-151	133,0	2,876	2725	ϵ	2,277	3,681		132,0
X131R4-153	133,0	2,878	2837	ϵ				
X131R4-154	132,0	2,877	2887	ϵ				
X131R4-155	133,0	2,877	3083	ϵ	2,281	3,692		131,0
X131R4-156	133,0	2,877	3029	ϵ				
X131R4-157	133,0	2,875	3132	ϵ	2,280	3,705		130,0
X131R4-158	134,0	2,877	3165	ϵ				
X131R4-159	133,0	2,877	3276	ϵ	2,283	3,710		129,0
X131R4-160	133,0	2,879	3280(F)	ϵ	2,283	3,702		131,0
X131R4-161	133,0	2,878	3463(F)	ϵ	2,288	3,705		129,0
X131R4-162	134,0	2,879	3559(F)	ϵ	2,288	3,710		130,0
X131R4-163	133,0	2,878	3575(F)	ϵ	2,287	3,710		130,0
X131R4-164	134,0	2,879	3671(F)	ϵ	2,289	3,711		130,0
X131R4-165	134,0	2,877	3777(F)	ϵ	2,289	3,706		132,0
X131R4-167	135,0	2,875	3850(F)	ϵ	2,296	3,710		129,0
X131R4-168	136,0	2,876	3889(F)	ϵ				
X131R4-169	136,0	2,875	4114(F)	ϵ	2,294	3,704		134,0
X131R4-175	136,0	2,876	4175(F)	ϵ +liquid				
X131R4-177	134,0	2,879	4024(F)	ϵ +liquid	2,293	3,716		132,0
X131R4-181	136,0	2,876	4087(F)	ϵ +liquid	2,288	3,729		133,0
X131R4-182	135,0	2,878	4095(F)	ϵ +liquid	2,289	3,720		134,0
X10R1-16	127,0	2,889	2885	ϵ	2,280	3,653		136,0
X10R1-17	128,0	2,888	3080	ϵ	2,275	3,688		135,0
X10R1-18	128,0	2,888	3020	ϵ	2,275	3,690		134,0
X10R1-19	128,0	2,888	3051	ϵ	2,281	3,690		131,0
X10R1-20	129,0	2,887	3187	ϵ				
X10R1-21	128,0	2,888	3319	ϵ				
X10R1-22	129,0	2,887	3316(F)	ϵ				
X10R1-23	130,0	2,886	3357(F)	ϵ				
X10R1-24	129,0	2,886	3346(F)	ϵ	2,280	3,720		130,0
X10R1-25	130,0	2,885	3470(F)	ϵ				

Name	P_{KCl} (GPa)	a_{KCl} (Å)	T (K)	phase	a_{hcp} (Å)	c_{hcp} (Å)	a_{fcc} (Å)	P_{Fe} (GPa)
X10R1-26	130.0	2.886	3528(F)	ϵ				
X10R1-27	131.0	2.884	3644(F)	ϵ				
X10R1-28	130.0	2.885	3626(F)	ϵ				
X10R1-29	131.0	2.884	3666(F)	ϵ				
X10R1-30	131.0	2.884	3686(F)	ϵ				
X10R1-31	133.0	2.881	3922(F)	ϵ				
X10R1-32	133.0	2.881	4097(F)	ϵ				
X10R1-34	134.0	2.880	4269(F)	ϵ +liquid				
X10R1-35	136.0	2.882	5335(F)	ϵ +liquid				
X10R2-53	154.0	2.836	3295	ϵ				
X10R2-54	155.0	2.835	3256	ϵ				
X10R2-55	154.0	2.838	3411	ϵ	2.265	3.661		149.0
X10R2-56	154.0	2.837	3422	ϵ	2.266	3.653		151.0
X10R2-57	156.0	2.833	3443	ϵ				
X10R2-58	156.0	2.834	3532	ϵ				
X10R2-61	154.0	2.838	3685(F)	ϵ				
X10R2-62	155.0	2.837	3728(F)	ϵ				
X10R2-64	155.0	2.837	3835(F)	ϵ				
X10R2-66	156.0	2.836	4092(F)	ϵ	2.275	3.662		151.0
X10R2-67	156.0	2.835	4057(F)	ϵ	2.274	3.665		151.0
X10R2-70	156.0	2.835	4046(F)	ϵ	2.267	3.662		155.0
X10R2-72	158.0	2.833	4269(F)	ϵ	2.278	3.657		153.0
X10R2-73	158.0	2.834	4463(F)	ϵ +liquid	2.283	3.653		153.0
X10R2-77	160.0	2.833	4889(F)	ϵ +liquid	2.268	3.687		161.0
X10R2-78	159.0	2.832	4612(F)	ϵ +liquid	2.273	3.664		158.0
X10R3-110	178.0	2.794	2855	ϵ	2.234	3.591		178.0
X10R3-111	177.0	2.796	2859	ϵ	2.234	3.591		178.0
X10R3-112	178.0	2.794	2911	ϵ	2.234	3.592		179.0
X10R3-113	178.0	2.794	2972	ϵ	2.235	3.591		179.0
X10R3-114	177.0	2.796	2985	ϵ	2.235	3.592		179.0
X10R3-115	177.0	2.795	2912	ϵ	2.235	3.591		178.0
X10R3-116	179.0	2.794	3083	ϵ	2.236	3.595		178.0
X10R3-117	178.0	2.794	2949	ϵ	2.236	3.591		178.0
X10R3-118	178.0	2.795	3087	ϵ	2.237	3.591		178.0
X10R3-119	178.0	2.794	3012	ϵ	2.236	3.590		179.0
X10R3-120	179.0	2.793	2981	ϵ	2.238	3.593		176.0
X10R3-121	179.0	2.793	3045	ϵ	2.238	3.591		177.0
X10R3-122	179.0	2.794	3099	ϵ	2.237	3.592		178.0
X10R3-123	179.0	2.792	3020	ϵ	2.236	3.590		179.0
X10R3-124	179.0	2.793	3130	ϵ	2.237	3.590		180.0
X10R3-125	180.0	2.792	3234	ϵ	2.240	3.593		178.0
X10R3-126	180.0	2.792	3153	ϵ	2.243	3.590		175.0
X10R3-127	180.0	2.792	3161	ϵ	2.242	3.590		176.0
X10R3-128	180.0	2.792	3128	ϵ	2.240	3.592		177.0
X10R3-129	180.0	2.792	3286	ϵ				
X10R3-130	180.0	2.793	3326	ϵ				

Name	P_{KCl} (GPa)	a_{KCl} (Å)	T (K)	phase	a_{hcp} (Å)	c_{hcp} (Å)	a_{fcc} (Å)	P_{Fe} (GPa)
X10R3-131	180.0	2.792	3383	ϵ	2.245	3.610		172.0
X10R3-132	180.0	2.792	3383	ϵ	2.245	3.605		173.0
X10R3-136	180.0	2.792	3384	ϵ				
X10R3-137	180.0	2.793	3469	ϵ				
X10R3-138	180.0	2.794	3516	ϵ				
X10R3-142	182.0	2.792	3834	ϵ	2.250	3.620		172.0
X10R3-140	181.0	2.793	3865(F)	ϵ	2.238	3.613		182.0
X10R3-141	182.0	2.792	3982(F)	ϵ	2.240	3.623		180.0
X10R3-145	181.0	2.793	4208(F)	ϵ	2.250	3.630		174.0
X10R3-146	182.0	2.793	4316(F)	ϵ	2.250	3.636		174.0
X10R3-149	183.0	2.792	4460(F)	ϵ	2.253	3.636		174.0
X10R3-160	184.0	2.790	4587(F)	ϵ				
X10R3-152	182.0	2.793	4669(F)	ϵ	2.246	3.635		182.0
X10R4-184	200.0	2.761	3207	ϵ				
X10R4-185	197.0	2.767	3242	ϵ				
X10R4-186	201.0	2.761	3317	ϵ				
X10R4-187	198.0	2.766	3350	ϵ	2.213	3.572		204.0
X10R4-189	196.0	2.768	3381	ϵ	2.218	3.572		200.0
X10R4-191	203.0	2.761	4073(F)	ϵ				
X10R4-190	206.0	2.756	4083(F)	ϵ	2.220	3.580		205.0
X10R4-192	202.0	2.761	4059(F)	ϵ	2.225	3.575		202.0
X10R4-193	203.0	2.761	4162(F)	ϵ	2.225	3.575		203.0
X10R4-194	204.0	2.759	4190(F)	ϵ	2.225	3.575		204.0
X10R4-195	204.0	2.760	4334(F)	ϵ				
X10R4-196	205.0	2.760	4642(F)	ϵ				
X10R4-197	204.0	2.759	4333(F)	ϵ	2.228	3.580		202.0
X10R4-204	204.0	2.761	4695(F)	ϵ	2.238	3.599		195.0
X10R4-205	200.0	2.766	4673(F)	ϵ	2.239	3.599		194.0
X10R4-206	201.0	2.765	4562(F)	ϵ	2.244	3.600		189.0
X10R4-211	204.0	2.762	4923(F)	ϵ				
X7R3-145	164.0	2.815	2459	ϵ	2.245	3.619		160.0
X7R3-146	163.0	2.817	2537	ϵ	2.248	3.597		164.0
X7R3-147	162.0	2.816	2624	ϵ	2.249	3.628		157.0
X7R3-148	163.0	2.819	2697	ϵ	2.249	3.608		163.0
X7R3-149	164.0	2.819	2738	ϵ				
X7R3-150	164.0	2.817	2815	ϵ	2.248	3.612		164.0
X7R3-151	165.0	2.816	2887	ϵ	2.245	3.629		163.0
X7R3-152	162.0	2.816	2956	ϵ				
X7R3-156	163.0	2.819	3156	ϵ				
X7R3-157	166.0	2.816	3276	ϵ				
X7R3-158	165.0	2.816	3321	ϵ				
X7R3-159	165.0	2.818	3364	ϵ				
X7R3-160	166.0	2.816	3439	ϵ				
X7R3-161	164.0	2.819	3598	ϵ				
X7R3-162	165.0	2.819	3806(F)	ϵ				
X7R3-163	171.0	2.810	4111(F)	ϵ	2.257	3.616		171.0
X7R3-172	172.0	2.809	4389(F)	ϵ	2.260	3.642		168.0

Bibliography

- [1] A.M. Dziewonski and D.L. Anderson. *Phys. Earth. Planet. Interiors*, 25:297, 1981.
- [2] O.L. Anderson. Equations of state of solids for geophysics and ceramic science. *Oxford Univ. Press.*, 1995.
- [3] D.J. Stevenson. *Science*, 214:611, 1981.
- [4] J.A. Jacobs. *The Earth's Core*. New York: Academic, 1987.
- [5] Q. Williams and R. Jeanloz. *J. Geophys. Res.*, 95:19299, 1990.
- [6] J.P. Poirier. *Introduction to the Physics of the Earth's Interior*. Cambridge University Press, Cambridge, 1991.
- [7] R. Brett. *Rev. Geophys. Space Phys.*, 14:375, 1976.
- [8] R.T. Merrill and M.W. McElhinny. The earth's magnetic field: Its history, origin and planetary perspective. *Academic, New York*, 1983.
- [9] R.A. Langel and J.A. Jacobs. *Geomagnetism*, volume 1,2. New York: Academic, 1987.
- [10] F. Birch. *J. Geophys. Res.*, 57:227, 1952.
- [11] R.G. McQueen and S.P. Marsh. *J. Geophys. Res.*, 71:1751, 1966.
- [12] R. Jeanloz and F.M. Richter. *J. Geophys. Res.*, 84:5497, 1979.
- [13] J.M. Brown and R.G. McQueen. *J. Geophys. Res.*, 91:7485, 1986.
- [14] J.A. Jacobs. *The Earth's Core*. Academic Press (London), 1987.
- [15] T. Lay, J. Hernlund, and B.A. Buffett. *Nature Geoscience*, 1:25, 2008.
- [16] D. Alfé, M.J. Gillan, and G.D. Price. *Contemp. Phys.*, 48:63, 2007.
- [17] K.C. Creager. *Nature*, 356:309, 1992.
- [18] L.J. Swartzendruber. *Bull. Alloy Phase Diagr.*, 3:161, 1982.

- [19] J.M. Leger, C. Loriers-Susse, and B. Vodar. *Phys. Rev. B*, 6:4250, 1972.
- [20] M.V. You, V. Heine, A.J. Holden, and P.J. Lin-Chung. *Phys. Rev. Lett.*, 44:1282, 1980.
- [21] H. Hasegawa, M.W. Finnis, and D.G. Pettifor. *J. Phys. F: Met. Phys.*, 15:19, 1985.
- [22] D. Bancroft, E.L. Peterson, and S. Minshall. *J. Appl. Phys.*, 27:291, 1956.
- [23] M. Nicol and G. Jura. *Science*, 141:1035, 1963.
- [24] K. Shimizu, T. Kimura, S. Furomoto, K. Takeda, K. Kontani, Y. Onuki, and K. Amaya. *Nature*, 412:316, 2001.
- [25] S.K. Bose, O.V. Dolgov, J. Kortus, O. Jepsen, and O.K. Andersen. *Phys. Rev. B*, 67:214518, 2003.
- [26] C.S. Yoo, N.C. Holmes, M. Ross, D.J. Webb, and C. Pike. *Phys. Rev. Lett.*, 70:3931, 1993.
- [27] J.H. Nguyen and N.C. Holmes. *Nature*, 427:339, 2004.
- [28] R. Boehler. *Nature*, 363:534, 1993.
- [29] G. Shen, V.B. Prakapenka, M.L. Rivers, and S.R. Sutton. *Phys. Rev. Lett.*, 92:185701, 2004.
- [30] Q. Williams, R. Jeanloz, J. Bass, B. Svendsen, and T.J. Ahrens. *Science*, 236:181, 1987.
- [31] Y. Ma, M. Somayazulu, G. Shen, H.K. Mao, J. Shu, and R.J. Hemley. *Phys. Earth Planet. Inter.*, 143-144:455, 2004.
- [32] A.B. Belonoshko, R. Ahuja, and B. Johansson. *Phys. Rev. Lett.*, 84:3638, 2000.
- [33] D. Alfè, G.D. Pride, and M.J. Gillan. *Phys. Rev. B*, 65:165118, 2002.
- [34] D. Alfè. *Phys. Rev. B*, 79:060101, 2009.
- [35] E. Sola and D. Alfè. *Phys. Rev. Lett.*, 103:078501, 2009.
- [36] R. Boehler. *Geophys. Res. Lett.*, 13:1153, 1986.
- [37] Q. Williams, E. Knittle, and R. Jeanloz. *J. Geophys. Res.*, 96:2171, 1991.

- [38] Q. Williams. The temperature contrast across d". In *The Core-Mantle Boundary Region*, page 73. the American Geophysical Union., 1998.
- [39] S. Tateno, K. Hirose, Y. Ohishi, and Y. Tatsumi. *Science*, 330:359, 2010.
- [40] S.N. Luo and T.J. Ahrens. *Phys. Earth Planet. Inter.*, 143-144:369, 2004.
- [41] J.M. Jackson, W. Sturhahn, M. Lerche, J. Zhao, T.S. Toellner, E.E. Alp, S.V. Sinogeikin, J.D. Bass, C.A. Murphy, and J.K. Wicks. *Earth Planet. Sci. Lett.*, 362:143, 2013.
- [42] A. Laio, S. Bernard, G.L. Chiarotti, S. Scandolo, and E. Tosatti. *Science*, 287:1027, 2000.
- [43] L. Liu. *Geophys. J. R. astr. Soc.*, 43:697, 1975.
- [44] C.S. Yoo, J. Akella, A.J. Campbell, H.K. Mao, and R.J. Hemley. *Science*, 270:1473, 1995.
- [45] G. Shen, H.K. Mao, R.J. Hemley, T.S. Duffy, and M.L. Rivers. *Geophys. Res. Lett.*, 25:373, 1998.
- [46] T. Komabayashi, Y. Fei, Y. Meng, and V. Prakapenka. *Earth Planet. Sci. Lett.*, 282:252, 2009.
- [47] M. Ross, D.A. Young, and R. Grover. *J. Geophys. Res.*, 95:21713, 1990.
- [48] M. Matsui and O.L. Anderson. *Phys. Earth Planet. Inter.*, 103:55, 1997.
- [49] A.B. Belonoshko, R. Ahuja, and B. Johansson. *Nature*, 424:1032, 2003.
- [50] P. Soderlind, J.A. Moriarty, and J.M. Wills. *Phys. Rev. B*, 53:14063, 1996.
- [51] L. Vocadlo, J. Brodholt, D. Alfè, M.J. Gillan, and G.D. Price. *Phys. Earth Planet. Inter.*, 117:123, 2000.
- [52] L. Stixrude, R.E. Cohen, and D.J. Singh. *Phys. Rev. B*, 50:6442, 1994.
- [53] L. Dubrovinsky, N. Dubrovinskaia, O. Narygina, I. Kantor, A. Kuznetsov, V.B. Prakapenka, L. Vitos, B. Johansson, A.S. Mikhaylushkin, S.I. Simak, and I.A. Abrikosov. *Science*, 316:1880, 2007.
- [54] S.K. Saxena, G. Shen, and P. Lazor. *Science*, 260:1312, 1993.

- [55] C.S. Yoo, P. Soderling, J.A. Moriarty, and A.J. Campbell. *Phys. Rev. Lett A*, 214:65, 1996.
- [56] S.K. Saxena, L.S. Dubrovinsky, P. Haggkvist, C. Cerenius, G. Shen, and H.K. Mao. *Science*, 269:1703, 1995.
- [57] D. Andrault, G. Fiquet, M. Kunz, F. Visocekas, and D. Hausermann. *Science*, 278:831, 1997.
- [58] Y. Kuwayama, K. Hirose, N. Sata, and Y. Ohishi. *Earth Planet. Sci. Lett.*, 273:379, 2008.
- [59] D. Errandonea, B. Schwager, R. Ditz, C. Gessmann, R. Boehler, and M. Ross. *Phys. Rev. B*, 63:132104, 2001.
- [60] A. Dewaele, M. Mezouar, N. Guignot, and P. Loubeyre. *Phys. Rev. B*, 76:144106, 2007.
- [61] A. Dewaele, M. Mezouar, N. Guignot, and P. Loubeyre. *Phys. Rev. Lett.*, 104:255701, 2010.
- [62] E. Schultz, M. Mezouar, W. Crichton, S. Bauchau, G. Blattmann, D. Andrault, G. Fiquet, R. Boehler, N. Rambert, B. Sitaud, and P. Loubeyre. *High Press. Res.*, 25:71, 2005.
- [63] T. Matsushita and R.P. Phizackerley. *Jpn. J. Appl. Phys.*, 20:2223, 1981.
- [64] S. Pascarelli, O. Mathon, M. Munoz, T. Mairs, and J. Susini. *J. Synch. Rad.*, 13:351, 2006.
- [65] J.C. Jamieson, A.W. Larson, and N.D. Nachtrieb. *Rev. Sci. Inst.*, 30:1016, 1959.
- [66] C.E. Weir, E.R. Lippincott, A. VanValkenburg, and E.N. Bunting. *Journal of Research of the National Bureau of Standards- A. Physics and Chemistry*, 63:55, 1959.
- [67] R. LeToullec, J.P. Pinceaux, and P. Loubeyre. *High Press. Res.*, 1:77, 1988.
- [68] J.M. Besson and J.P. Pinceaux. *Science*, 206:1073, 1979.
- [69] R. Boehler and K. De Hantsetters. *High Press. Res.*, 24:391, 2007.
- [70] R.J. Hemley, H.K. Mao, G. Shen, J. Badro, P. Gillet, M. Hanfland, and D. Hauserman. *Science*, 276:1242, 1997.
- [71] A. Dadashev, M.P. Pasternak, G.K. Rozenberg, and R.D. Taylor. *Rev. Sci. Instrum.*, 72:2633, 2001.

- [72] H.K. Mao and P.M. Bell. *Science*, 200:1145, 1978.
- [73] D.J. Dunstan. *Rev. Sci. Instrum.*, 60:3789, 1989.
- [74] T.S. Duffy, G. Shen, D.L. Heinz, J. Shu, Y. Ma, H.K. Mao, R.J. Hemley, and A.K. Singh. *Phys. Rev. B*, 60:15063, 1999.
- [75] L. Liu, T. Takahashi, and W.A. Bassett. *J. Phys. Chem. Solids*, 31:1345, 1970.
- [76] Y.K. Vohra, S.J. Duclos, and A.L. Ruoff. *Phys. Rev. B*, 36:9790, 1987.
- [77] R. Jeanloz, B.K. Godwal, and C. Meade. *Nature*, 349:687, 1991.
- [78] S. Klotz, J-C. Chervin, P. Munsch, and G. Le Marchand. *J. Phys. D: Appl. Phys.*, 42:075413, 2009.
- [79] H.K. Mao, R.J. Hemley, Y. Wu, A.P. Jephcoat, L.W. Finger, C.S. Zha, and W.A. Bassett. *Phys. Rev. Lett.*, 60:2649, 1988.
- [80] K. Takemura. *J. Appl. Phys.*, 89:662, 2001.
- [81] A. Dewaele and P. Loubeyre. *High Press. Res.*, 27:419, 2007.
- [82] F. Datchi, P. Loubeyre, and R. LeToullec. *Phys. Rev. B*, 61:6535, 2000.
- [83] Z.M. Geballe and R. Jeanloz. *J. Appl. Phys.*, 111:123518, 2012.
- [84] Z. Konopková, P. Lazor, A.F. Goncharov, and V.V. Struzhkin. *High Press. Res.*, 31:228, 2011.
- [85] A.A. El-Sharkawy, I.H. Rashed, M.S. Zaghoul, and M.H. Ghoniem. *Phys. Stat. Sol. (a)*, 85:429, 1984.
- [86] M. Mezouar, W.A. Crichton, S. Bauchau, F. Thurel, H. Witsch, F. Torrecillas, G. Blattmann, P. Marion, Y. Dabin, J. Chavanne, O. Hignette, C. Morawe, and C. Borel. *J. Synch. Rad.*, 12:659, 2005.
- [87] P. Kirkpatrick and A.V. Baez. *J. Opt. Soc. Am.*, 38:766, 1948.
- [88] B.E. Warren. *X Ray Diffraction*. Dover Publications, New York, 1990.
- [89] A. Hammersley, S. Stevenson, M. Hanfland, A. Fitch, and D. Hausermann. *High Press. Res.*, 14:235, 1996.
- [90] R. Torchio, Y.O. Kvashnin, S. Pascarelli, O. Mathon, C. Marini, L. Genovese, P. Bruno, G. Gambarino, A. Dewaele, F. Occelli, and P. Loubeyre. *Phys. Rev. Lett.*, 107:237202, 2011.

- [91] R. Torchio, A. Monza, F. Baudelet, S. Pascarelli, O. Mathon, E. Pugh, D. Antonangeli, and J.P. Itie. *Phys. Rev. B*, 84:060403, 2011.
- [92] O. Mathon, F. Baudelet, J.P. Itie, A. Polian, M. D' Astuto, J.C. Chervin, and S. Pascarelli. *Phys. Rev. Lett.*, 93:255503, 2004.
- [93] R. Boehler, H.G. Musshoff, R. Ditz, G. Aquilanti, and A. Trapananti. *Rev. Sci. Instrum.*, 80:045103, 2009.
- [94] D. Andrault, M. Munoz, N. Bolfan-Casanova, N. Guignot, J.P. Perrillat, G. Aquilanti, and S. Pascarelli. *Earth Planet. Sci. Lett.*, 293:90, 2010.
- [95] W. Gawelda, V.T. Pham, M. Benfatto, Y. Zaushitsyn, M. Kaiser, D. Grolimund, S.L. Johnson, R. Abela, A. Hauser, C. Bressler, and M. Chergui. *Phys. Rev. Lett.*, 98:057401, 2007.
- [96] B.K. Agarwal. *X-Ray Spectroscopy*. Springer, Berlin, 1991.
- [97] D.C. Koningsberger and R. Prins. *X-Ray Absorption: Principle, Application, Techniques of EXAFS, SEXAFS and XANES*. Wiley, New York, 1988.
- [98] J. Stohr. *NEXAFS Spectroscopy*. Springer, Berlin, 1992.
- [99] M. Newville. *Fundamentals of XAFS*. Consortium for Advanced Radiation Sources, University of Chicago, Chicago, IL, 2004.
- [100] D.E. Sayers, E.A. Stern, and F.W. Lytle. *Phys. Rev. Lett.*, 27:1204, 1971.
- [101] P.A. Lee, P.H. Citrin, P. Eisenberg, and B.M. Kincaid. *Rev. Mod. Phys.*, 53:769, 1981.
- [102] T.M. Hayes and J.B. Boyce. *Solid State Physics*, 37:173, 1983.
- [103] B.K. Teo. *EXAFS: Basic Principles and Data Analysis: A Practical Guide to X-Ray Absorption Fine Structure Spectroscopy*. Springer, Berlin, 1986.
- [104] S.J. Gurman. *J. Synch. Rad.*, 2:56, 1995.
- [105] G. Bunker. *Introduction to XAFS*. Cambridge University Press, 2010.
- [106] F. Bardelli, G. Barone, V. Crupi, F. Longo, D. Majolino, P. Mazzoleni, and V. Venuti. *Anal. Bioanal. Chem.*, 399:3147, 2011.
- [107] R. Terzano, Z. Al Chami, B. Vekemans, K. Janssens, T. Miano, and P. Ruggiero. *J. Agric. Food Chem.*, 56:3222, 2008.

- [108] A. Vairavamurthy. *Spectroscopia Acta A*, 54:2009, 1998.
- [109] S.P. Cramer, T.K. Eccles, F.W. Kutzler, K.O. Hodgson, and L.E. Morteson. *J. Am. Chem. Soc.*, 98:1287, 1976.
- [110] R.P. Phizackerley, Z.U. Rek, G.B. Stephenson, S.D. Conradson, K.O. Hodgson, T. Matsushita, and H. Oyanagi. *J. Appl. Cryst.*, 16:220, 1983.
- [111] R. Torchio, O. Mathon, and S. Pascarelli. *Coord. Chem. Rev.*, In press.
- [112] A.L. Ankudinov, B. Ravel, J.J. Rehr, and S.D. Conradson. *Phys. Rev. B*, 58:7565, 1998.
- [113] [Http://Cars9.Uchicago.Edu/Cgi-Bin/Atoms/Atoms.Cgi](http://Cars9.Uchicago.Edu/Cgi-Bin/Atoms/Atoms.Cgi).
- [114] S. Merkel, R.J. Hemley, and H.K. Mao. *Appl. Phys. Lett.*, 74:656, 1999.
- [115] R.A. Forman, G.J. Piermarini, J.D. Barnett, and S. Block. *Science*, 176:284, 1972.
- [116] J.D. Barnett, S. Block, and G.J. Piermarini. *Rev. Sci. Instrum.*, 44:1, 1973.
- [117] K. Takemura and A. Dewaele. *Phys. Rev. B*, 78:104119, 2008.
- [118] H.K. Mao, J. Xu, and P.M. Bell. *J. Geophys. Res.*, 91:4673, 1986.
- [119] W.J. Carter, S.P. Marsh, J.N. Fritz, and R.G. McQueen. *Accurate Characterization of the High Pressure Environment*, volume 326 of *NBS Spec. Publ.* E.C. Llyod, National bureau of standards, Washington DC, 1971.
- [120] W.B. Holzapfel. *J. Appl. Phys.*, 93:1813, 2003.
- [121] A. A. dewaele and p. loubeyre and m. mezouar. *Phys. Rev. B*, 70:094112, 2004.
- [122] P.I. Dorogokupets and A.R. Oganov. *Phys. Rev. B*, 75:024115, 2007.
- [123] K. Syassen. *High Press. Res.*, 28:75, 2008.
- [124] A. Dewaele, M. Torrent, P. Loubeyre, and M. Mezouar. *Phys. Rev. B*, 78:104102, 2008.
- [125] W.L. Vos and J.A. Schouten. *J. Appl. Phys.*, 69:6744, 1991.
- [126] S. Rekhi, L. Dubrovinsky, and S. K. Saxena. *High Temp.- High Press.*, 31:299, 1999.

- [127] A.F. Goncharov, J.M. Zaug, J.C. Crowhurst, and E. Gregoryanz. *J. Appl. Phys.*, 97:094917, 2005.
- [128] N.C. Holmes, J.A. Moriarty, G.R. Gathers, and W.J. Nellis. *J. Appl. Phys.*, 66:2962, 1989.
- [129] J.C. Jamieson, J.N. Fritz, and M.H. Manghnani. *High Pressure Research in Geophysics*. S. Akimoto and M.H. Manghnani, Academic, Tokio, 1982.
- [130] R. Hixson and J.N. Fritz. *J. Appl. Phys.*, 71:1721, 1992.
- [131] P.I. Dorogokupets and A. Dewaele. *High Press. Res.*, 27:431, 2007.
- [132] A. Dewaele, A.B. Belonoshko, G. Garbarino, F. Occelli, P. Bouvier, M. Hanfland, and M. Mezouar. *Phys. Rev. B*, 85:214105, 2012.
- [133] P. Vinet, J. Ferrante, J.H. Rose, and J.R. Smith. *J. Geophys. Res.*, 92:9319, 1987.
- [134] A. Dewaele, P. Loubeyre, F. Occelli, M. Mezouar, P.I. Dorogokupets, and M. Torrent. *Phys. Rev. Lett.*, 97:215504, 2006.
- [135] J.M. Brown, J.N. Fritz, and R.S. Hixson. *J. Appl. Phys.*, 88:5496, 2000.
- [136] D. Alfè, G.D. Price, and M.J. Gillan. *Phys. Rev. B*, 64:045123, 2001.
- [137] P.I. Dorogokupets and A.R. Oganov. *Doklady Earth Sciences*, 410:1091, 2006.
- [138] G. Shen, W. Sturhahn, E.E. Alp, J. Zhao, T.S. Toellner, V.B. Prakapenka, Y. Meng, and H.R. Mao. *Phys. Chem. Minerals*, 31:353, 2004.
- [139] T. Komabayashi and Y. Fei. *J. Geophys. Res.: Solid Earth*, 115:B03202, 2010.
- [140] O.L. Anderson, H. Oda, and D. Isaak. *Geophys. Res. Lett.*, 19:1987, 1992.
- [141] R. Boehler, N. Von Bargen, and A. Chopelas. *J. Geophys. Res.*, 95:21731, 1990.
- [142] L. Dubrovinsky, N. Dubrovinskaia, V.B. Prakapenka, and A.M. Abakumov. *Nature Communication*, 2012.
- [143] A.P. Jephcoat and S.P. Besedin. *Philos. Trans. R. Soc. London, Ser. A*, 354:1333, 1996.

- [144] C.T. Seagle, D.L. Heinz, Z. Liu, and R.J. Hemley. *Applied Optics*, 48:545, 2009.
- [145] M.J. Walter and K.T. Koga. *Phys. Earth Planet. Int.*, 143:541, 2004.
- [146] L.R. Benedetti and P. Loubeyre. *High Press. Res.*, 24:423, 2004.
- [147] S. Petitgirard, A. Salamat, P. Beck, G. Weck, and P. Bouvier. *J. Synchrotron Rad.*, 21:89, 2013.
- [148] Y.S. Touloukian and D.P. Dewitt. *Thermophysical Properties of Matter*. IFI, Plenum Press, 1970.
- [149] L.S. Dubrovinsky and S.K. Saxena. *High Temp. High Press.*, 31:393, 1999.
- [150] R. Boehler, M. Ross, and D.B. Boercker. *Phys. Rev. B*, 53:556, 1996.
- [151] G. Morard, J. Siebert, D. Andrault, N. Guignot, G. Garbarino, F. Guyot, and D. Antonangeli. *Earth Planet. Sci. Lett.*, 373:169, 2013.
- [152] D. Andrault, S. Petitgirard, G. Lo Nigro, J.L. Davidal, G. Veronesi, G. Garbarino, and M. Mezouar. *Nature*, 487:354, 2012.
- [153] D. Santamaria-Pérez, M. Ross, D. Errandonea, G.D. Mukherjee, M. Mezouar, and R. Boehler. *J. Chem. Phys.*, 130:124509, 2009.
- [154] N. Sata, K. Hirose, G. Shen, Y. Nakajima, Y. Ohishi, and N. Hirao. *J. Geophys. Res.: Solid Earth*, 115:B09204, 2010.
- [155] D.L. Heinz and R. Jeanloz. *J. Geophys. Res.*, 92:11437, 1987.
- [156] R. Boehler. *Philos. Trans. R. Soc. London, Ser. A*, 354:1265, 1996.
- [157] P. Lazor, G. Shen, and S.K. Saxena. *Phys. Chem. Minerals*, 20:86, 1993.
- [158] R. Boehler, D. Santamaria-Perez, D. Errandonea, and M. Mezouar. *J. Phys.: Conf. Ser.*, 121:1, 2008.
- [159] B. Steinberger and R. Holme. *J. Geophys. Res.*, 113:B05403, 2008.
- [160] G. Fiquet, A.L. Auzende, J. Siebert, A. Corgne, H. Bureau, H. Osawa, and G. Garbarino. *Science*, 329:1516, 2010.
- [161] S. Tateno, K. Hirose, N. Sata, and Y. Ohishi. *Earth Planet. Sci. Lett.*, 277:130, 2009.
- [162] L. Vocadlo, D. Alfe, M.J. Gillan, I.G. Wood, J.P. Brodholt, and G.D. Price. *Nature*, 424:536, 2003.

- [163] G. Morard, D. Andrault, N. Guignot, J. Siebert, G. Garbarino, and D. Antonangeli. *Phys. Chem. Minerals*, 38:767, 2011.
- [164] T. Nakagawa and P.J. Tackley. *Geophys. Res. Lett.*, 40:2652, 2013.
- [165] C. Sanloup, F. Guyot, P. Gillet, G. Fiquet, R.J. Hemley, M. Mezouar, and I. Martinez. *Europhys. Lett.*, 52:151, 2000.
- [166] S.L. Johnson, P.A. Heimann, A.M. Lindenberg, H.O. Jeschke, M.E. Garcia, Z. Chang, R.W. Lee, J.J. Rehr, and R.W. Falcone. *Phys. Rev. Lett.*, 91:157403–1, 2003.
- [167] S. De Panfilis, A. Filipponi, and C. Meneghini. *J. Synchrotron Rad.*, 6:549, 1999.
- [168] M. Azuma, W. T. Chen, H. Seki, M. Czapski, S. Olga, K. Oka, M. Mizumaki, T. Watanuki, N. Ishimatsu, N. Kawamura, S. Ishiwata, M.G. Tucker, Y. Shimakawa, and J.P. Attfield. *Nature Communications*, 2(347):317, 2011.
- [169] T. Ressler, R.E. Jentoft, J. Wienold, M.M. Gunter, and O. Timpe. *J. Phys. Chem. B*, 104:6360, 2000.
- [170] C. Marini, I. Kantor, O. Mathon, and S. Pascarelli. *High Press. Res.*, 33:108, 2013.
- [171] J.C. Labiche, O. Mathon, S. Pascarelli, M.A. Newton, G.G. Ferre, C. Curfs, , G. Vaughan, A. Homs, and D.F. Carreiras. *Rev. Sci. Instr.*, 78:091301, 2007.
- [172] M. MuñOz, S. Pascarelli, G. Aquilanti, O. Narygina, A. Kurnosov, and L. Dubrovinsky. *High Press. Res.*, 28:665, 2008.
- [173] S. Anzellini, A. Dewaele, M. Mezouar, P. Loubeyre, and G. Morard. *Science*, 340:464, 2013.